

UNIVERSITÀ DEGLI STUDI DI PERUGIA

XXXVII CICLO DEL DOTTORATO DI RICERCA IN FISICA



Characterization of the performance of very long silicon detectors

Studente:

Jiang YAOZU

tutors:

Prof. Bruna BERTUCCI

Dr. Matteo DURANTI

"In society, knowledge should not be used to reinforce inequality, but to eliminate injustice."

—Richard Feynman

Acknowledgement

I would like to express my heartfelt gratitude to everyone who has cared for, supported, and helped me throughout the completion of my thesis. First and foremost, I would like to extend my special thanks to Professor Bruna Bertucci. Thank you for taking the time out of your busy schedule to help me revise my thesis and answer my various questions. Your patience and professional academic spirit have deeply impressed upon me the charm of an outstanding scholar and inspired my strong aspiration to pursue the path of scientific research. Secondly, I would like to thank Matteo. Over the past three years, you have consistently given me endless encouragement and guidance, making every effort to ensure that I have access to the same educational resources as others. Your compassion for disadvantaged groups has shown me the power of responsibility and morality. Your words and actions have not only profoundly influenced my academic journey but also inspired my deep reflection on social justice. Finally, I want to express my gratitude to Mattia. Thank you for your care and companionship over the years. Your support has long transcended the boundaries of a mere professional relationship. From you, I have seen the shared humanity that surpasses borders, cultures, and religious differences. Your sense of justice and kindness has strengthened my belief in a beautiful and peaceful world.

Contents

Introduction	V
1 Physical Background	1
1.1 Introduction to Cosmic Rays	1
1.1.1 Discovery of Cosmic Rays	1
1.1.2 Cosmic Rays Spectrum	3
1.1.3 Origin of Galactic Cosmic Rays	5
1.1.4 Acceleration of Galactic Cosmic Rays	6
1.1.5 Propagation of Galactic Rays	12
1.2 Dark Matter	14
1.2.1 Observational Evidence for DM	15
1.2.2 Detection of DM	16
1.3 Antimatter	16
1.3.1 History of Antimatter Discovery	17
1.3.2 Observation in cosmic rays	19
2 Space borne cosmic ray detectors	21
2.1 The AMS-02 Experiment	22
2.1.1 Detector Structure	23
2.1.2 AMS-02 Layer 0 upgrade	35

2.2	The HERD Experiment	41
2.2.1	Detector Structure	41
3	Silicon Microstrip Detectors	49
3.1	The semiconductors	49
3.1.1	Intrinsic semiconductors	50
3.1.2	Extrinsic semiconductors	53
3.1.3	The p-n junction	56
3.2	The single-sided microstrip detectors	62
3.2.1	AC coupling and DC coupling	64
3.2.2	Bias rings	65
3.2.3	Guard rings	67
3.2.4	Floating strips	67
3.2.5	Ladder	67
3.3	Signal formation and acquisition	68
3.3.1	Energy deposition	68
3.3.2	Noise contributions	70
3.3.3	Charge-sensitive amplifier	71
3.3.4	Pulse shaper	73
3.3.5	Chip IDE1140 - VA	73
3.4	Signal Analysis	75
3.4.1	Calibration	75
3.4.2	Cluster search	79
3.4.3	η correction	90
3.4.4	VA equalization	94
3.4.5	Alignment	95
4	Detector Studies with Particle Beams	107
4.1	L0 beam tests	107
4.1.1	Beam Test with muons	108
4.1.2	Test with heavy ions	118

4.2 HERD-SCD beam tests	129
4.2.1 Beam test with electrons	132
4.2.2 Test with heavy ions	138
Conclusions	145
Bibliography	147

Introduction

Since their discovery at the beginning of the last century, Cosmic Rays (CRs) have represented a precious probe for fundamental physics. This flux of charged particles, mainly proton and helium nuclei, has been the first natural particle beam at the dawn of elementary particle physics, and even now, a century after their discovery, CRs are a powerful tool for exploring the mysteries of the universe.

Astronomical observations indicate that the universe is mainly composed of dark energy ($\sim 68\%$) and dark matter ($\sim 27\%$), with only a mere $\sim 5\%$ of matter. Weakly Interacting Massive Particles (WIMPs) are among the leading candidates for dark matter particles. Their indirect search in cosmic rays can be performed by looking an excess of high-energy photons, positron and anti-protons, produced in their annihilation/decay. Searching for this tiny excess of anti-particles of exotic origin, requires a deep knowledge of the CRs characteristics from ordinary astronomical sources, in terms of their composition, energy spectra and interactions with the Inter Stellar Medium. The existence of heavier anti-matter particles, as $Z \geq 2$ ions, never observed as of today in CRs, is still a challenging theoretical and experimental open question since it could be a relic of a primordial symmetric universe, apparently evolved into the asymmetric one dominated by matter.

Study of the rare anti-particle fluxes in CRs requires to minimize backgrounds from secondary particles produced in the CRs interactions with the atmosphere: space is the ideal environment to ensure no atmospheric background and different experimental programs started in the late 90s to be carried on satellites and on the International Space Station to pursue direct measurements of the composition and energy spectra of

CRs and γ -rays.

Different platforms and measurement approaches have been adopted along the years, with the successful AMS-01 and PAMELA experiments, and the still operating Fermi, AMS-02 and DAMPE experiments. In spite of their different design and specific objectives, all these instruments feature silicon microstrip detectors for tracking and absolute charge measurement.

Silicon microstrip detectors, a common technology in high-energy experiments at colliders, feature excellent spatial resolution and absolute charge measurement. They are particularly suited for space applications, being lightweight and with no need for high voltage power supplies or gas vessels hard to operate/be refurbished in outer space. The real challenge is to instrument with silicon sensors ever larger surface to increase detection acceptances, while keeping manageable number of readout channels and power consumption.

Operation of silicon sensors in daisy chains to build up detections unit as long as $\sim 1\text{ m}$ or more, is the key to cover large detection areas without increasing the number of readout channels. This approach has been used for instance in the AMS-02 experiment on the International Space Station, where $\sim 6.7\text{ m}^2$ of double sided silicon microstrip detectors are used in the tracker, and maximum length of 60cm for the single detection unit.

Upgrade of the AMS-02 experiment, with an additional layer of silicon detectors, and development of a new experiment, HERD, on the Chinese Space Station, Tiangong, will require a further step forward in sensor design, assembly and operation to cover $\sim 8\text{ m}^2$ and $\sim 64\text{ m}^2$ respectively for the two experiments. The challenge to adopt long ladder units, $\geq 1\text{ m}$, is common to the two experiments: the effect of higher strip capacitance can in fact increase the noise, spoiling efficiency and resolution.

In this thesis, the performances of the different silicon detectors units planned for the AMS-02 upgrade and the HERD experiment have been studied in different beam test campaigns. The writeup is organized as follows.

Chapter 1: provides a brief survey of cosmic rays physics, including Dark Matter and antimatter searched, as a background of the scientific objectives of the AMS-02 and HERD experiments.

Chapter 2: the AMS-02 and HERD instruments are presented, with an overview of their main components.

Chapter 3: the working principles of silicon strip detectors and related data analysis

methods are presented. In particular, will be discussed the processing of the raw signals from the microstrip detectors to search for physical signals as implemented in this thesis.

Chapter 4: describes the beam tests of silicon strip detector prototypes related to AMS-L0 and HERD, and uses the data processing methods introduced in Chapter 3 to study detector performances in terms of efficiency, position resolution and charge identification capability.

CHAPTER 1

Physical Background

1.1 Introduction to Cosmic Rays

Cosmic rays originating from outside Earth's atmosphere consist predominantly of bare atomic nuclei, stripped of their electron shells, accounting for about 99% of these rays, and a small components of electrons. A very small portion of cosmic rays includes stable antimatter particles like positrons or antiprotons. The exact composition of this small fraction, and its energy behaviour, remain an active area of research.

Among the nuclei, approximately 90% are simple protons (hydrogen nuclei), 9% are α particles (helium nuclei), and 1% are nuclei of heavier elements. The extremely wide energy range [1] of cosmic rays indicates that they have a diverse range of sources in the universe. Currently, the physics behind their origin remains poorly understood. The scientific community is advancing its understanding by developing more sophisticated space- and ground-based detection instruments, aiming for higher precision and a broader energy range in the observation of cosmic rays to unveil their mysteries.

1.1.1 Discovery of Cosmic Rays

Henri Becquerel's discovery in 1896 that uranium salts could sensitize photographic plates [2], revealing the existence of natural radioactivity, sparked extensive research

into radiation. Researchers believed that the presence of free ions in the atmosphere was a result of radiation's action.

Different theories existed regarding the source of ionizing radiation, with German scientists Julius Elster and Hans Geitel suggesting that atmospheric radiation might originate from the diffusion of radioactive radon from the soil into the air [3]. In 1901, C.T.R. Wilson proposed the idea that radiation comes from outside the Earth [4].

To verify various hypotheses, a common experimental approach involved measuring radiation levels at different altitudes. In 1909, Theodore Wolff developed a new portable electrostatic counter [5]. Using this device, he measured the ionization density at different heights of the Eiffel Tower and found that, although the ionization density at the top of the tower was lower than that at ground level, it was higher than expected. While Wolff's experiments did not provide decisive conclusions, the electrostatic counter he designed became widely used in subsequent experiments.

Following Wolff, a series of balloon experiments attempted to measure ionization density at higher altitudes, including those by Karl Bergwitz in Germany and Albert Gockel in Switzerland [6]. These experiments found a decrease in ionization density with altitude; however, it did not align well with the predicted values based on the assumption that radiation was solely from the Earth's crust.

Italian meteorologist Domenico Pacini held a skeptical view about the idea that radiation primarily originated from the Earth's crust. Considering water's ability to absorb some radiation, he designed experiments in 1910 and 1911, simultaneously measuring ionization density at different locations, such as on land, at the water's surface, and underwater at a depth of 3 meters [7]. Observing a relative decrease in ionization density underwater compared to that on land, Pacini suggested that a considerable portion of ionization should be caused by radiation from beyond the Earth's crust.

Austrian physicist Victor Hess provided decisive evidence for the radiation source issue. In 1911 and 1912, he conducted a series of balloon experiments, systematically measuring ionization rates up to an altitude of 5300 meters using a Wolff-type electrostatic counter. He observed a gradual decrease in ionization rates below 1000 meters, followed by a significant increase, with the intensity reaching double that observed at ground level at around 5000 meters [8]. Following this, German physicist Werner Kolhörster, in experiments conducted from 1913 to 1914, further discovered that radiation levels at 9300 meters could be 40 times higher than at ground level [9]. From these results, Hess concluded that highly penetrating radiation must be entering the

atmosphere from space. Due to his contribution to the discovery of cosmic radiation, Victor Hess was awarded the Nobel Prize in Physics in 1936.

Since that time, extensive research on cosmic rays has been conducted, including ground array experiments, telescope experiments, high-altitude balloon experiments, and even space satellite experiments. These experiments have gradually revealed the true nature of cosmic rays and made significant contributions to understanding their composition, exploring their origins, investigating acceleration mechanisms, and studying their propagation.

1.1.2 Cosmic Rays Spectrum

The energy spectrum of all-particle cosmic rays, as illustrated in Figure 1.1, stands as one of the most remarkable achievements in experimental astrophysics research.

From Figure 1.1, it can be observed that, except for the portion modulated by solar activity at energies lower than approximately 10 GeV, the energy spectrum distribution

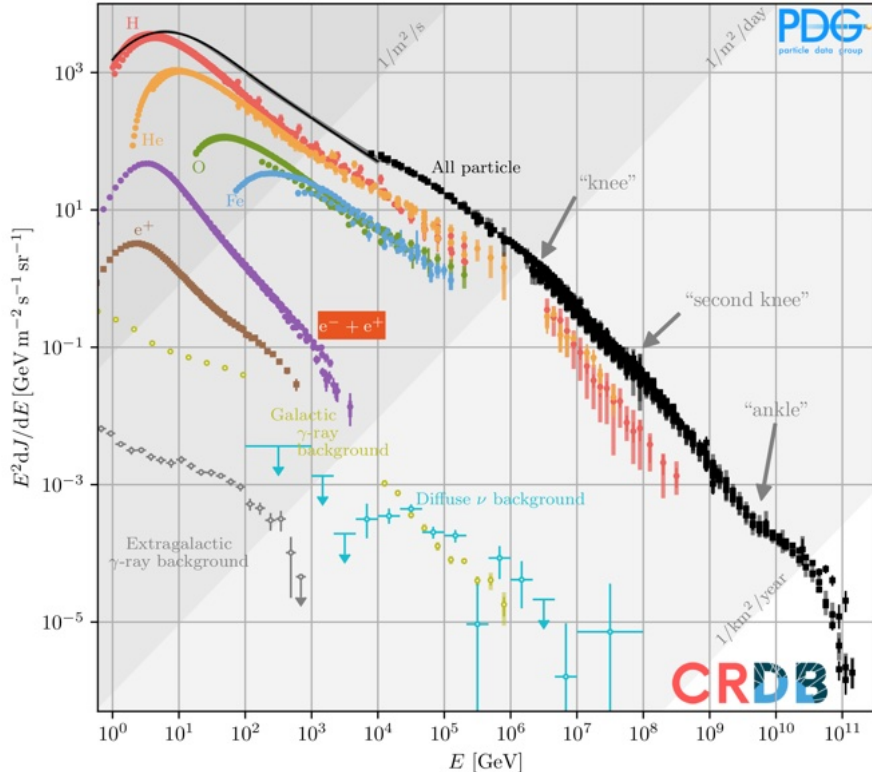


Figure (1.1) – The spectrum of cosmic rays (CRs) [10].

of cosmic rays approximately follows a power-law pattern, where the flux¹ of particles rapidly decreases as energy increases. Specifically, the number of particles with energy E can be expressed as:

$$\Phi = \Phi_0 E^{-\gamma} \quad (1.1)$$

where γ is the spectral index, usually ranging between 2.6 and 3.1.

The spectrum presents three spectral features, the first feature is the "Knee," which appears around an energy level of 10^{15} eV. At the Knee, the slope of the spectrum becomes steeper, indicating a faster decrease in the number of high-energy cosmic rays. This phenomenon is generally believed to be related to the propagation or acceleration mechanisms of cosmic rays within the Milky Way, possibly suggesting that certain physical processes within the galaxy exert a stronger influence on cosmic rays at this energy [11, 12].

Next is the "Ankle", located at approximately 10^{18} eV, where the slope of the spectrum changes again, becoming flatter. It is generally believed that this marks the energy range where extragalactic ultra-high-energy cosmic rays begin to dominate. This discovery provides crucial clues for studying the origins of cosmic rays, particularly those of ultra-high energies.

Moreover, at energy levels above 10^{19} eV, there is broad consensus that a sharp cutoff in the cosmic ray spectrum, known as the "Greisen-Zatsepin-Kuzmin (GZK) cutoff" [13], exists. This cutoff is caused by energy loss due to interactions between these ultra-high-energy particles and the cosmic microwave background (CMB) radiation. Recent experimental results have confirmed the existence of the GZK cutoff [14].

From the experimental point of view, the study of charged cosmic rays can be essentially conducted in two quite different ways that correspond to two significantly different and complementary experimental techniques:

- indirect measurement on ground - this is typically used when the fluxes are very low, that correspond to energies that are larger than 10^{14-15} eV, so around and above the 'knee'. Generally the detectors used are water Cherenkov tanks, or in general detectors capable to detect the components of the air shower initiated by

¹Cosmic ray flux refers to the number of cosmic ray particles passing through a unit area per unit time. It is mathematically expressed as: $\Phi = dN / (dA \cdot dt \cdot d\Omega)$. $d\Omega$ is the unit of solid angle, dt is the unit of time, dA is the unit of measured area, dN is the number of particles detected within the time interval dt , passing through the area element dA , and within the solid angle $d\Omega$.

the primary CR particle, arranged in sparse arrays to cover several km^2 to collect some statistics even when the rate of particles is at the $1 \text{ km}^{-1} \text{ yr}^{-1}$ level. Another approach used on ground is to detect the fluorescence light that is produced during the extensive air shower development. These techniques are addressed as “indirect” since the real detected particles are only the ones created in the shower and the characteristics of the primary particle can be inferred only on statistical basic (for example no discrimination between particle and antiparticles is possible);

- direct measurement in space or on stratospheric balloon - this is possible when the primary flux is large enough to have a certain amount of statistics with detector with a geometrical factor of fractions of or few $\text{m}^2 \text{ sr}$ and exposure times that cannot exceed few weeks for a balloon flight or few years for a detector in orbit. In this case the detectors used are typically the ones coming from the High Energy Particles Physics and the characteristics of the primary particles can be measured at the single event level. This is the only way to access experimentally the rarest components of Cosmic Rays (such as positrons, anti-protons, deuterium, ...), to search for components not yet observed experimentally (such as anti-deuterons, anti-Helium and in general heavy antimatter) and to measure with high accuracy the spectral features of all the different species, even the different isotopes of the same nuclear species.

The “knee” being a sort of de-facto separation between the direct and indirect measurement is just a coincidence and has not any particular motivation. One of the goals of the direct measurement community is to extend the direct measurements above the knee and to measure also the not more abundant components (protons and Helium) at the knee: this requires larger experiments in space and the design of detectors with large fields of view (ideally the whole solid angle) and able to exploit the larger possible effective areas once fixed, by the load weight capacity and the ogive size of the launcher, the volume of the apparatus. This will be discussed in more details in Chap.2.

1.1.3 Origin of Galactic Cosmic Rays

The current cosmological theory posits that the formation of elements primarily involves two key processes: Big Bang Nucleosynthesis (BBN) [15] and stellar nucleosynthesis [16]. Light elements (namely deuterium, helium, and lithium) were produced in the first few minutes after the Big Bang, while elements heavier than helium are thought

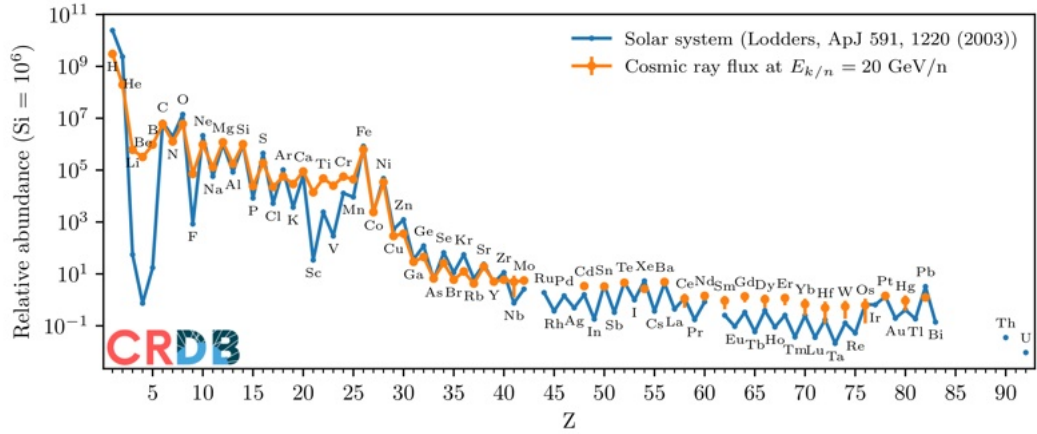


Figure (1.2) – Comparison between the relative abundance of atomic nuclei in cosmic rays and that in the solar system [17].

to have originated in the interiors of stars that formed much later in the history of the universe.

The theory of stellar nucleosynthesis indicates that heavier elements are primarily formed within stars through nuclear fusion and nucleosynthesis processes. The life cycle of a star involves multiple stages, starting with the fusion of hydrogen and helium, gradually forming heavier elements such as ^{12}C , ^{16}O , and ^{56}Fe : these are the elements typically addressed as “primary” cosmic rays. ^{56}Fe is the heaviest element that can be produced through stellar nucleosynthesis, while even heavier elements are believed to form during supernova explosions, scattering into the cosmic space through collisions and ejections.

Figure 1.2 compares the relative abundance of atomic nuclei in cosmic rays with that in the solar system. Elements such as Li, Be, B, and Fe exhibit abundances far exceeding those found in the solar system. These elements are therefore believed to be produced by collision reactions between primordial cosmic rays and interstellar matter during their propagation, and are referred to as “secondary” cosmic rays.

1.1.4 Acceleration of Galactic Cosmic Rays

All nuclei fluxes in primary cosmic rays display a consistent power-law spectrum, indicating a common acceleration mechanism. To account for this observation, Enrico Fermi introduced the concept of “Fermi acceleration” in 1949 [18]. This theory posits that

charged particles gain energy by interacting with randomly moving magnetic clouds in interstellar space. When a particle collides head-on with a magnetic cloud, it is reflected, and its kinetic energy increases. Conversely, if a particle collides with the trailing side of a magnetic cloud, it slows down. Because high-energy particles follow longer paths in magnetic turbulence and experience more collisions, and because fast-moving particles are more likely than slow-moving ones to undergo significant momentum exchange and gain more energy, the probability of energy gain is slightly higher than that of energy loss in a statistical sense. This process results in the acceleration of particles in interstellar space, which accounts for the observed power-law spectrum of primary cosmic rays.

Assuming a particle with an initial energy of E undergoes scattering with a massive scattering center (SC) moving at a velocity of β_M , when the particle undergoes a tail-on collision with the scattering center, the energy of the particle becomes

$$E_1 = \gamma_m E (1 - \beta_M \cos \theta_1) \quad (1.2)$$

In the equation, $\gamma_m = (1 - \beta_M^2)^{-1/2}$ represents the Lorentz factor of the scattering center, and θ is the angle between the velocity vectors of the particle and the scattering center. It can be observed that the contribution of tail-on collisions to the change in kinetic energy is negative, leading to a decrease in the particle's kinetic energy. Subsequently, when they undergo head-on collisions, the energy of the particle becomes

$$E_2 = \gamma_m E_1 (1 + \beta_M \cos \theta_2) \quad (1.3)$$

In this second scenario, the particle gains energy and accelerates. After multiple collisions, the average increment in the particle's kinetic energy is

$$\frac{dE}{E} \approx \frac{4}{3} \beta_M^2 \quad (1.4)$$

Due to the proportionality of particle acceleration with the square of the velocity of the magnetic cloud in this equation, this acceleration mechanism is also referred to as the Second-order Fermi Acceleration mechanism. For non-relativistic particles, after N acceleration events, their energy is

$$E = mc^2 e^{\beta_M^2 N} \quad (1.5)$$

In the equation, m represents the mass of the particle. During the propagation of particles in cosmic space, there is a certain probability of interacting with interstellar matter and transforming into other particles. Therefore, the survival time of particles will follow a Poisson distribution.

$$f(t; T) = \frac{1}{T} e^{-t/T} \quad (1.6)$$

In the equation, T denotes the average lifespan of the particle. By incorporating Formula 1.5, it becomes possible to compute the particle's energy at a given moment t .

$$E(t) = mc^2 e^{\beta_M^2 t / \tau} \quad (1.7)$$

In the equation, τ represents the average time interval between collisions of the particle with magnetic clouds. The probability of observing the particle's energy falling within the range from E to $E + dE$ is given by:

$$p(E) dE = (\tau / \beta_M^2 T) (mc^2)^{\tau / \beta_M^2 T} dE / E^{1 + \tau / \beta_M^2 T} \quad (1.8)$$

Usually, $1 + \tau / \beta_M^2 T$ is represented by γ , and thus, the flux of cosmic rays will follow the following power-law spectrum.

$$\frac{dN}{dE} \propto E^{-\gamma} \quad (1.9)$$

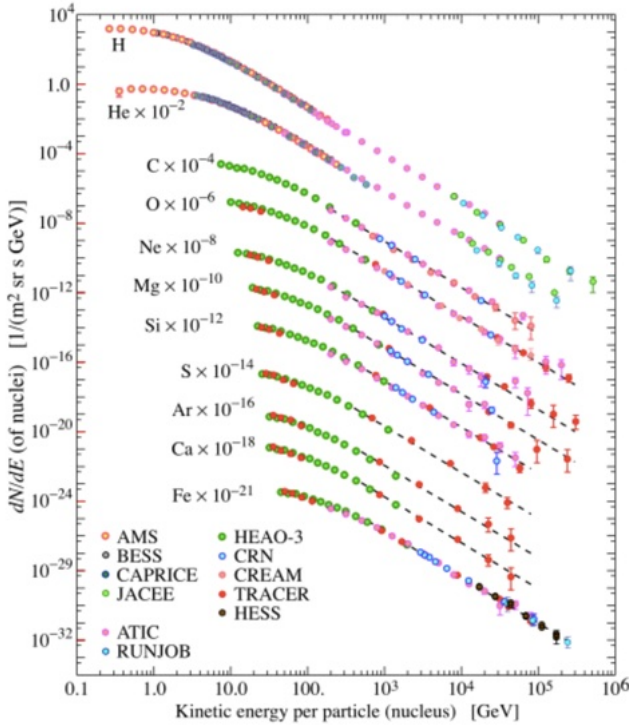


Figure (1.3) – Fluxes of primary cosmic nuclei radiation plotted as a function of the kinetic energy [19].

This is consistent with the observed form of cosmic ray spectrum. However, this theory still has many limitations. Firstly, its acceleration process is very slow, with particles having only a few opportunities for acceleration during their travel, resulting in a very low acceleration efficiency. Secondly, due to the energy loss caused by ionization during collision processes, and the fact that larger mass particles experience higher energy losses, this cannot explain the observed results in Figure 1.3, where all particles follow the same power-law spectrum form.

Therefore, a new mechanism is needed to ensure that particle acceleration occurs with each collision. A simple model is as follows: two scattering centers are separated by a distance L , moving towards each other with a velocity V . A particle with mass m and velocity $v \gg V$ reflects back and forth between the scattering centers. In this way, each collision for the particle is a head-on collision, and its energy increment rate is

$$\frac{dE}{dt} = n \times \delta E \quad (1.10)$$

Here, n is the number of collisions per unit time, and δE represents the energy gained by the particle in each collision.

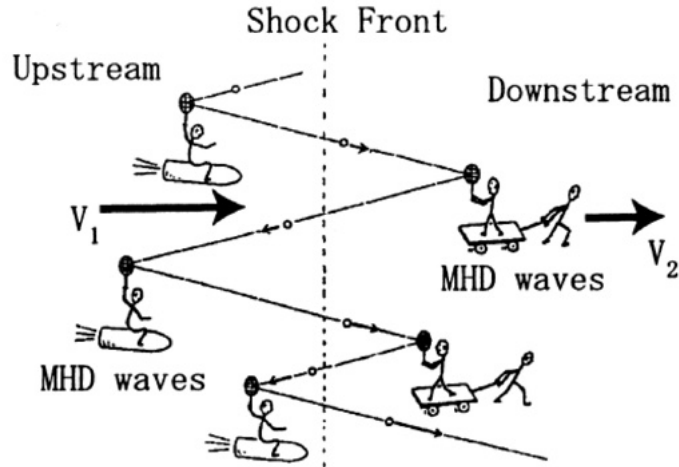


Figure (1.4) – A cartoon of the diffusive shock acceleration mechanism [21].

For high-speed moving particles, the increase in momentum per collision is represented by $\gamma m V$. Therefore, Equation 1.10 can be approximated as follows:

$$\frac{dE}{dt} \approx \frac{v}{L} \times \gamma m V c \approx \frac{\gamma m c^2 V}{L} \approx \frac{EV}{L} = \frac{E}{\tau} \quad (1.11)$$

From the above equation, it can be observed that the energy of particles increases exponentially. Therefore, when a large number of particles are accelerated by the same scattering center, particles with slightly higher initial energy will ultimately gain significantly more energy than those with lower initial energy.

The currently accepted and widely acknowledged theory that conforms to this model is the shock wave acceleration mechanism [20]. A shock wave is a form of turbulent propagation. When a star's internal fuel is depleted and can no longer support its massive outer shell, the shell collapses toward the center and is then ejected at speeds far exceeding the speed of sound, generating a powerful shock wave. The basic shock wave model is illustrated in Figure 1.4, where the region traversed by the shock wave is defined as downstream, and the area not traversed is upstream.

When particles are trapped between the upstream and downstream of the shock wave, undergoing repeated reflections, they will continue to be accelerated until they escape. In the shock wave transition region, the mass through the unit shock wave surface is conserved:

$$\rho_u v_u = \rho_d v_d \quad (1.12)$$

where ρ_u, ρ_d are the densities of the gas before and after the shock wave, respectively. and v_u, v_d are the velocities of the gas before and after the shock wave, respectively. Because the shock wave surface remains stationary in its own reference frame, the momentum upstream and downstream is conserved,

$$\rho_u v_u^2 = P_d + \rho_d v_d^2 \quad (1.13)$$

In the equation, P_d represents the pressure in the downstream. The expansion in the downstream performs work on the shock wave surface, and the energy is conserved,

$$\frac{1}{2} \rho_u v_u^3 - \left(\frac{1}{2} + \rho_d v_d^3 + \frac{\gamma}{\gamma-1} P_d v_d \right) = v_d P_d \quad (1.14)$$

In the equation, γ represents the ratio of specific heat at constant pressure to specific heat at constant volume, with a theoretical value denoted as $(n+2)/n$, where n stands for the number of degrees of freedom for the microscopic motion of gas molecules, and for high-speed shock waves, considering gas with one degree of freedom, we have $\gamma=3$. Through rearranging equations 1.12, 1.13, and 1.14, we can obtain

$$\left(\frac{\rho_d}{\rho_u} - 4 \right) \left(\frac{\rho_d}{\rho_u} - 1 \right) = 0 \quad (1.15)$$

Therefore, in the reference frame where the upstream is stationary, the shock wave approaches with a velocity of v_u , and the downstream gas also approaches with a velocity of $\frac{3}{4}v_u$. When a particle traverses the shock wave and encounters the downstream gas, it is reflected and its velocity increases by $\frac{3}{4}v_u$. In the reference frame where the downstream is stationary, the upstream gas is also approaching with a velocity of $\frac{3}{4}v_u$. When the reflected particle collides again with the upstream gas, it is once again reflected and gains a velocity increment of $\frac{3}{4}v_u$.

Assuming that the particle's energy increases by a factor of α each time it traverses the shock wave, after n accelerations, the energy of a particle with an initial energy of E_0 would be:

$$E = E_0 \alpha^n \quad (1.16)$$

In the process of shock wave acceleration, there is a certain probability that particles escape from the acceleration region. Assuming the probability of a particle remaining in the acceleration region after each acceleration is P , after n accelerations, the number of particles remaining out of the initial N_0 particles would be:

$$N = N_0 P^n \quad (1.17)$$

After rearranging, we obtain:

$$\frac{N}{N_0} = \left(\frac{E}{E_0} \right)^{\frac{\log P}{\log \alpha}} \quad (1.18)$$

Expressed in differential form as:

$$N(E) dE \propto E^{-k} dE \quad (1.19)$$

In the equation, where $k = 2$, it closely aligns with the currently measured power spectrum index of 2.7. Since the energy gained by particles in each acceleration is proportional to the shock wave velocity, this theory is also referred to as the first-order Fermi acceleration mechanism. Its acceleration efficiency is significantly higher than second-order Fermi acceleration, and the attainable final energy is also higher.

1.1.5 Propagation of Galactic Rays

Once particles are accelerated and escape into the cosmic space, they may encounter various unknown interstellar materials, dynamic magnetic fields, and electric fields. These processes occur unpredictably and continuously alter the particle's energy and trajectory, potentially leading to particle fragmentation reactions and transformation into other types of particles. Taking into account the potential influences on cosmic rays within the galaxy, the propagation equation for a particular particle species is typically formulated as follows [22]:

$$\begin{aligned} \frac{\partial \Psi_i(x, p, t)}{\partial t} &= q_i(x, p) + \nabla \cdot (D_{xx} \nabla \Psi_i - \mathbf{V} \Psi_i) + \frac{\partial}{\partial p} p^2 D_{pp} \frac{\partial}{\partial p} \frac{1}{p^2} \Psi_i \\ &\quad - \frac{\partial}{\partial p} \left[\dot{p} \Psi_i - \frac{p}{3} (\nabla \cdot \mathbf{V}) \Psi_i \right] - \frac{1}{\tau_{f,i}} \Psi_i - \frac{1}{\tau_{r,i}} \Psi_i \end{aligned} \quad (1.20)$$

In the above formula:

- $\psi_i(x, p, t)$ represents the number density of a particular cosmic ray particle species per unit momentum;
- $q_i(x, p)$ represents the cosmic ray source term, generally considered to be pulsars and supernovae. The energy injection into cosmic rays is assumed to follow a power-law spectrum $\frac{\partial q}{\partial p} \propto p^{-\gamma}$;
- $D_{xx} = \frac{1}{3}\lambda_D v$ represents the diffusion coefficient of cosmic rays in the magnetic field, where λ_D is the mean free path, v is the particle velocity, and V is the cosmic ray convection velocity, typically assumed to be 20 km/s;
- D_{pp} represents the secondary acceleration coefficient of cosmic rays in the magnetic field, determined by the local irregularities of the magnetic field;
- $\dot{p} = dp/dt$ represents the energy loss of cosmic rays, including ionization, Coulomb energy loss, inverse Compton effect, and synchrotron radiation;
- $\tau_{f,i}$ is the time scale for loss by fragmentation;
- $\tau_{r,i}$ is the time scale for radioactive decay

Equation 1.20 encompasses various issues that may be encountered during the propagation of cosmic rays, making direct solutions very challenging.

Currently, one popular method is the GALPROP code [23], which serves as an open-source tool for simulating the propagation of cosmic rays within the Milky Way galaxy. Its primary functionalities encompass cosmic ray source modeling, diffusion processes, and interaction simulations. The code is capable of calculating the propagation dynamics of cosmic rays in the galaxy, accounting for factors such as diffusion, convection, and energy loss, while generating energy spectra and spatial distributions for various particle types. Furthermore, GALPROP can model the high-energy gamma rays produced by the interactions of cosmic rays with the interstellar medium, thereby providing a significant resource for research in cosmic ray physics and high-energy astrophysics.

The Leaky Box model [24] was proposed in the 1960s to simplify the calculations of cosmic ray propagation. In this model, cosmic rays are confined within a specific region of cosmic space, where particles can propagate freely and escape this confined space with a constant probability. The Galactic magnetic field is considered the main factor confining and mixing cosmic rays. The model includes the following assumptions: the boundary of the Galaxy has strong reflective properties, so long-lived cosmic ray particles will encounter this boundary multiple times before escaping the Galaxy; the

probability of various cosmic ray nuclei escaping the Galaxy at the boundary is the same; and the escape process of cosmic rays follows a Poisson distribution.

Using the Leaky Box model, equation 1.20 can be simplified to

$$\frac{\partial \Psi_i}{\partial t} = q_i - \frac{1}{\tau_{esc}} \Psi_i - \sum_{j>i} \frac{1}{\tau_{j,i}} \Psi_j - \frac{1}{\tau_i} \Psi_i \quad (1.21)$$

In the above equation, $\tau_{j,i}$ represents the characteristic time for the fragmentation or decay of nuclide j into nuclide i , τ_i represents the characteristic time for the transformation of nuclide i into other nuclides, and τ_{esc} denotes the escape time. Under steady-state conditions, $\frac{\partial \Psi_i}{\partial t} = 0$.

For primary cosmic rays, their abundance is much greater than that of secondary cosmic rays. Therefore, $\tau_{j,i}$ in equation 1.21 can be neglected, allowing us to deduce the relationship between the observed energy spectrum Ψ_i and the energy spectrum q_i produced by the cosmic ray sources as follows:

$$\Psi_i = \frac{q_i \tau_{esc}}{1 + \tau_{esc}/\tau_i} \quad (1.22)$$

For secondary cosmic rays, q_i can be neglected, so τ_{esc} can be expressed as:

$$\tau_{esc} = \left(\frac{\sum_{j>i} \frac{1}{\tau_{j,i}} \Psi_j}{\Psi_i} - \frac{1}{\tau_i} \right)^{-1} \quad (1.23)$$

From equation 1.23, it can be seen that by measuring the flux ratio of secondary to primary cosmic rays, the cosmic ray escape time can be determined. By adjusting parameters such as the escape time, the Leaky Box model can then be used to explain most cosmic ray measurement results. Therefore, more precise measurements of the secondary-to-primary cosmic ray ratio can more effectively constrain certain parameters within propagation models, which is of great importance for a deeper understanding of the cosmic ray propagation process.

1.2 Dark Matter

The Cosmic Microwave Background (CMB) [26] originates from the thermal radiation emitted by the primordial plasma remaining from the Big Bang [27], approximately 380 kyears after its occurrence. The observations of the CMB provide crucial evidence for the evolution of the universe and contributed to the establishment of the Big Bang

theory. Modern cosmological theories suggest that after the Big Bang, the temperature and pressure of the primordial gas were too high for small structures like celestial bodies to form. It required the involvement of non-relativistic (cold) Dark Matter (DM) [28] in the formation of large-scale structures to eventually evolve into the current cosmic structure. In general, the temperature distribution of the current universe is uniform and isotropic. However, within certain ranges, there are still temperature fluctuations, as shown in Figure 1.5. High-resolution measurements of these temperature fluctuations can provide key insights into the early evolution of the universe. Theoretically, the anisotropy of the CMB can be seen as the result of acoustic oscillations caused by collisions between photons and baryon plasmas under the influence of gravity in the early universe [29]. Additionally, gravitational interactions between baryonic matter and DM also play a role in the CMB anisotropy. Using the Λ CDM [30] cosmological model, it is possible to determine the density parameters of baryonic matter, DM and dark energy [31]. All visible matter accounts for only 4.9% of the total energy in the universe, while dark energy comprises 68.3%, and dark matter accounts for 26.8%.

1.2.1 Observational Evidence for DM

At present, the fundamental composition of most DM remains unknown. Assuming the validity of General Relativity, DM has been observed to be pervasive in gravitationally collapsed structures, ranging in size from the smallest known galaxies [32], to galaxies comparable to the size of the Milky Way [33], and to groups and clusters of galaxies [34]. In such collapsed structures, the existence of DM is directly inferred using mass

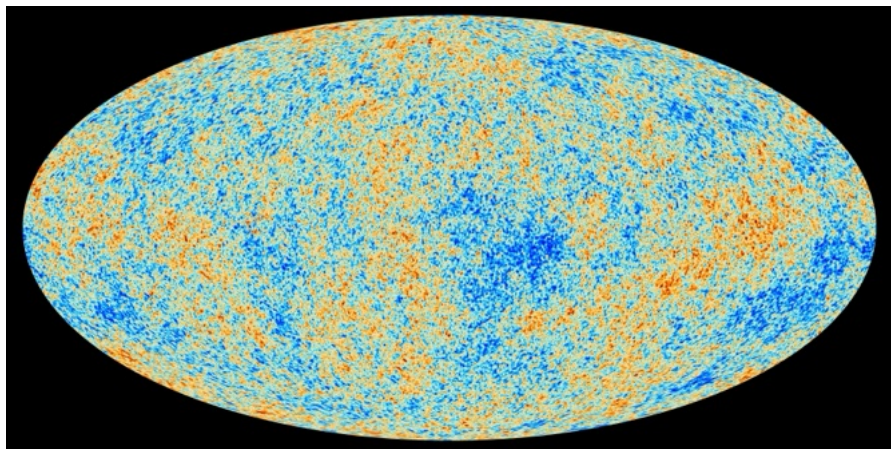


Figure (1.5) – The map of temperature fluctuations in the cosmic microwave background [25].

tracers within a certain radius, such as stellar velocity dispersion, rotation curves [33] in axisymmetric systems, the virial theorem, gravitational lensing [35], and measurements of non-dark matter (i.e., baryonic) mass, such as stellar number counts and gas density tracers like X-ray emission [36].

1.2.2 Detection of DM

Currently, most DM detection experiments are based on the aforementioned WIMP particles, which are believed to interact via weak interactions. Detection methods are divided into three types,

- Collider detection: High-energy particle colliders, such as the Large Hadron Collider (LHC) [37], can potentially produce dark matter candidate particles. If these particles interact weakly and do not leave direct traces in the detector, an imbalance in energy and momentum can be observed, indirectly suggesting their existence.
- Indirect detection: Indirect detection searches for secondary particles (such as gamma rays, antiprotons, positrons, and neutrinos) produced by the annihilation or decay of dark matter. These signals may originate from regions with high dark matter density, such as the galactic center, dwarf galaxies, or the Sun.
- Direct detection: Direct detection experiments aim to observe interactions between dark matter particles and ordinary matter (such as atomic nuclei). These experiments are typically conducted in deep underground laboratories to reduce cosmic ray interference. If dark matter particles, such as Weakly Interacting Massive Particles (WIMPs), exist, they may elastically scatter off atomic nuclei in the detector, producing detectable energy deposits.

HERD [38] experiment will measure the “all-electron” (positron plus electron) energy spectrum in cosmic space, and the AMS-02 [39] experiment can measure the antiproton and positron energy spectra in cosmic space. Figure 1.6 show the proton, antiproton, electron, and positron spectrum observed by the AMS-02 experiment.

1.3 Antimatter

Ordinary matter is composed of regular particles, while antimatter consists of their corresponding antiparticles. Each particle has a corresponding antiparticle that shares

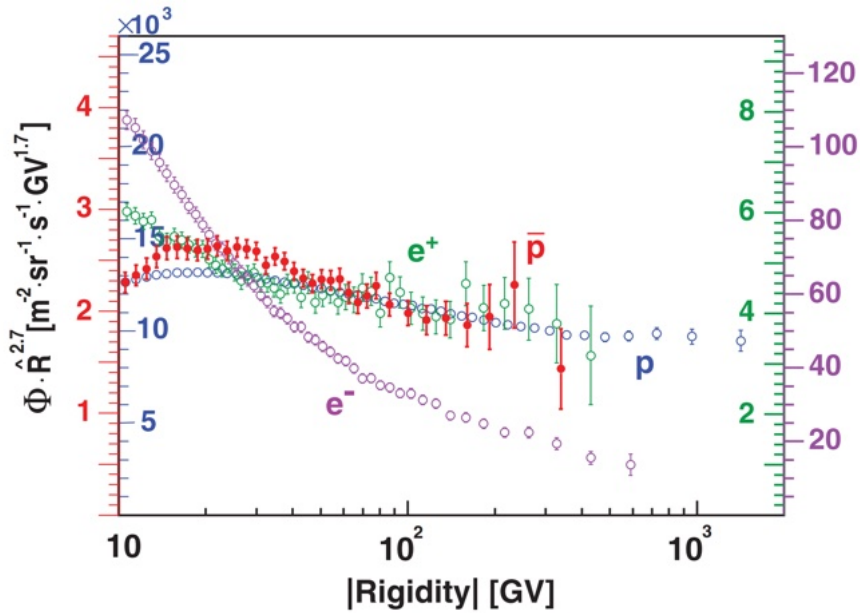


Figure (1.6) – The antiproton flux (red, left axis) compared to the proton flux (blue, left axis), the electron flux (purple, right axis), and the positron flux (green, right axis) measured by AMS-02 [40].

the same mass and most physical properties, with the only difference being their opposite electric charge. In the currently observable universe, ordinary matter seems to dominate, while antimatter appears to be extremely scarce.

According to the Big Bang theory, the early universe should have generated equal amounts of matter and antimatter. However, current observations indicate that the universe is almost entirely dominated by matter, revealing a significant matter-antimatter asymmetry. This asymmetry remains one of the fundamental unresolved questions in particle physics and cosmology. Therefore, the search for antimatter and the study of its properties have long been major scientific pursuits.

1.3.1 History of Antimatter Discovery

The modern theory of antimatter began in 1928 with a paper by Paul Dirac [41]. Dirac realized that the relativistic version of the Schrödinger wave equation for the electron, which he proposed, predicted the possible existence of the positron. Although Dirac laid the theoretical foundation for the existence of these “antielectrons” he did not initially fully grasp the implications of his equation.

After the antiparticle solutions of Dirac's equation were proposed, in 1932, American physicist Carl Anderson observed the positron for the first time in cosmic ray experiments [42], marking the first discovery of an antiparticle in human history and the beginning of antimatter research. For this achievement, Anderson was awarded the Nobel Prize in Physics in 1936.

In 1955, Emilio Segrè and Owen Chamberlain successfully discovered the antiproton using a cyclotron at the Lawrence Radiation Laboratory at the University of California [43]. Their discovery earned them the Nobel Prize in Physics in 1959. In 1965, a research team led by Samuel Ting successfully detected the antideuteron using the Alternating Gradient Synchrotron (BNL-AGS) at Brookhaven National Laboratory [44].

In 1971, Soviet scientists observed anti-helium-3 and further studied the relationship between the production cross-sections of antiprotons, antideuterons, and anti-helium-3 as a function of their mass number [45]. The study found that as the mass number increases, the production cross-section of antimatter nuclei decreases by several orders of magnitude. Consequently, under the same experimental conditions, detecting heavier antimatter nuclei requires significantly higher experimental statistics. Due to this limitation, anti-helium-4 was only successfully discovered decades later in 2011 by the RHIC-STAR experiment group at Brookhaven National Laboratory [46].

In 2010, the RHIC-STAR experiment group made another breakthrough by discovering the first-ever antihypernucleus — the anti-hypertriton [47]. This hypernucleus consists of an antiproton, an antineutron, and an anti-Lambda (Λ) particle, which contains a second-generation quark—the strange quark. This was the first time a nucleus containing a strange quark in antimatter had been discovered, providing crucial experimental evidence for studying the properties of antimatter and strong interactions.

In 2024, the RHIC-STAR collaboration made another significant discovery: an antimatter hypernucleus, the “anti-hyperhydrogen-4”, which is currently the heaviest antimatter hypernucleus observed experimentally. Anti-hyperhydrogen-4 consists of one antiproton, two antineutrons, and one anti-Lambda (Λ) hyperon. Compared to its corresponding matter counterpart, hyperhydrogen-4, no significant difference in lifetime was observed, further confirming the symmetry between matter and antimatter properties [48].

1.3.2 Observation in cosmic rays

The antiparticles in cosmic rays primarily originate from the collisions of high-energy protons with the interstellar medium, through hadronic decay, producing antiparticles such as antiprotons and positrons. In recent years, several important detection projects have been conducted to study these antiparticles in depth. For example, HEAT (High-Energy Antimatter Telescope) [49] is a high-altitude balloon experiment designed to detect antiparticles in cosmic rays, with the main objective of measuring the energy spectra of positrons and antiprotons to investigate their sources and the propagation mechanisms of cosmic rays. HEAT conducted two high-altitude balloon flights in 1994 and 1995, during which it detected an excess of high-energy positrons. PAMELA (Payload for Antimatter Matter Exploration and Light-nuclei Astrophysics) [50] is an orbital satellite experiment launched in 2006, which is mounted on the Russian Resurs-DK1 [51] satellite and aimed at studying antiparticles and light nuclei in cosmic rays. The main goal of this experiment is to monitor the composition of cosmic rays, including antiprotons, positrons, and light nuclei such as helium. One significant finding from PAMELA is the discovery of an anomalous increase in the abundance of positrons, possibly related to dark matter annihilation or pulsars.

In 2011, the Alpha Magnetic Spectrometer (AMS-02) [52] was successfully installed on the International Space Station. AMS-02 conducted high-precision measurements of positrons and antiprotons in cosmic rays and confirmed the high-energy positron excess previously detected by HEAT. Figure 1.7 shows the positron spectrum measured by AMS-02. In this figure, $\tilde{E}^3 \Phi_{e^+}$ (red data points) is shown as a function of energy. \tilde{E} is the spectrally weighted mean energy for a flux E^{-3} . The time variation of the flux at low energies due to solar modulation is indicated by the red band. To guide the eye, the vertical color bands indicate the energy ranges corresponding to changing behavior of the spectrum: flattening, rising, and falling [39]. The complex behavior of the positron flux in the figure does not conform to the secondary production model, which attributes positrons solely to collisions of cosmic rays.

One of the primary objectives of AMS-02 is the search for antihelium. Compared to lighter antiparticles such as antiprotons and positrons, which can be produced through interactions between cosmic rays and the interstellar medium [53], the composition of antihelium is more complex. As a result, the abundance of antihelium is expected to be extremely low. However, AMS-02 has observed antihelium events that exceed the predictions based on standard cosmic ray interactions by several orders of magnitude. Furthermore, the detected antihelium nuclei consist of two different isotopes:

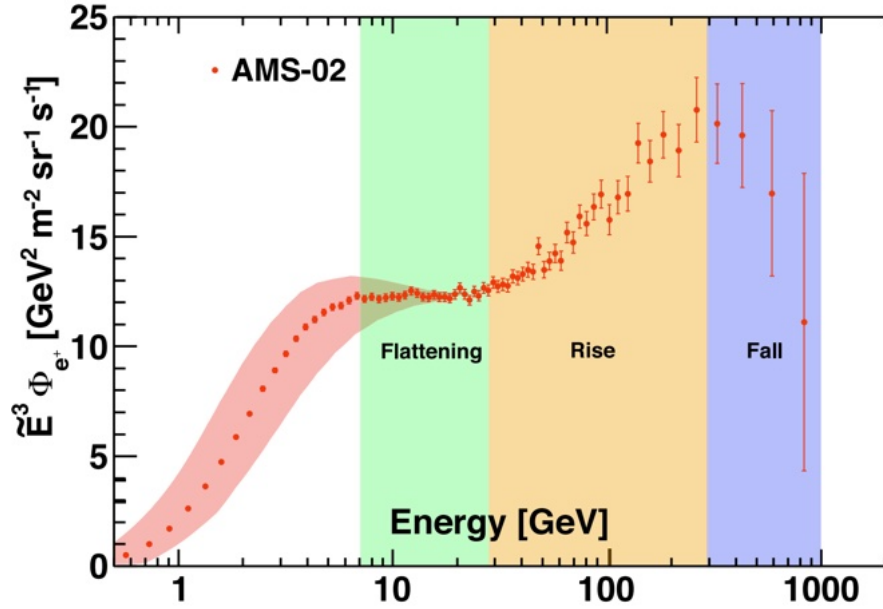


Figure (1.7) – the positron spectrum measured by AMS-02 [39].

antihelium-3 and antihelium-4. In particular, antihelium-4 is heavier and even rarer. While the annihilation model of weakly interacting massive particles can account for the detected amount of antihelium-3, it fails to explain the presence of antihelium-4. Therefore, antihelium-4 is highly likely to originate from an antimatter-dominated region [54].

CHAPTER 2

Space borne cosmic ray detectors

This thesis is focused on the study, characterization and development of analysis algorithms and approaches related to detectors, the silicon trackers, that are largely used in direct measurement experiments. Generally two approaches are explored for stratospheric/space instruments: the purely calorimetric measurement and the spectrometric one. The latter involves trackers, almost always based on silicon sensors, with high accuracy to measure the Rigidity of the particles inside the magnetic field of the spectrometer. The former, instead, don't need trackers with state-of-the-art (below $10 \mu\text{m}$) spatial resolutions, but still a silicon tracker (with spatial resolution at the level of $30\text{-}40 \mu\text{m}$) is a valuable, and often preferred to different solutions (as for example a gas drift chamber) for their easiness in terms of mechanical assembly, operation (as the absence of high voltages) and robustness to the challenging conditions of the launch to space or of the in orbit environment.

Silicon microstrip sensors are used in space born instruments since the early 2000s to accurately measure trajectory and absolute charge of the traversing particles. This choice appeared somewhat mandatory for planning long term missions in space, where traditional gas based detectors - used in balloon based experiments - could lead to safety issues and limited operation lifetime in case of gas leaks.

In this chapter we will briefly review two large sized experiments: AMS-02 [52], operating on board the International Space Station (ISS), and HERD [38], planned to operate on board the Chinese Space Station (CSS). Indeed, both experiments use microstrip silicon

sensors and, in this thesis, the performance of silicon detectors for these experiments has been studied.

2.1 The AMS-02 Experiment

The Alpha Magnetic Spectrometer (AMS) experiment was proposed in 1995 [56] with the objective of a precise study of antimatter particles in cosmic rays, applying in space the state of the art detection techniques adopted in high energy experiments at colliders. In particular, the use of a silicon sensors was proposed to reconstruct the track of charged CR in the magnetic field of a permanent magnet. In June 1998, a simplified version, known as AMS-01, was designed and successfully launched into space aboard the Space Shuttle Discovery, orbiting the Earth for ten days. The successful operation of the AMS-01 silicon tracker in this precursor flight, and the scientific results from this limited data taking period [57], validated the AMS project approach. The current operational version, AMS-02, was collaboratively designed and constructed by 56 research institutions from 16 countries. It was launched into space on May 16, 2011, aboard the Space Shuttle Endeavour and successfully installed on the International Space Station (ISS) on the 19th of May, As shown in Figure 2.1. About 250 billion cosmic rays have been collected by AMS-02 in nearly 14 years of data taking, and new data will be continuously collected until the decommissioning of the ISS.

The primary physics objective of AMS-02 is to search for antimatter particles in cosmic rays, anti nuclei with $Z \geq 2$ to investigate the existence of primordial antimatter signals, or positrons and anti-protons, anti-deuterons eventually produced in the

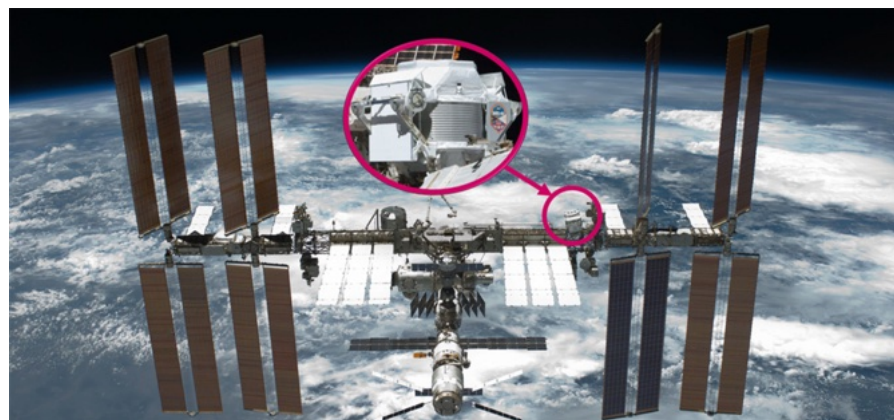


Figure (2.1) – AMS-02 on the International Space Station[55].

annihilation of dark matter particles. Currently, AMS-02 has measured antiproton and positron fluxes up to 525 GV and 1000 GV [39]. The unprecedented accuracy and the maximum energy achieved in these measurements has challenged current understanding of the origin of these cosmic particles since their fluxes exceed the expected level of secondary production from CRs collisions in the Inter Stellar Medium (ISM).

Precision measurements of all CRs components, nuclei and electrons, up to TeV energies are among the physics goals since can shed light on the acceleration and propagation mechanisms of the CRs in the galaxy. This knowledge is mandatory to evaluate secondary production of light anti-matter (anti-protons, positrons). Indeed, unexpected spectral features in different nuclear species, of primary and secondary origin, have been observed by AMS-02, with similar spectral behaviour in different *classes* of primary CR components [39].

These measurements have been possible thanks to a redundant approach in measuring the particle properties, absolute charge (Z), velocity and energy, while distinguishing e^\pm components from the p/\bar{p} , with different detectors. The magnetic spectrometer, a permanent magnet to bend CR trajectories and 9 layers of silicon sensors, is the core of AMS-02 and the key for particle/anti-particle separation.

Current measurements of AMS-02 at the higher energies are limited by statistics, i.e. by the tracker acceptance. In 2023 an effort has been started to integrate a new large sized plane of silicon sensors on top of the instrument to enhance the tracker acceptance and fully exploit the remaining ISS lifetime.

2.1.1 Detector Structure

The overall dimensions of the AMS-02 detector are approximately $5 \times 4 \times 3 m^3$ 5 cubic meters, with a weight of around 7.5 tons. A schematic of the AMS-02 detector is shown in Fig. 2.2, The primary detection system of AMS-02 is the silicon Tracker, which consists of nine layers of silicon sensors. Six of these layers (L3 to L8) are positioned within the magnetic field generated by a permanent magnet. The Tracker plays a crucial role in measuring the momentum of charged particles by reconstructing their trajectories within the magnetic field. The charge sign of the particle is determined by combining the bending direction of its trajectory, as measured by the Tracker, with its direction of motion, as inferred from the Time of Flight (TOF) system.

The TOF system comprises two pairs of plastic scintillators located at both ends of the Tracker. It determines the velocity of the particle by measuring the time interval

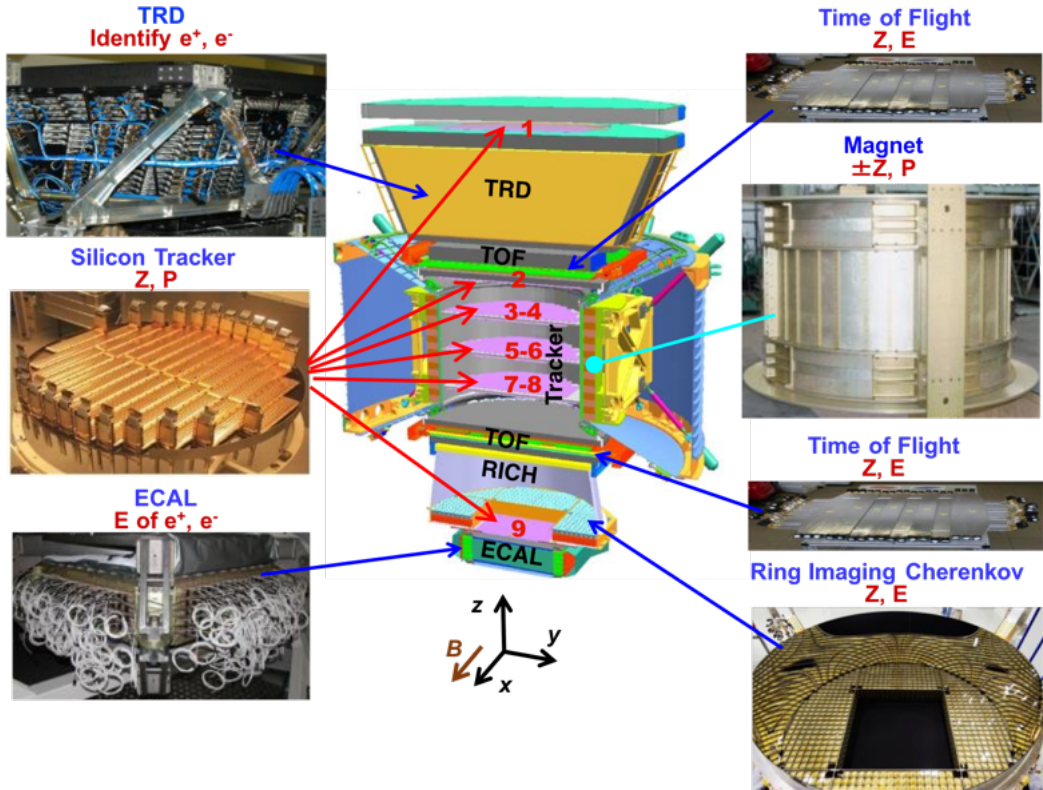


Figure (2.2) – The AMS detector showing the main elements and their functions [39].

between its passage through two TOF planes. Additionally, the TOF system serves as the primary trigger for the experiment.

The AMS-02 detector also includes three other sub-detectors to enable precise particle identification. The Ring Imaging Cherenkov (RICH) detector, positioned below the magnet, provides an independent measurement of the particle's velocity. The Transition Radiation Detector (TRD), located at the top of AMS-02, aids in distinguishing different particle species. Finally, the Electromagnetic Calorimeter (ECAL), placed at the bottom of the experiment, ensures accurate separation of leptons and hadrons through energy deposition measurements.

The Transition Radiation Detector:

The Transition Radiation Detector (TRD) [58] is the only gas detector on AMS-02. Positioned between the first layer of the silicon tracker and the upper layer of the Time-of-Flight (TOF) detector, as shown in Fig. 2.3, it features an overall design that

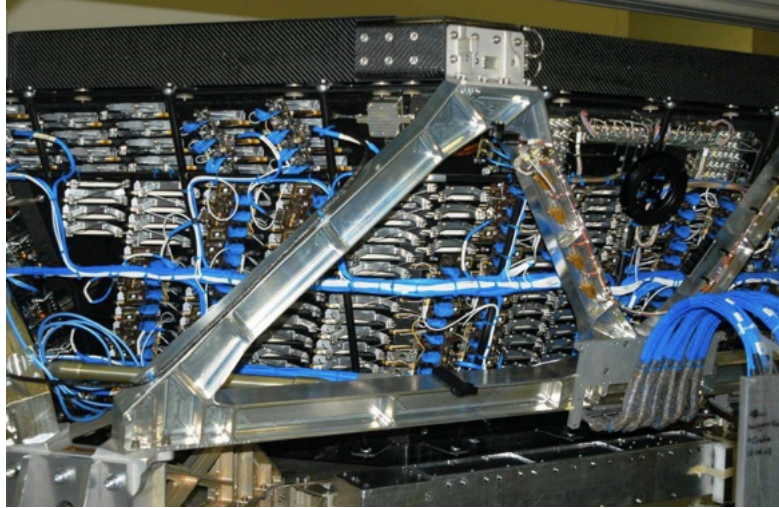


Figure (2.3) – The Transition Radiation Detector [39].

is wider at the top and narrower at the bottom, with a total height of approximately 0.8 meters. This tapered design effectively enhances its acceptance of cosmic rays. The TRD comprises 328 modules, each consisting of 16 straw tubes arranged in a flat row, with lengths ranging from 0.8 to 20 meters and a diameter of 6 mm. Additionally, each module includes a 20 mm-thick polyethylene fiber radiator. The tubes are filled with an Xe/CO₂ gas mixture, and a high-strength gold-plated tungsten wire with a diameter of approximately 30 micrometers is used as the anode, operating at a voltage of 1600 volts. These modules are stacked into 20 layers, with 12 layers arranged along the Y-direction and 8 layers along the X-direction.

The primary function of the TRD detector is to distinguish between electron/antiproton and positron/proton signals. As shown in Fig. 2.4, when high-speed charged particles traverse two layers of dielectric materials with different permittivities, they generate a certain amount of X-rays, known as transition radiation. The direction of these X-rays is nearly aligned with the direction of motion of the charged particles, and the probability of X-ray generation increases with the increase in the particle's Lorentz factor $\gamma = E/M$. For relativistic particles with different masses but the same kinetic energy, the smaller mass particle is more likely to exhibit the transition radiation effect. For particles that do not produce transition radiation, the straw tubes can only detect the ionization signal of the particles. For particles producing transition radiation, the detected signal in the straw tubes is a superposition of the ionization signal of the particles and the transition radiation signal. Therefore, using the Likelihood method and

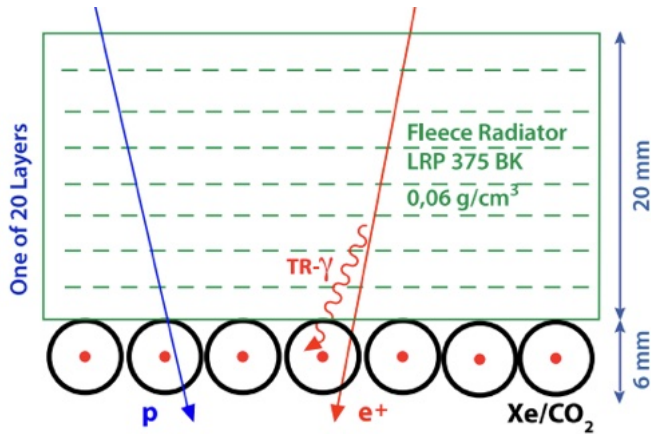


Figure (2.4) – Schematic of the detection of ionization losses from charged particles [39].

comparing the deposited energy, one can effectively distinguish electron/antiproton or positron/proton signals.

The TRD detector can also be used to measure the charge information of charged particles. During the ionization process of charged particles, electrons in the medium have a probability of acquiring high energy, forming delta electrons. Delta electrons can drift a few millimeters to a few centimeters near the particle trajectory, exciting adjacent straw tubes. The number of delta electrons generated by high-energy particles increases with their charge. Therefore, by calculating the number of delta electrons near the entry point, the charge of the incident particle can be determined.

The Time of Flight Counters:

The Time-of-Flight (TOF) [59] is composed of four layers of plastic scintillator (shown in Fig. 2.5), with two layers installed above the magnetic field, referred to as Upper TOF, and the other two layers installed below the magnetic field, referred to as Lower TOF. The vertical distance between Upper TOF and Lower TOF is 120 cm. Each layer consists of 8-10 elongated plastic scintillator bars, with a 5mm overlap between adjacent bars to ensure no signal loss. Two photomultiplier tubes (PMTs) are installed at each end of each plastic scintillator bar. To enhance photon collection efficiency, the outer surface of the scintillator bars is wrapped in a highly reflective aluminum film.

By comparing the timing of signals appearing in the upper and lower layers of TOF, the velocity of particles can be calculated, and it can be determined whether particles are incident from top to bottom or from bottom to top. The time resolution is measured

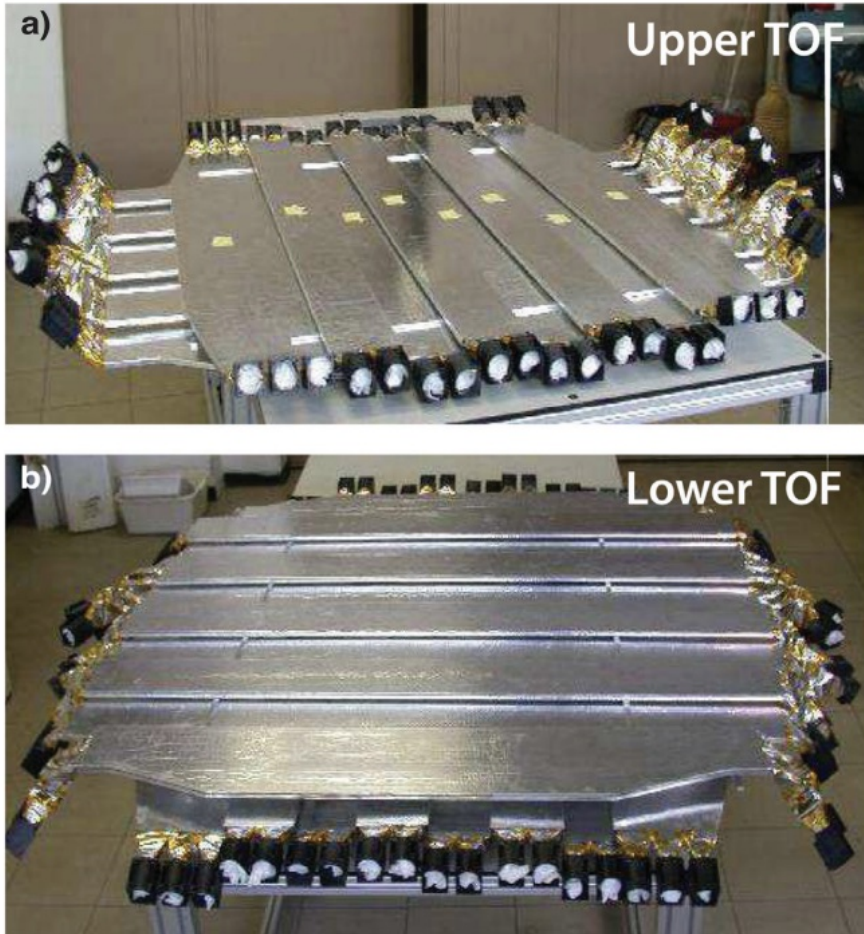


Figure (2.5) – (a) The upper TOF counters. (b) The lower TOF counters [39].

to be approximately 180 ps for $Z = 1$ particles and below 100 ps for particles with $Z \geq 2$ (reaching ~ 48 ps for $Z = 6$), which is enough to discriminate down-going particles from up-going ones at the level of 1 out of 10^9 . The resulting resolution on the particle velocity measurement is, below few GV, of the order of 4% for protons and 1% for ions [60]. As the TOF system delivers a rapid and reliable measurement of the energy loss of charged particles, it serves as the primary trigger for the experiment.

TOF system is also capable of measuring particle charges up to $Z = 40$. By combining measurements from both the upper and lower TOF layers, the accuracy of charge determination is further enhanced. Fig. 2.6 presents the charge distribution measured by the TOF, ranging from protons ($Z = 1$) to zinc ($Z = 30$). For individual TOF counters, the charge resolution is approximately 0.16 charge units (c.u.) for carbon ($Z = 6$) and around 0.4 c.u. for iron ($Z = 26$).

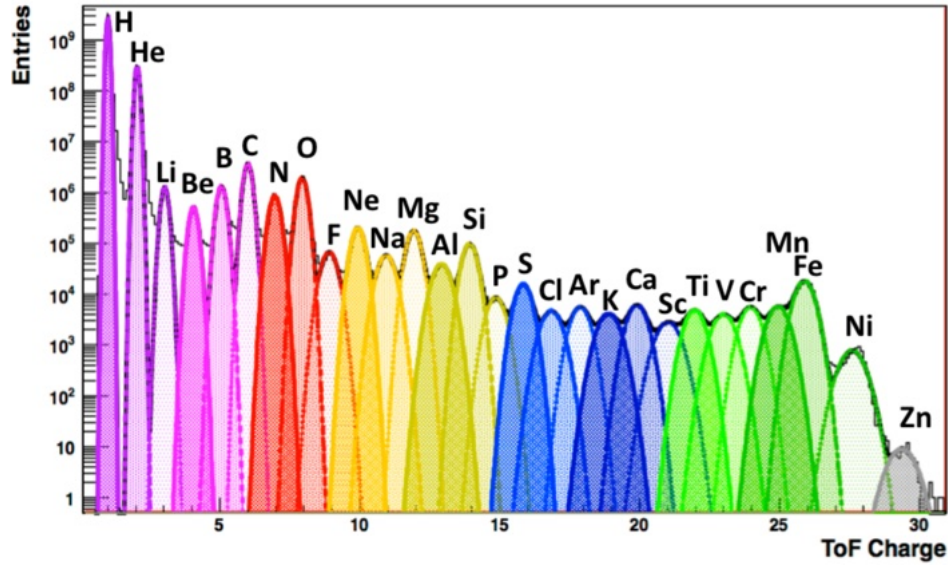


Figure (2.6) – The charge distribution from proton ($Z = 1$) to zinc ($Z = 30$) measured by the TOF [60].

The Ring Imaging Cherenkov Detector :

The RICH [61] detector is located between the Lower ToF and the 9th layer of the track detector, with a height of 47 cm. As shown in Fig. 2.7, Its upper surface has a diameter of 120 cm, and the lower surface has a diameter of 124 cm. the upper layer consists of two different radiators. The central square of the upper layer measures 34×34 cm 2 and is equipped with 16 pieces of sodium fluoride (NaF) crystals, each with a thickness of 0.5 cm and a refractive index of 1.33. These crystals cover approximately 10% of the overall acceptance of the RICH. Surrounding the central region, there are 92 pieces of 2.5 cm thick aerogel radiators with a refractive index of 1.05. The central area of the lower layer is left empty in a square shape with dimensions of 65×65 cm 2 to avoid obstructing the underlying ECAL detector. Around this central square region, there is an array of photomultiplier tubes (PMTs) used to detect the Cherenkov light generated by the radiators in the upper layer. This PMT array consists of 680 photomultiplier tubes. To enhance the collection range of Cherenkov light, a highly reflective aluminum mirror is placed on the side surface of the RICH. When Cherenkov light exceeds the range of the PMT array, the mirror reflects it back into the acceptance area.

The RICH measures the velocity and charge of passing particles. Both are calculated from the geometrical shapes, circles or rings, generated by the Cherenkov effect. The opening angle θ of the cone of photons generated in the radiator yields a measurement

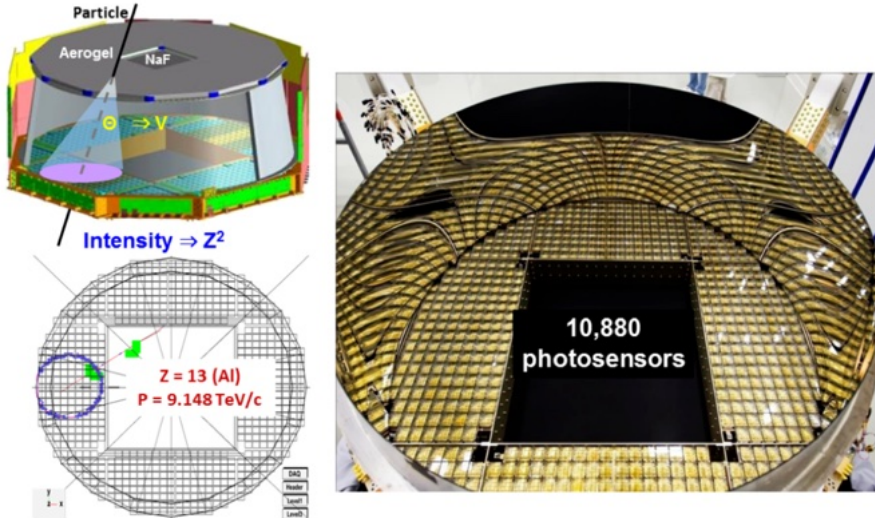


Figure (2.7) – The RICH detector and an event display with $Z = 13$ and $P = 9.148 \text{ TeV}/c$ [62].

of the velocity $\beta = v/c$ and the number of photons is proportional to Z^2 . The RICH provides a β measurement with a resolution $\sigma_\beta/\beta \sim 0.1\%$, for unitary charge particles, and $\sigma_\beta/\beta \sim 0.01\%$ for ions [63].

The Electromagnetic Calorimeter :

The Electromagnetic Calorimeter (ECAL) [64] is located at the bottom of AMS-02 and serves primarily to perform three-dimensional sampling of electromagnetic showers, precisely measuring the energy and direction of high-energy electrons and photons. As depicted in Figure 2.8, ECAL is constructed using 9 Super Layers, each consisting of lead plates and fiber interspaces stacked together. The front acceptance area is $648 \times 648 \text{ mm}^2$ square millimeters, with a total thickness of 166.5 mm. Each Super Layer has a thickness of 18.5 mm, composed of 11 lead layers and 10 fiber interspaces. The lead layers are 1 mm thick, and the fiber diameter is 1 mm, bonded together with epoxy resin to form a unified structure. In each adjacent pair of Super Layers, the fiber orientations are perpendicular to each other, with five Super Layers in the X direction and four in the Y direction. The signals from ECAL are processed by Photomultiplier Tubes (PMTs) installed at the ends of the fibers, each PMT having four anodes with an area of $9 \times 9 \text{ mm}^2$, corresponding to 35 fibers. At each end of the Super Layer, 36 PMTs are connected.

The ECAL achieves an energy resolution for high-energy electrons within the range of 1.5 – 3% and an angular resolution for their incident angles of approximately 1 degree.

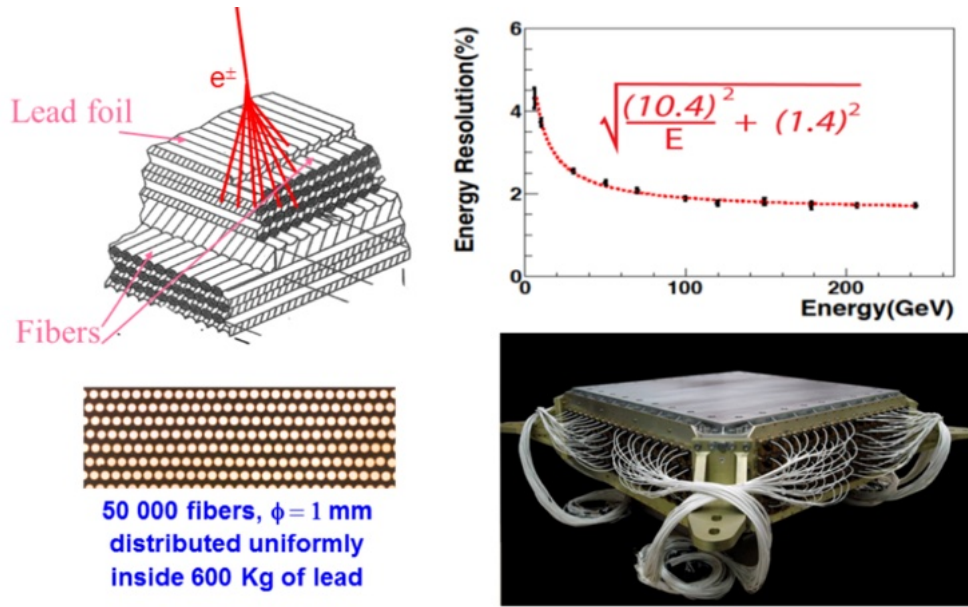


Figure (2.8) – The construction and energy resolution of the ECAL [65].

While ECAL has 17 radiation lengths for electromagnetic interactions, it only has one nuclear interaction length. Consequently, the probability of a hadronic interaction for strongly interacting particles in ECAL is only about 60%. For protons and electrons with the same incident energy, protons deposit significantly less energy than electrons. By leveraging the distinct characteristics of electromagnetic and hadronic showers, coupled with particle information obtained from the tracking detector, ECAL effectively distinguishes electrons/positrons from anti-electrons/protons.

The ECAL also functions as an independent photon trigger, achieving an efficiency exceeding 99% for energies above 5 GeV. This capability enables the detection of photons within the AMS02 field of view that have not undergone interactions prior to reaching the calorimeter. Due to the radiation length (X_0) present in front of the calorimeter, over 60% of photons entering the detector from above reach the calorimeter directly without interaction. Conversely, photons that interact with the material before reaching the ECAL can be identified through the detection of the resulting e^\pm pair in the Silicon Tracker.

The Anti-Coincidence Counter :

The Anti-Coincidence Counter (ACC) [66] is designed as a cylindrical structure with a height of 1.1 meters and a diameter of 0.8 meters, surrounding the inner tracking detector. Its structure is illustrated in Figure 2.9. The ACC is composed of 16 blocks of 0.8 cm thick plastic scintillators, each containing 74 optical fibers embedded within. These fibers extend to the ends of the scintillator blocks and are connected to 8 photomultiplier tubes (PMTs) at both upper and lower ends of the magnetic field for signal readout. The upper PMTs read the signals from adjacent scintillator blocks, while the lower PMTs read signals from scintillator blocks separated by one block.

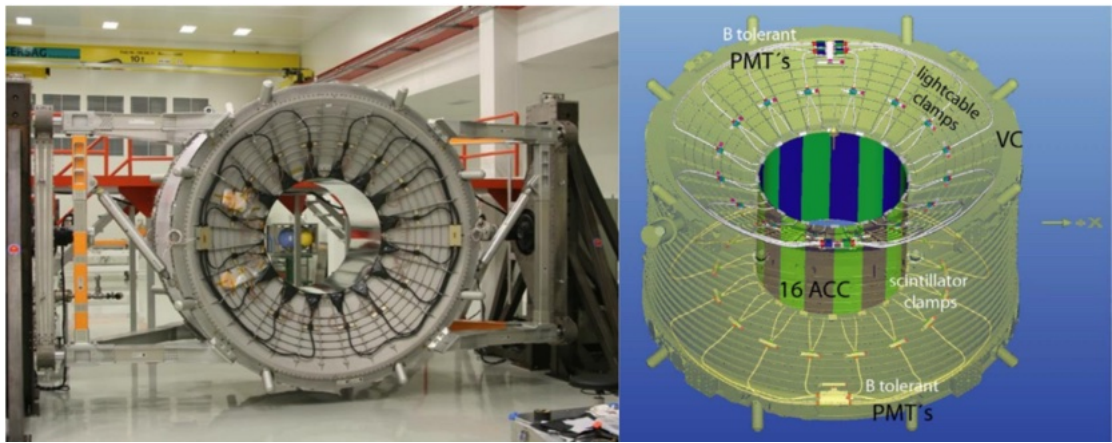


Figure (2.9) – The Veto (ACC) system [67].

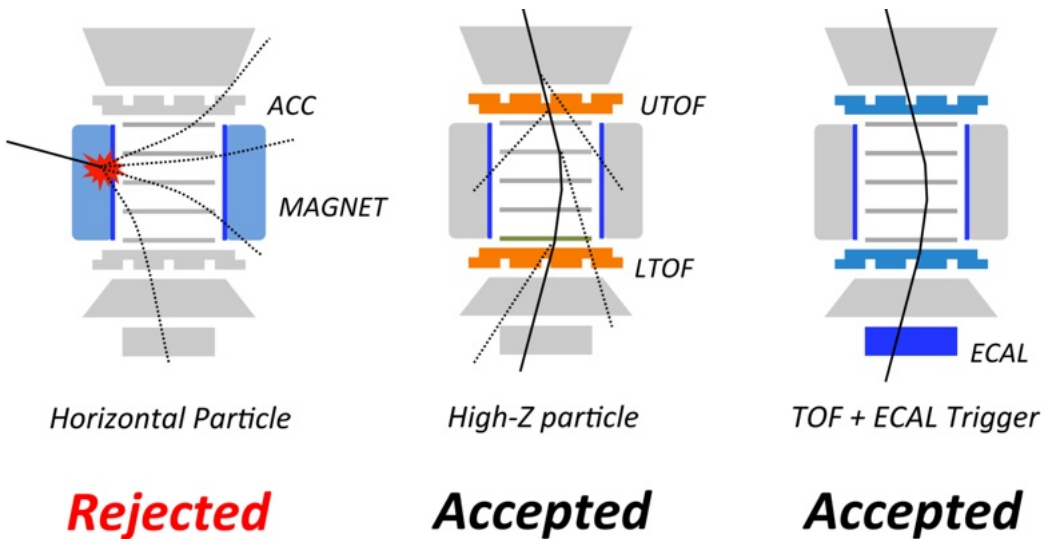


Figure (2.10) – Illustration of the ACC's purpose in rejecting spurious events in the AMS trigger [68].

The ACC exhibits high sensitivity and effectively eliminates abnormal events, as illustrated in Fig. 2.10. For instance, the direction of incident cosmic rays is generally uniform, but the design of AMS-02 allows it to selectively measure particles passing through a limited solid angle range around the Z-axis direction. The ACC efficiently excludes particles coming from other directions, such as the horizontal direction.

The magnetic spectrometer

The magnetic field (shown in Fig. 2.11) of AMS-02 is generated by 64 sets of rubidium-iron-boron ($Nd_2Fe_{14}B$) magnets, forming a cylindrical structure with a diameter of 1.1 meters and a total weight of 1200 kilograms [69]. This magnet can produce a uniform magnetic field of 1400 Gauss in the central region, with a total bending power of 0.15 Tm^2 . When charged particles traverse the magnetic field, their trajectories are influenced by the Lorentz force, leading to deflection. By measuring the direction of deflection, as well as the curvature of the particle's deflection, combined with charge information, details such as the particle's momentum can be determined.

The tracker (shown in Fig. 2.12) of AMS-02 [70] consists of nine layers of silicon microstrip detectors, with each layer composed of 16-26 rectangular modules to accommodate various installation positions. In total, 192 modules are used, arranged in a top-to-bottom sequence. The nine layers are positioned on aluminum planes covered with high-strength carbon fiber. Layers 1, 2, and 9 have a single-layer structure, while

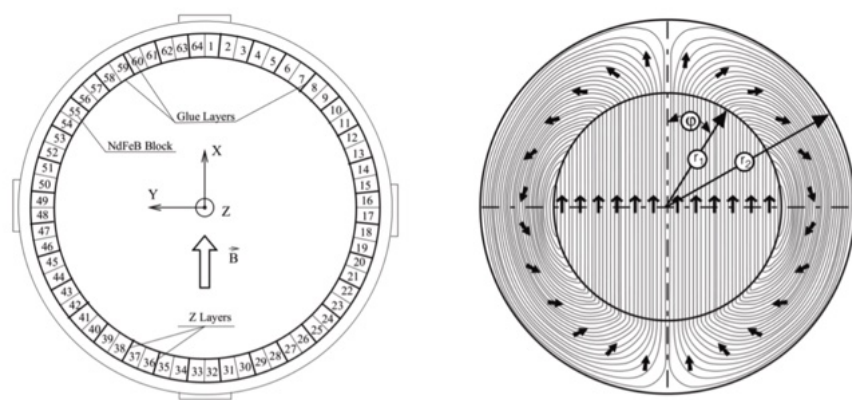


Figure (2.11) – Left: A cross-sectional view from above of the AMS magnet. Right: The magnetization vector flow is confined in the magnet volume with a negligible leak, making the magnetic field stable. [68].

layers 3-8 are placed on three-layer support surfaces, forming an anti-face structure. The first layer is positioned above the Transition Radiation Detector (TRD), layers 2-8 are located inside the magnetic field, and layer 9 is placed between the Ring Imaging Cherenkov detector (RICH) and the Electromagnetic Calorimeter (ECAL).

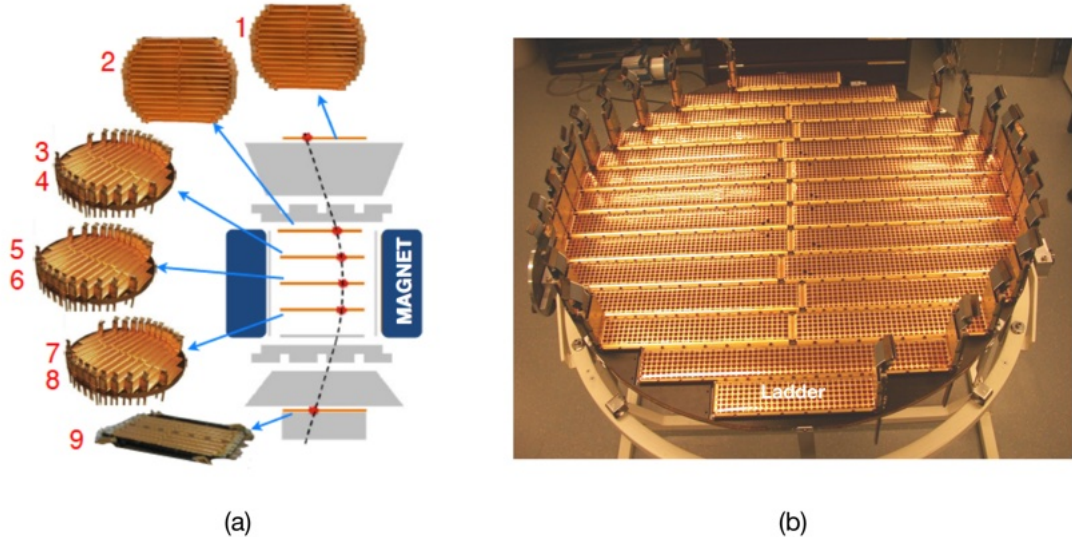


Figure (2.12) – Left: (a) Layout of the nine Silicon Tracker layers. (b) Real view of a silicon tracker inner plane. [71].

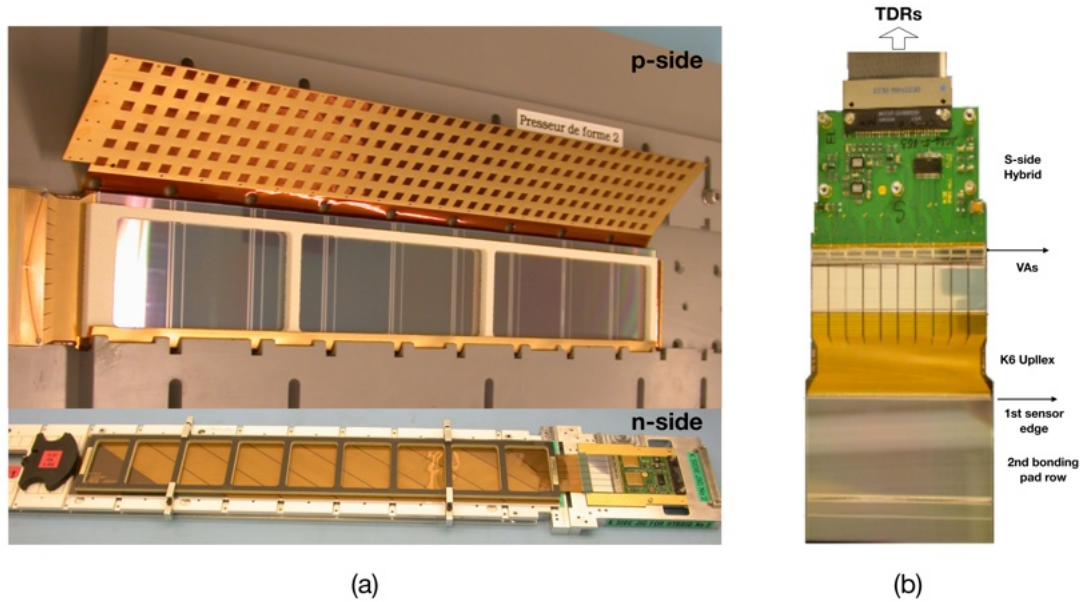


Figure (2.13) – (a) A real view of a ladder on the p-side and n-side before covered by the electromagnetic shielding foil. (b) Tracker Front-end Electronics of a ladder. [71].

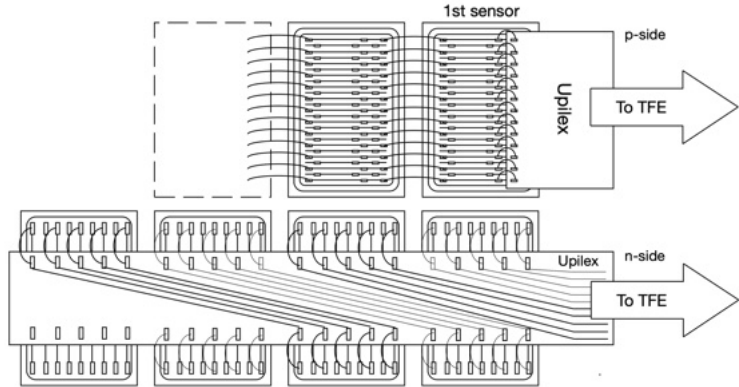


Figure (2.14) – Schematic view of one ladder on p-side and n-side. [71].

The fundamental component of the tracker is a double-sided silicon sensor with dimensions of approximately $72.045 \times 41.360 \times 0.300 \text{ mm}^3$. Each sensor features p+ strips on one side, arranged with an implantation pitch of $27.5 \mu\text{m}$ and a readout pitch of $110 \mu\text{m}$, while n+ strips are placed orthogonally, with an implantation pitch of $104 \mu\text{m}$ and a readout pitch of $208 \mu\text{m}$. The finer-pitch p-side strips are responsible for measuring the bending (y) coordinate, whereas the orthogonal n-side strips determine the x coordinate.

These silicon sensors are integrated into basic structural units known as *ladders* (illustrated in Fig. 2.13). Each ladder consists of 9 to 15 sensors mounted within a carbon-fiber frame, following the configuration shown in Fig. 2.14. The entire system comprises 192 ladders, covering an active area of approximately 6.4 m^2 . The p-side strips are aligned along the ladder's longitudinal direction, while the n-side strips are oriented perpendicularly. This arrangement necessitates distinct signal-routing strategies for each side. On the p-side, strips from adjacent sensors are directly interconnected via metallic bonds in a daisy-chain fashion. Conversely, on the n-side, signals from alternating sensors are merged and routed to the same readout channel.

The primary role of silicon detectors is to track the trajectories of charged particles and determine their charge. Figure 2.15 presents the spatial resolution on layers 3 and 5 for carbon nuclei with rigidity $R > 50 \text{ GV}$, comparing results obtained using the η algorithm [72] (left) and the non-linear η algorithm [72] (right). Figure 2.16 illustrates the tracker charge distribution based on combined p-side and n-side measurements [73], along with the charge estimator resolution (in charge units) for nuclei up to silicon.

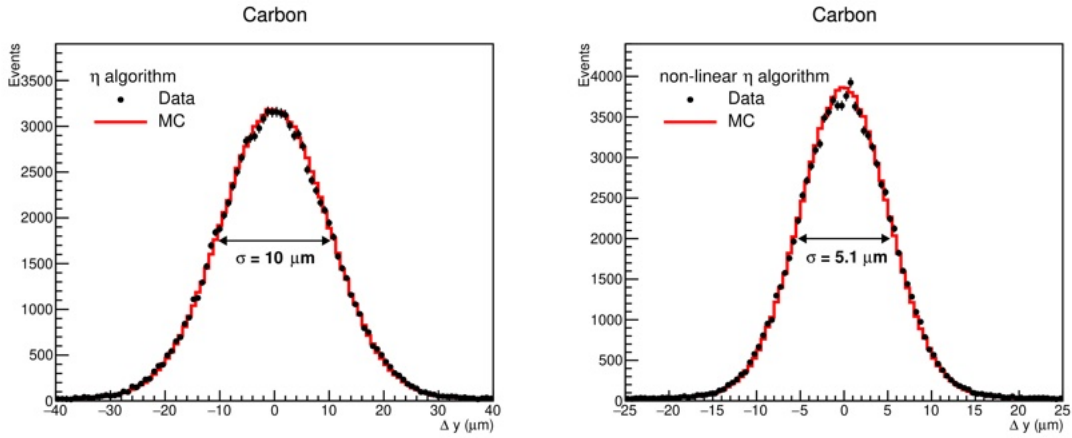


Figure (2.15) – Spatial resolution on layers 3 and 5 for Carbon nuclei with rigidity $R > 50$ GV obtained with the η algorithm (Left) and with the non-linear η algorithm. [72].

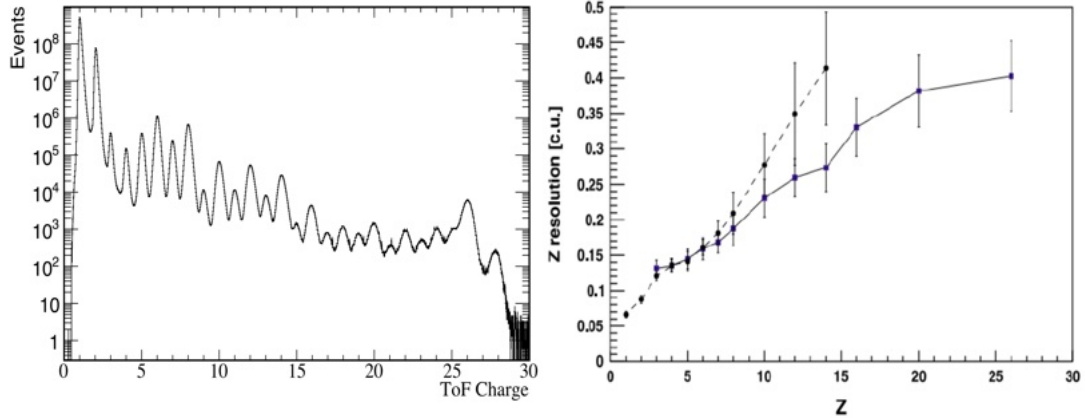


Figure (2.16) – Left: ToF charge estimator for nuclei events up to Ni. Right: anode (dots, dashed line) and dynode (squares, solid line) charge resolution in charge units (c.u.) as a function of Z [73].

2.1.2 AMS-02 Layer 0 upgrade

AMS-02 has a unique capability to distinguish between matter and antimatter, a feature that no other experiment can currently match, nor is it expected that similar data will be obtainable in the near future. For this reason, options for upgrading AMS [74] are being considered, with the aim of maximizing the use of the remaining data up until 2030. The proposed upgrade involves adding new tracking layer(L0) on top of the existing tracking layer 1, which would increase the acceptance of AMS02 by a factor of 3, as shown in Figure 2.17.

Adding L0 to AMS 02 can bring many benefits, for example, extending the energy

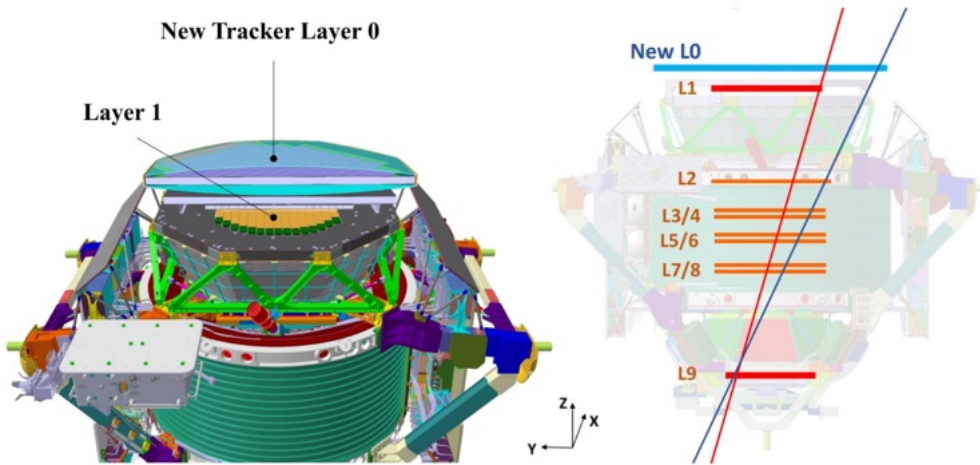


Figure (2.17) – The schematic diagram of the L0 installation on top of AMS02.

range of the positron flux measurement to 2 TeV from the current 1.4 TeV and reducing the uncertainties by a factor of two (see Figure 2.18). This is particularly important at high energies, as it will ensure that the measured high-energy positron spectrum indeed drops off quickly in the 1-2 TeV region, where the positrons come only from cosmic ray collisions as predicted by dark matter models (see Figure 2.19).

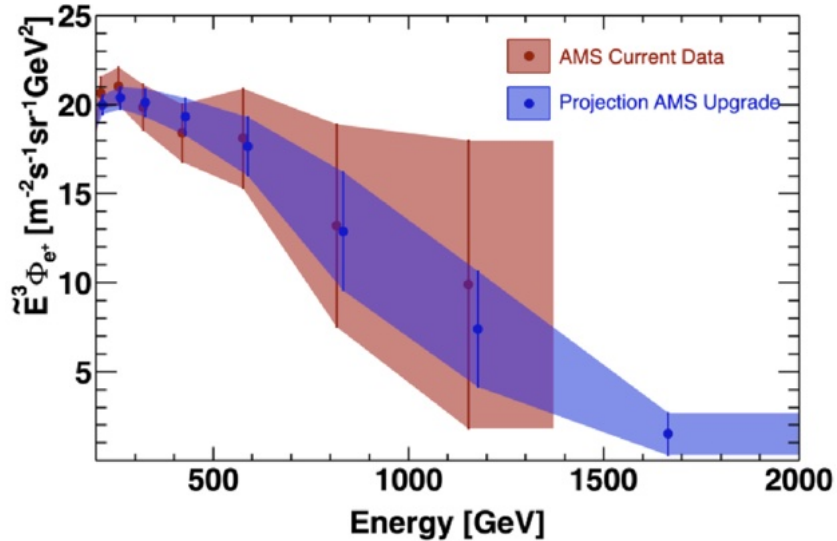


Figure (2.18) – Positron spectrum at highest energies for the current data (blue shading) and with the upgrade through 2030 (gold shading) [74].

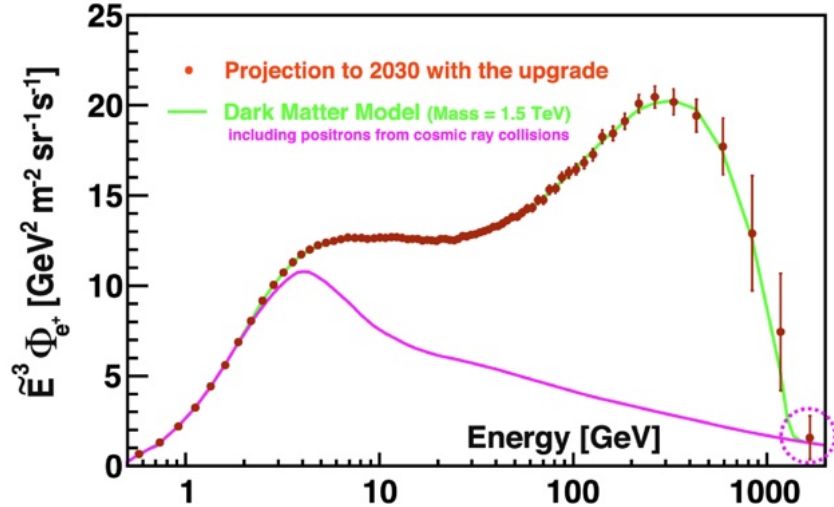


Figure (2.19) – Positron spectrum with the upgrade through 2030 (cyan points) together with a dark matter prediction (magenta curve) which includes cosmic ray collisions (green curve) [74].

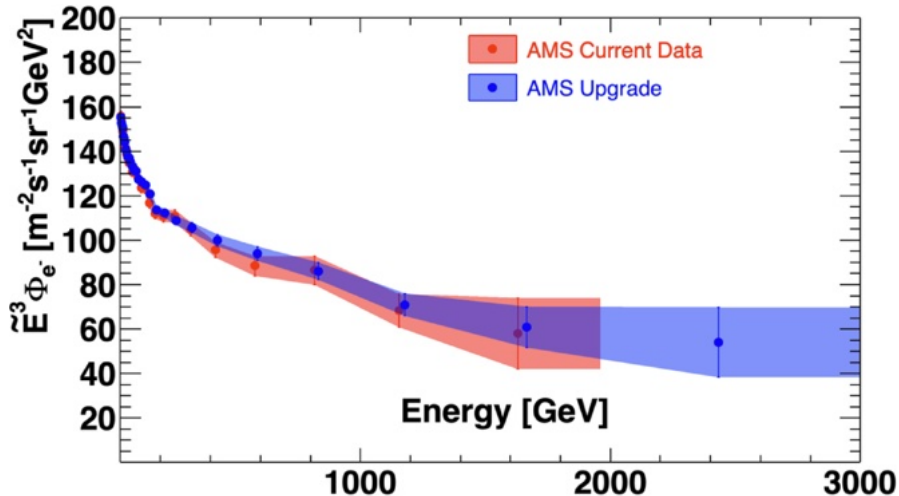


Figure (2.20) – Electron spectrum at high energies for current data (blue shading) and with the upgrade (gold shading) [74].

This upgrade will also extend the energy range of the electron flux measurement to 3 TeV from the current 2 TeV and reduce the error by a factor of about two (see Figure 2.20). This will provide definitive proof of the existence of a positron source term in both the positron and electron spectra and, consequently, the existence of new physics. As shown in Figure 2.21, current data (left) show that the electron spectrum can be described by the sum of two power-law components and a charge-symmetric positron

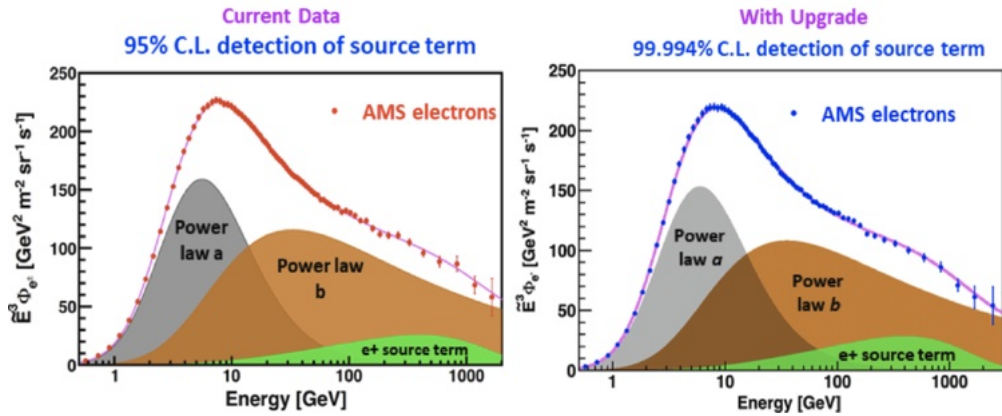


Figure (2.21) – Origin of high energy electrons [74].

source term. At present, the significance of this positron source term in the electron spectrum is 2σ . With the upgrade (right), we will reach 4σ significance.

L0 consists of two planes of silicon micro-strip sensors, as shown in Figure 2.22, both with an active area of approximately 4m^2 . The L0-U plane is on top of L0, while the L0-Y plane is on the bottom. The L0-Y plane measures the AMS bending coordinate, and the L0-U plane is mounted with strips oriented at 45 degrees to those in L0-Y. The L0-U plane measures both the bending and non-bending coordinates. Each plane is composed of 36 mechanical-electrical units called “ladders”. There are three lengths of ladders, containing 8, 10, or 12 silicon sensors, respectively. The ladders are surrounded by readout electronic boards.

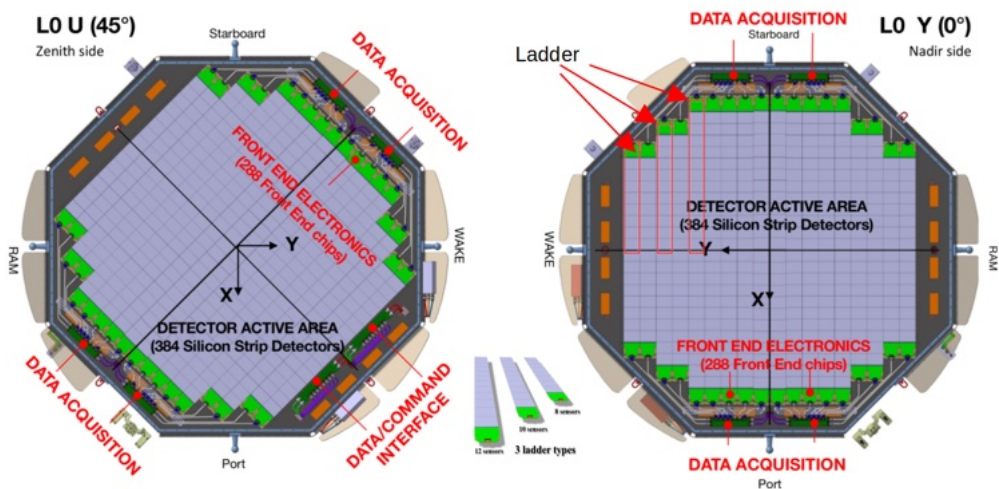


Figure (2.22) – The Schematic diagram of L0 structure [74].

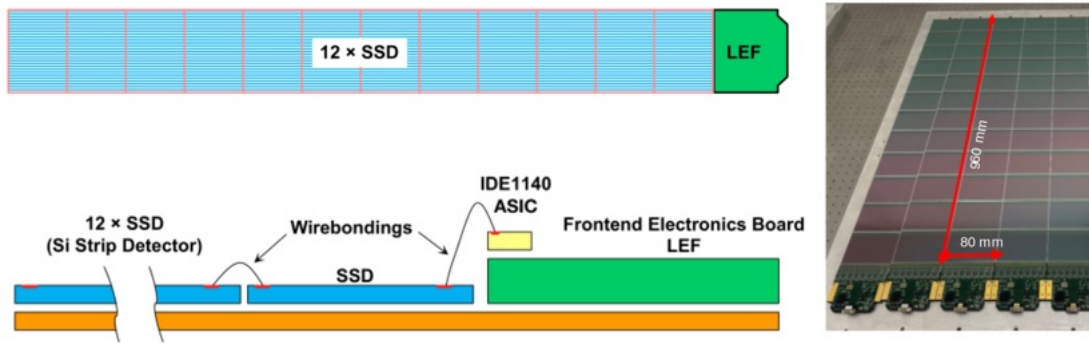


Figure (2.23) – The schematic diagram of a ladder with 12 sensors.

For example, Figure 2.23 shows the longest L0 ladder, which is composed of 12 sensors, a front-end electronics board, and a long flexible printed circuit board for mounting. Its total sensitive area is $960 \times 80 \text{ mm}^2$.

As illustrated in Figures 2.24 and 2.25, the ladders are installed on both sides of a carbon-fiber aluminum honeycomb structural plane, along with the associated electronics and heaters. These components are enclosed by thin carbon-fiber cupolas, which are securely attached to the structural plane. The cupolas serve multiple functions: they ensure light tightness, provide electromagnetic shielding for the sensors and electronics, and offer protection against both space debris and potential damage during ground handling. The heat generated by the electronics and heaters within Layer-0 is efficiently transferred via copper foil to radiators positioned around the structural plane's rim. Figure 2.26 shows the actual image of the fully assembled L0.

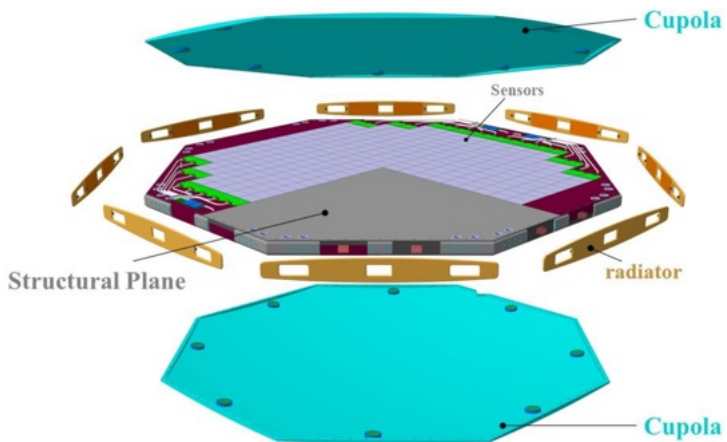


Figure (2.24) – Details of the Layer0 main mechanics [74].

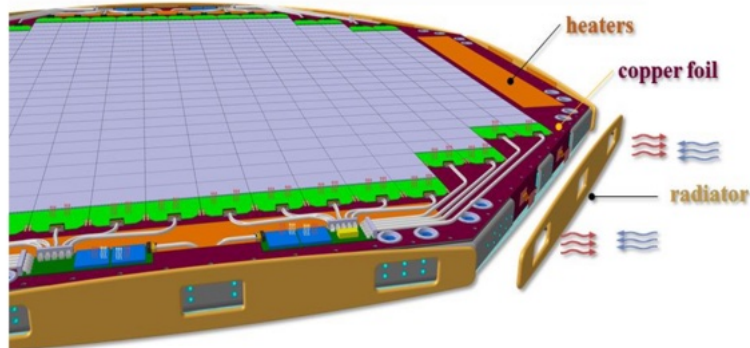


Figure (2.25) – Details of the Layer0 thermal systems [74].



Figure (2.26) – The actual image of the fully assembled L0.

Chapter 4 of this thesis will cover the detailed construction of the ladder and the analysis of data from its beam tests.

2.2 The HERD Experiment

The High Energy cosmic-Radiation Detection (HERD) facility [38] is one of the leading projects among future space-borne instruments to be installed on-board the Chinese Space Station (CSS), around 2027, (fig.2.27) following a Low-Earth Orbit (LEO) at an altitude of approximately 400 km and an inclination angle of 42° with an expected duration of approximately 10 years.

HERD is designed to perform calorimetric measurements of different CR species at energies well above the maximum reach of AMS-02 or DAMPE [76] experiments, to search for signatures of the annihilation/decay products of dark matter particles in the energy spectra and anisotropy of high-energy electrons from 10 GeV to 100 TeV, as well as in the gamma-ray spectrum from 500 MeV to 100 TeV. Precise measurement of the energy spectra and composition of nuclei from 30 GeV up to PeV, is in the physics program of HEARD, aimed to determine the mechanism behind the “knee” structure in the cosmic rays.

2.2.1 Detector Structure

In order to achieve its objectives while satisfying the size/weight requirements for launch, HERD has a nearly isotropic design based on a 3-D cubic imaging calorimeter (CALO) surrounded by scintillating fiber trackers (FITs) on the top and on the four lateral sides. The CALO and FIT are then covered by the Silicon Charge Detector (SCD) and



Figure (2.27) – HERD onboard the China's Space Station (CSS) [75].

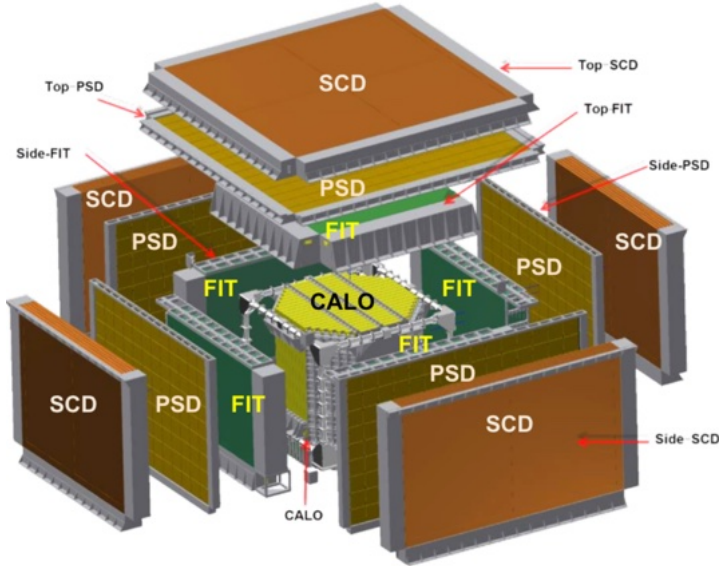


Figure (2.28) – Exploded view of the HERD detector [77].

the plastic scintillator detector (PSD) from the outside. A Transition Radiation Detector (TRD) is located on the lateral side (Fig. 2.28). SCD is used for the accurate measurement of the particle's absolute charge magnitude $| Z |$. PSD is used for triggering gamma and charge measurement. FIT is mainly for particle tracking and charge measurement. CALO is for energy reconstruction and e/p discrimination. TRD is for the calibration of TeV nuclei.

The CALO:

CALO [78] is the primary detector of the HERD instrument: it is a homogeneous, isotropic, 3D segmented calorimeter that can detect particles coming from every surface. CALO is comprised of 7500 LYSO crystal cubes, each with a side length of 3 cm, and its overall shape resembles an octagonal prism (fig. 2.29). For vertical particles, the total depth of CALO is about 55 radiation lengths and 3 interaction lengths.

The FIT:

The design objective of the HERD Scintillating Fiber Tracker (FIT) [79] is to reconstruct the trajectories and determine the absolute charge value $| Z |$ of charged cosmic rays. In the current design, FIT is structured into 5 tracking sectors (Fig.2.30), each comprising

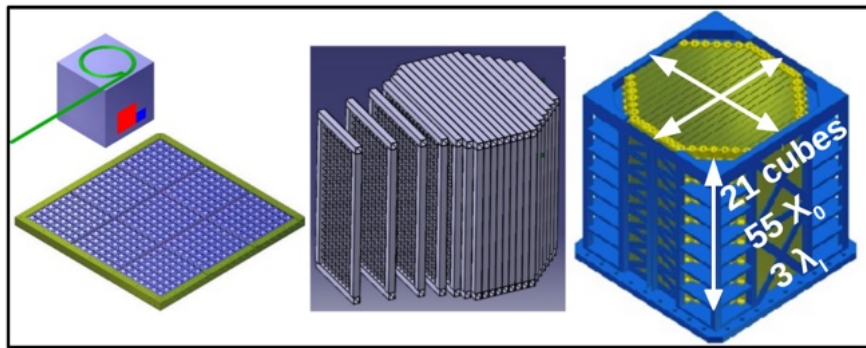


Figure (2.29) – Basic drawing of the different CALO components [78].

7 tracking planes. This configuration allows for 7 independent measurements of the position of a traversing charged particle. Each tracking plane consists of two layers of FIT modules that measure the two orthogonal spatial coordinates. The tracking planes in the top sector consist of 10 FIT modules on both the x and y layers, while the tracking planes in the side sectors are formed by 6 FIT modules on the x layers and 10 FIT modules on the y layers. Each module comprises a scintillating fiber mat and three silicon photomultiplier (SiPM) arrays to capture the scintillation light generated when particles hit the mat.

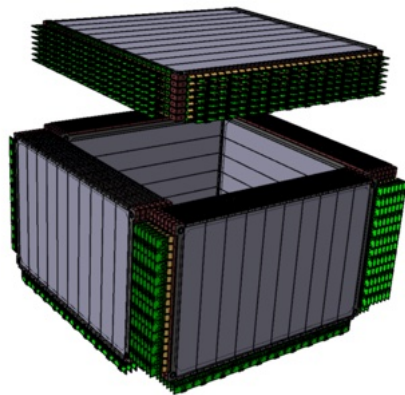


Figure (2.30) – Sketch of the 5-side FIT detector [80].

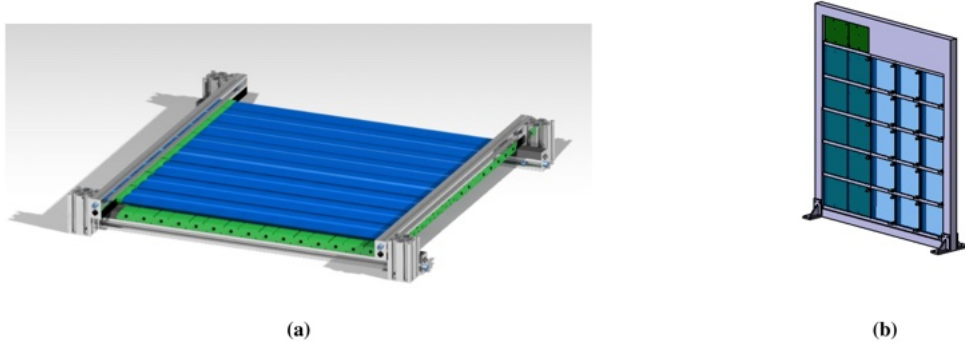


Figure (2.31) – Preliminary designs of PSD (a) bar and (b) tile prototypes [80].

The PSD:

The Plastic Scintillator Detector (PSD) [81] of HERD measures the charge of incoming cosmic-ray nuclei within the range $Z = 1$ to ~ 26 . In the PSD, organic scintillators are read out using silicon photomultipliers (SiPMs) instead of traditional photomultiplier tubes (PMTs). This choice is based on the characteristics of SiPMs, including fast light signal detection, sensitivity to low light yields, low power consumption, and robustness. The primary design requirements for the PSD include high detection efficiency, a broad dynamic range, and good energy resolution. Currently, two design layouts are under investigation: one based on long scintillator bars and the other on square (or rectangular) tiles. Each configuration has its advantages and disadvantages, primarily related to the optimal number of readout channels versus back-splash (or back-scattering) effects. Continuous testing and optimization efforts are underway for both configurations, aiming to determine the best scintillator type and size, SiPM model and quantity for instrumentation, and overall verification of the PSD configuration, structural robustness, and space adaptability.

The SCD:

The SCD (Silicon Charge Detector) [82] is the first detector encountered by a particle traversing HERD, positioned above the PSD (Plastic Scintillator Detector), and is designed to provide charge measurements in HERD. The choice of placing the SCD at the top of the instrument aims to ensure that particles do not interact with other detectors before entering the SCD. This arrangement facilitates reliable charge measurements and minimizes the fragmentation of cosmic-ray nuclei, reducing systematic errors in HERD.

flux measurements. Additionally, the SCD is capable of 3D tracking and will be used in conjunction with FIT (Fiber Tracker) for HERD particle trajectory reconstruction. The additional features of the SCD enhance redundancy between different sub-detectors and allow for cross-calibrations.

In the current design, the SCD consists of 5 thin detector units. One unit is square-shaped with dimensions of $1.6 \times 1.6 \text{ m}^2$, placed on the top of the instrument, while the other four units have dimensions of $1.4 \times 0.9 \text{ m}^2$ and are positioned on the other four sides. Each detection unit contains 8 layers of $300 \mu\text{m}$ microstrip silicon detectors mounted with alternating orthogonal strip directions. Each XY pair is composed of a supporting structure made of a woven carbon fiber frame with high modulus unidirectional carbon fiber skins and an aluminum honeycomb core, as shown in Figure 2.32.

Similar to AMS02, the SCD will also consist of “ladders”, where multiple silicon sensors are connected in a daisy chain and read out from one side by dedicated electronics. Each side unit will contain 1024 silicon wafers, while the top unit will have 2048 wafers, for a total of 6144 wafers. Using the designed $97.5 \times 97.5 \text{ mm}^2$ silicon sensors, the total silicon area will be $\sim 60 \text{ m}^2$. To reduce the number of readout channels while maintaining satisfactory performance in terms of spatial and charge resolution, the readout adopts the so-called floating strip method, where a certain number of implanted strips are not read out.

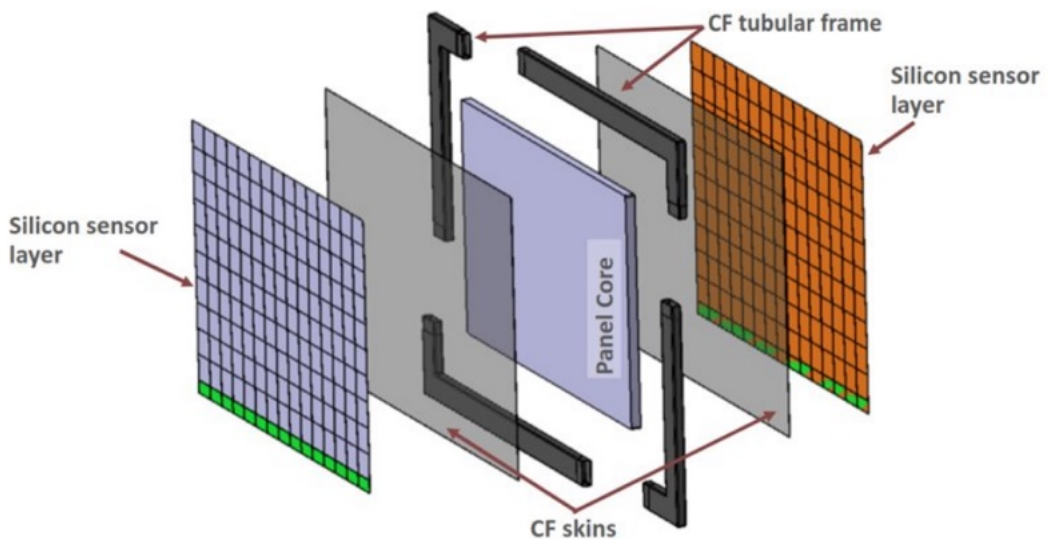


Figure (2.32) – Exploded view of one of the SCD layers [82].

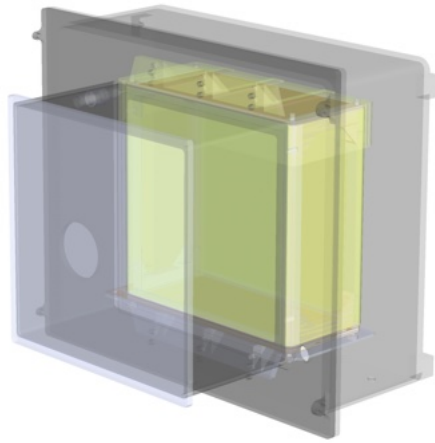


Figure (2.33) – 3D view of new side-on TRD prototype [83].

Chapter 4 of this paper presents the beam test results of a single SCD sensor and compares its performance with that of the AMS L0 sensor.

The TRD:

The Transition Radiation Detector (TRD) [83] will be employed to calibrate the energy measurement of incident particles within an energy range where transition radiation (TR) is generated but not saturated. The TR energy is directly proportional to the Lorentz factor γ of the incident charged particle. The emission of radiant photons occurs at $\gamma \sim 10^3$ and saturates at $\gamma \sim 10^4$. This corresponds to a proton energy range of about 1-10 TeV. Through the detection of X-rays generated by TR, the absolute energy of the incident charged particle in the TeV region can be determined by measuring the Lorentz factor. The newly designed side-on TRD prototype features a fully metal chamber that encloses the working gas. A 3D representation of the prototype can be seen in Figure 2.33, with its side view shown in Figure 2.34(a), where also the different TRD components are detailed: the structure of the standard radiator (b), and the THGEM working scheme (c, d) used for X-ray detection.

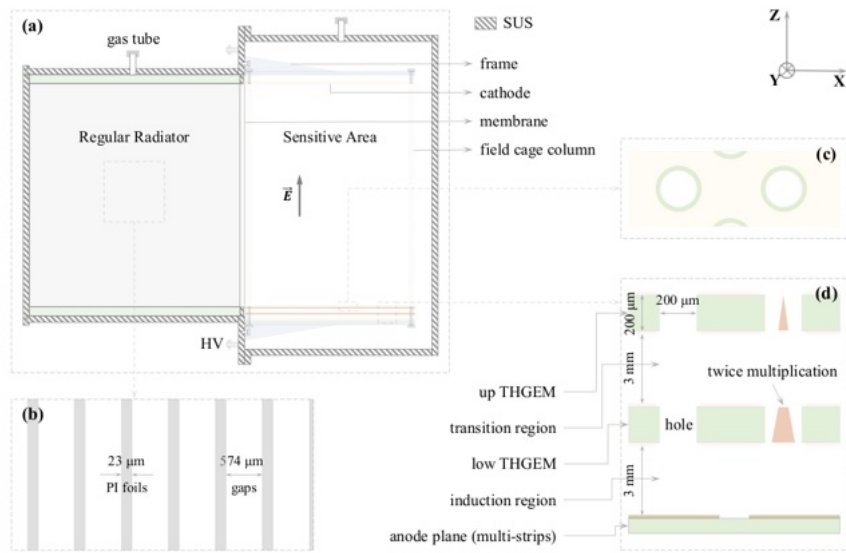


Figure (2.34) – (a) Profile of transition radiation detector; (b) structure of the regular radiator; (c) a front view of THGEM; (d) THGEM parameters and the multiplication of electron in the THGEM hole. [83].

CHAPTER 3

Silicon Microstrip Detectors

Silicon Microstrip Detectors are by now a well established technology used to perform simultaneous measurement of particles absolute charge, Z , and position with a resolution of few microns. Their light weight and relatively low operating voltages make their use particularly suitable in space experiments, and the current challenge is to cover wide areas, as for the L0 upgrade in AMS-02 or the HERD detector, while keeping a manageable number of readout channels. In this chapter we will briefly review their operating principle, starting from semiconductor properties and the p-n junction, then discussing different sensor designs, their integration in the *ladder* structure and readout electronics. Finally we will introduce the signal analysis to reconstruct position and charge.

3.1 The semiconductors

Energy band characteristics determine electrical conduction properties of different type of solids (cfr. Fig.3.1). The conductivity of a material is in fact the result of a directed motion of electrons in the presence of an external electric field. This involves energy exchange between electrons and the external electric field, causing electron transitions from one energy level to another. A material will be a conductor if its conduction band is partially filled with electrons, so that they can absorb energy from the external electric field and have a transition to unoccupied energy level, enabling the formation of current.

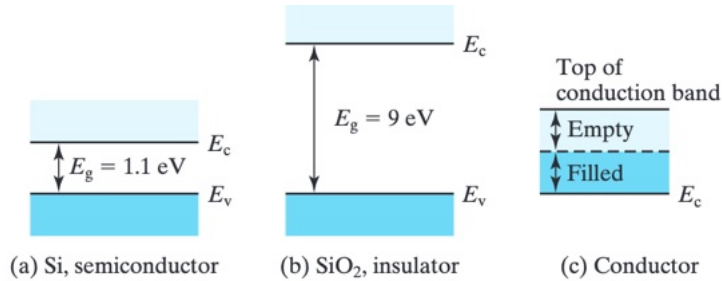


Figure (3.1) – Schematic representation of energy bands for semiconductors (a), insulators (b) and conductors (c)[84].

The conduction band is empty in insulators and the valence band is completely filled with electrons, with no way for them to make transitions within the band under the effect of an external field. Thermal energy may allow the transfer of an electron from the valence to the conduction band if it is close enough in energy. The basic difference between semiconductors and insulator is the energy gap value between valence and conduction bands, typically $< 1 \text{ eV}$ for semiconductors and 5 to 10 times larger for insulators. At zero thermodynamic temperature, insulators and semiconductors do not conduct electricity under the influence of an external electric field. However, when environmental conditions change, such as an increase in temperature or exposure to light, due to the narrow band gap of semiconductors, a small number of electrons from the valence band may be excited to the conduction band. Under the influence of an external electric field, these electrons will participate in conduction. Simultaneously, due to the reduction in the number of electrons in the valence band, leaving behind holes, the valence band also becomes partially filled. The electrons remaining in the valence band can still contribute to conduction under the influence of an external electric field.

3.1.1 Intrinsic semiconductors

Intrinsic semiconductor refers to a *pure* semiconductor, i.e. without any impurities or lattice defects. At thermal equilibrium, the probability distribution for different energy quantum states to be occupied by electrons is constant and derives from the Fermi-Dirac statistics, it can be described by the Fermi function $f(E)$:

$$f(E) = \frac{1}{1 + e^{\left(\frac{E-E_F}{k_0 T}\right)}} \quad (3.1)$$

where k_0 is the Boltzmann constant, T is the temperature, and E_F is referred to as the Fermi level. Figure 3.2 illustrates the relationship between the Fermi distribution func-

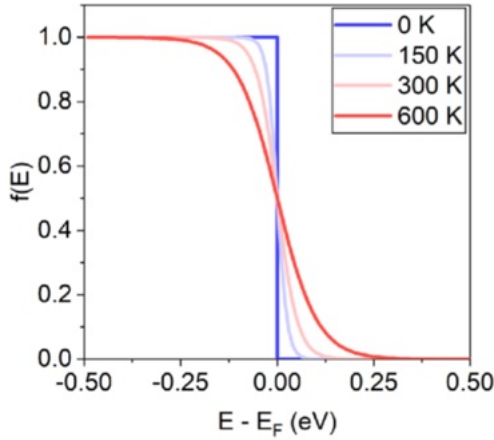


Figure (3.2) – Fermi-Dirac distribution function at different temperatures [85].

tion and temperature. From the graph, it is evident that when $T = 0K$, the probability of quantum states to be occupied with electrons at energies lower than E_F is 100%, while the probability of quantum states to be filled with electrons energies higher than E_F is zero, indicating absence of electrons in these states. Therefore, at absolute zero temperature, the Fermi level E_F can be considered as a boundary that separates energy states filled with electrons from empty ones. As temperature increases, there will be a finite probability for electrons to occupy energies states above E_F : the probability for energy states to be occupied with electrons at an energy below/above/equal the Fermi level will be $>/</= 50\%$ respectively. Since $f(E)$ defined in equation 3.1 represents the probability of a quantum state with energy E to be filled, $1 - f(E)$ will be the probability of a state to be NOT occupied. This defines the *hole* probability distribution:

$$1 - f(E) = \frac{1}{1 + e^{\left(\frac{E_F - E}{k_0 T}\right)}} \quad (3.2)$$

When $(E - E_F) \gg k_0 T$ in equation 3.1 and $(E_F - E) \gg k_0 T$ in equations 3.3, we get back to the Maxwell-Boltzmann distribution f_B for electrons and $1 - f_B$ for holes:

$$f_B(E) = e^{-\frac{E - E_F}{k_0 T}} = e^{\frac{E_F}{k_0 T}} e^{-\frac{E}{k_0 T}} \quad (3.3)$$

$$1 - f_B(E) = e^{-\frac{E_F - E}{k_0 T}} = e^{-\frac{E_F}{k_0 T}} e^{\frac{E}{k_0 T}} \quad (3.4)$$

In semiconductors, the most common scenario is where the Fermi level (E_F) lies within the band gap, and the distance between E_F and the bottom of the conduction band or the top of the valence band is much greater than $k_0 T$. Therefore, the distribution of electrons in the conduction band and holes in the valence band can be described by the Boltzmann distribution function [86]. Due to the rapid decrease of $f(E)$ as energy

E increases, and the rapid increase of $1-f(E)$, most of the electrons in the conduction band are distributed near the bottom of the band, while the vast majority of holes in the valence band are distributed near the top of the band. In the non-degenerate case, the electron concentration in the conduction band can be calculated as follows:

$$dN = f_B(E) g_c(E) dE \quad (3.5)$$

Where $g_c(E)$ represents the number of quantum states within a unit energy interval near the bottom of the conduction band, and the expression is as follows:

$$g_c(E) = \frac{dZ}{dE} = \frac{V}{2\pi^2} \frac{(2m_n^*)^{3/2}}{\hbar^3} (E - E_c)^{1/2} \quad (3.6)$$

Where m_n^* is the effective mass of electrons near the bottom of the conduction band. Substituting Equations 3.3 and 3.6 into Equation 3.5, we obtain:

$$dN = \frac{V}{2\pi^2} \frac{(2m_n^*)^{3/2}}{\hbar^3} e^{-\frac{E-E_F}{k_0T}} (E - E_c)^{1/2} dE \quad (3.7)$$

Alternatively, it can be rewritten as the number of electrons per unit volume between energies E and $(E + \Delta E)$:

$$dn = \frac{dN}{V} = \frac{1}{2\pi^2} \frac{(2m_n^*)^{3/2}}{\hbar^3} e^{-\frac{E-E_F}{k_0T}} (E - E_c)^{1/2} dE \quad (3.8)$$

Integrating the above equation, the concentration of conduction band electrons in non-degenerate semiconductors under thermal equilibrium can be calculated as:

$$n = 2 \left(\frac{m_n^* k_0 T}{2\pi \hbar^2} \right)^{3/2} e^{-\frac{E_c - E_F}{k_0 T}} = N_c e^{-\frac{E_c - E_F}{k_0 T}} \quad (3.9)$$

Similar to the calculation of electron concentration in the conduction band, the concentration of holes in the valence band can be expressed as:

$$p = 2 \left(\frac{m_p^* k_0 T}{2\pi \hbar^2} \right)^{3/2} e^{\frac{E_v - E_F}{k_0 T}} = N_v e^{\frac{E_v - E_F}{k_0 T}} \quad (3.10)$$

The term m_p^* represents the effective mass of holes near the top of the valence band. Multiplying Equation 3.9 and Equation 3.10, we obtain the product of carrier concentrations as:

$$np = 4 \left(\frac{k_0}{2\pi \hbar^2} \right)^3 (m_n^* m_p^*)^{3/2} T^3 e^{-\frac{E_g}{k_0 T}} \quad (3.11)$$

E_g represents the energy gap between conduction and valence bands. From the above equation, the np product is a constant for a given semiconductor material and T , and this applies universally to both intrinsic and extrinsic semiconductors, that will be

introduced hereafter.

For intrinsic semiconductors, due to the generation of electron-hole pairs, the electron concentration n in the conduction band should be equivalent to the hole concentration p in the valence band, that is:

$$n = p = n_i \quad (3.12)$$

being n_i the intrinsic carrier density defined as:

$$np = n_i^2 = N_c N_v e^{-\frac{E_g}{k_0 T}} \quad (3.13)$$

By substituting equations 3.9 and 3.10 into 3.1.1. the Fermi level E_F of the intrinsic semiconductor can be determined as follows:

$$E_F = \frac{E_c + E_v}{2} + \frac{3k_0 T}{4} \ln \frac{m_p^*}{m_n^*} \quad (3.14)$$

For silicon, the value of m_p^*/m_n^* is 0.55, thus $\ln(m_p^*/m_n^*)$ is approximately below 2. Consequently, E_F is approximately within a range of $1.5k_0 T$ near the middle of the bandgap, where $k_0 T$ equals 0.026 eV at room temperature (300K).

3.1.2 Extrinsic semiconductors

Extrinsic semiconductors are semiconductors doped with impurities, that is, doping agents are added to intrinsic semiconductors altering their electrical properties compared to pure semiconductors. Depending on the kind of inserted impurities, *donors* or *acceptors* impurities, semiconductors are classified as n-type or p-type, respectively.

In n-type semiconductors, also known as electron-type semiconductors, the donor impurities - pentavalent elements - increase the electron density at the expenses of the mobile holes. The conductivity is therefore determined by negatively charged electrons as they are the majority of charge carriers.

Taking phosphorus doping in silicon as an example, as shown in Figure 3.3 (left), a phosphorus atom occupies the position of a silicon atom. Phosphorus has five valence electrons, four of which form covalent bonds with the surrounding four silicon atoms, leaving one valence electron whose binding to the donor nucleus is weak relatively to the covalent bonds. The binding energy can be evaluated starting from hydrogen atom energy levels, since we are effectively left by one single positive charge balanced by the spare electron, applying corrections for crystal periodic potential and dielectric constant of the material. For phosphorous in silicon, the binding energy is $\sim 44 \text{ meV}$ much less than the 1 eV of the energy gap. The donor atom can be then easily ionized and this spare electron reaches the conduction energy band, becoming a conducting electron

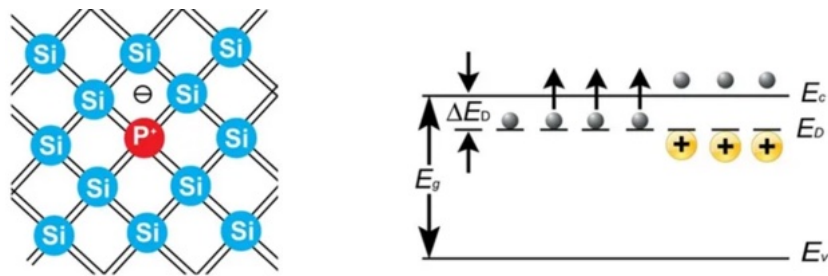


Figure (3.3) – Schematic representation of donor (left) impurities in Si and their ionization (right).

freely moving in the lattice. The ionization mechanism is sketched in Figure 3.3 (right): an extra energy level E_D is introduced in the gap by donor atoms, which lies close to the bottom of the conduction band. The energy needed to reach the conduction band is much smaller than the gap energy, $\Delta E_D = E_c - E_D \ll E_g$, and the electron can easily transition to the conduction band.

P-type semiconductor, also known as hole-type semiconductor, has an imbalance between electron density and hole density due to the presence of acceptor impurities - trivalent elements - resulting in a higher density of mobile holes than conducting electrons. Conductivity is determined by positively charged holes as majority charge carriers.

Taking boron doping in silicon as an example, as shown in Figure 3.4 (left), a boron atom occupies the position of a silicon atom. When it forms covalent bonds with the surrounding four silicon atoms, it lacks one electron, that it *accepts* from another silicon atom elsewhere, creating a hole in the covalent bonds of the silicon crystal. The binding of this boron ion to the hole is weak, and once again it the binding energy can be evaluated in the hydrogen like situation as $\ll E_g$, such that it can easily become a conducting hole moving freely in the crystal lattice's covalent bonds. This mechanism is sketched in Figure 3.4 (right): an extra energy level E_A is introduced in the gap by acceptor atoms, which lies close to the top of the valence band. The energy needed to an electron of the valence band to reach the acceptor level is much smaller than the gap energy, $\Delta E_A = E_A - E_V \ll E_g$, and the electron can easily transition from the valence band, leaving a hole freely moving in the lattice.

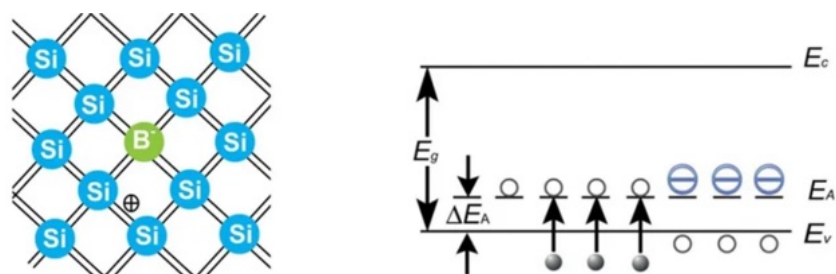


Figure (3.4) – Schematic representation of acceptor (left) impurities in Si and their ionization (right).

For n-type semiconductors the probability of electrons occupying the donor level can be expressed as :

$$f(E_D) = \frac{1}{1 + \frac{1}{g_D} e^{\frac{E_D - E_F}{k_0 T}}} \quad (3.15)$$

and for p-type semiconductors the probability of the hole occupying the acceptor energy can be expressed as:

$$f(E_A) = \frac{1}{1 + \frac{1}{g_A} e^{\frac{E_F - E_A}{k_0 T}}} \quad (3.16)$$

In the equation, g_D represents the ground state degeneracy of the donor energy level, while g_A represents the ground state degeneracy of the acceptor energy level. For silicon, $g_D = 2$ and $g_A = 4$.

Therefore, the electron density in the donor energy level is :

$$n_D = N_D f(E_D) = \frac{N_D}{1 + \frac{1}{g_D} e^{\frac{E_D - E_F}{k_0 T}}} \quad (3.17)$$

where N_D is the density of donor impurities, and the ionized donor density is:

$$n_D^+ = N_D - n_D = N_D [1 - f(E_D)] = \frac{N_D}{1 + g_D e^{-\frac{E_D - E_F}{k_0 T}}} \quad (3.18)$$

when $E_D - E_F \gg k_0 T$, $n_D \approx 0$, and simultaneously $n_D^+ \approx N_D$.

Similarly, the hole density n at the acceptor energy level is:

$$p_A = N_A f(E_A) = \frac{N_A}{1 + \frac{1}{g_A} e^{\frac{E_F - E_A}{k_0 T}}} \quad (3.19)$$

where N_A is the density of acceptor impurities, and the ionized acceptor density is:

$$p_A^- = N_A - p_A = N_A [1 - f(E_A)] = \frac{N_A}{1 + g_A e^{-\frac{E_F - E_A}{k_0 T}}} \quad (3.20)$$

when $E_F - E_A \gg k_0 T$, $p_A \approx 0$, and simultaneously $p_A^- \approx N_A$.

The condition of electrical neutrality implies that the density of positive (holes and ionized donor nuclei) and negative (electrons and ionized acceptor nuclei) charges should balance:

$$n + p_A^- = p + n_D^+ \quad (3.21)$$

Equations 3.21 and 3.13 can be solved for n, p:

$$n = \frac{N_D - N_A}{2} + \left[\left(\frac{N_D - N_A}{2} \right)^2 + n_i^2 \right]^{\frac{1}{2}} ; \quad p = \frac{N_A - N_D}{2} + \left[\left(\frac{N_A - N_D}{2} \right)^2 + n_i^2 \right]^{\frac{1}{2}} \quad (3.22)$$

This is a general result, that, however, in most cases can be simplified:

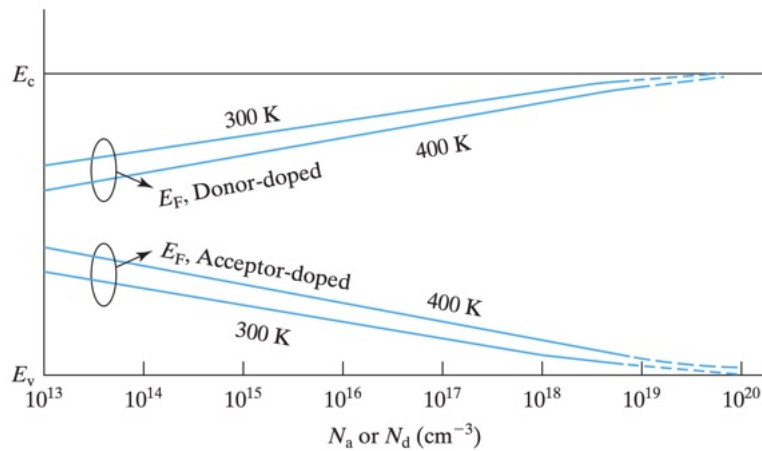


Figure (3.5) – Location of Fermi level vs. dopant concentration in Si at 300 and 400 K [84].

- a) if $N_D - N_A \gg n_i$, i.e. we are in an n-type semiconductor, $n = N_D - N_A$; $p = n_i^2/n$, and furthermore if $N_D \gg N_A$ it will be $n = N_D$ and $p = n_i^2/N_D$;
- b) if $N_A - N_D \gg n_i$, i.e. we are in a p-type semiconductor, $p = N_A - N_D$; $n = n_i^2/p$, and furthermore if $N_A \gg N_D$ it will be $p = N_A$ and $p = n_i^2/N_D$.

From equations 3.22 also the Fermi level can be evaluated as a function of the donor/acceptor concentrations, as depicted in Fig. 3.5.

3.1.3 The p-n junction

A p-n junction is formed at the interface joining an n-type and a p-type semiconductor, as schematically represented for a step junction in Fig. 3.6. The n-type or p-type semiconductors taken individually are electrically neutral with no net flow of charge in absence of an external field. However, as they come into contact, due to the concentration gradient of carriers on the junction interface, diffusion occurs with holes moving from the p-region to the n-region and electrons moving from the n-region to the p-region. Therefore, a *depletion* region built up across the junction interface with

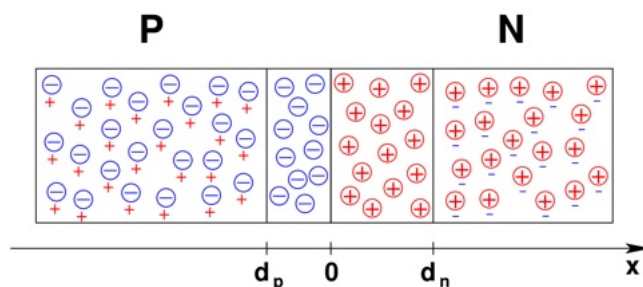


Figure (3.6) – An ideal step p-n junction.

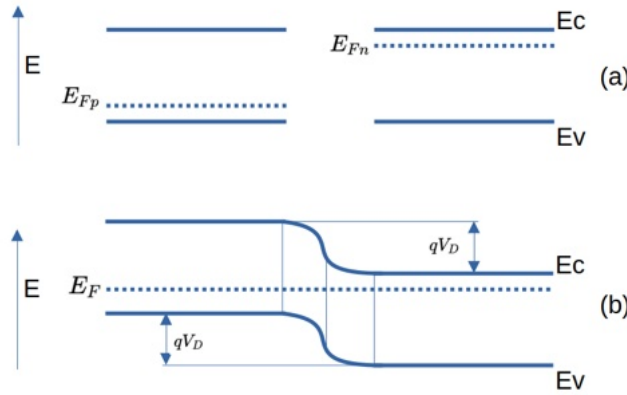


Figure (3.7) – (a) n-p junction; (b) the energy diagram of the pn junction at equilibrium.

no majority carriers and negative fixed charge on the p side and positive fixed charge on the n side (see Figure 3.6).

The fixed spatial charge distribution in the depletion region generates an electric field pointing from the n-region to the p-region, known as the *built-in* electric field. The built-in field causes a drift motion of the carriers, e^- from p to n side, and h from n to p side, which opposes to their diffusion across the junction. As diffusion proceeds the built-in field strengthens and finally an equilibrium is reached between drift and diffusion, with no net charge flow across the junction. This can be described using energy band properties, as depicted in Fig. 3.7.

The energy band diagram of the p-type and n-type semiconductors taken individually are sketched in the top-most drawing (a): the Fermi level of the p-type semiconductor is close to the valence band, conversely on the n-type semiconductor it is close to the conduction band. At equilibrium, the Fermi level should be the same on the two sides of the junction, that implies that the energy bands are bent in correspondence of the depletion region due to the potential of the built-in field (b). This is the *potential barrier* that electron (holes) should overcome to flow from n-side (p-side) to p-side (n-side) of the junction.

As shown in Figure 3.8, the potential plot (a) shows up as an upside mirror image in the energy band, $-x_p$ and x_n in the figure respectively represent the boundaries of the n-region and p-region depletion layers. In fact, assuming zero potential in the p-type semiconductor far from the junction, the potential $V(x)$ at a point x in the barrier region is positive. For electrons, the potential energy at point x in the barrier region is $E(x) = -qV(x)$. For non-degenerate materials, according to equation 3.8, the electron concentration $n(x)$ at point x is given by:

$$n(x) = \int_{E(x)}^{\infty} \frac{1}{2\pi^2} \frac{(2m_{dn})^{3/2}}{\hbar^3} e^{\frac{E_F-E}{k_0T}} [E - E(x)]^{1/2} dE \quad (3.23)$$

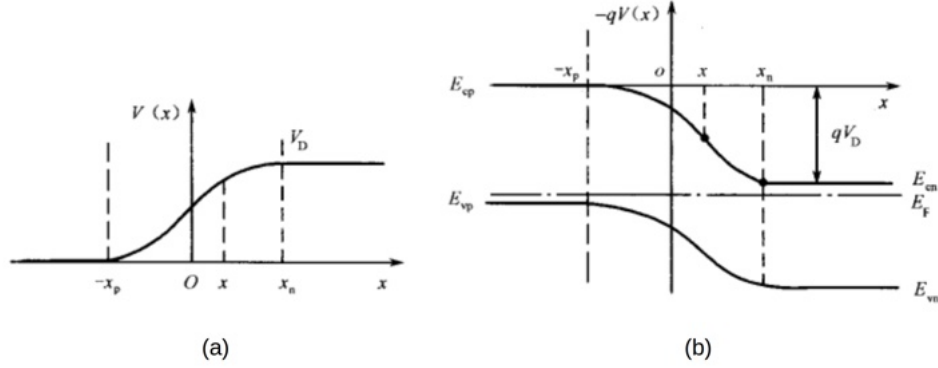


Figure (3.8) – Potential across the junction (a) and its effect on the energy band diagram (b).

Integrating the above equation, we obtain:

$$n(x) = \frac{2}{\hbar^3} \left(\frac{m_{dn} k_0 T}{2\pi} \right)^{3/2} e^{\left[\frac{E_F - E(x)}{k_0 T} \right]} = N_c e^{\left[\frac{E_F - E(x)}{k_0 T} \right]} \quad (3.24)$$

Since $E(x) = -qV(x)$ and $n_{n0} = N_c e^{\left[\frac{E_F - E_{cn}}{k_0 T} \right]}$, while $E_{cn} = -qV_D$, therefore:

$$n(x) = n_{n0} e^{\left[\frac{qV(x) - qV_D}{k_0 T} \right]} \quad (3.25)$$

Similarly, we can obtain the hole concentration at point x as:

$$p(x) = p_{n0} e^{\left[\frac{qV_D - qV(x)}{k_0 T} \right]} \quad (3.26)$$

Where n_{n0} and n_{p0} respectively represent the equilibrium electron concentrations in the n-region and p-region. Equations 3.25 and 3.26 can be used to estimate the carrier concentration at various points in the pn junction depletion region. For example, assuming a barrier height of 0.7 eV, at point x where the potential energy is 0.1 eV higher than the bottom of the conduction band in the n-region:

$$n(x) = n_{n0} e^{-\frac{0.1}{0.026}} \approx \frac{n_{n0}}{50} \approx \frac{N_D}{50} \quad (3.27)$$

$$p(x) = p_{n0} e^{-\frac{0.6}{0.026}} \approx 10^{-10} p_{p0} \approx 10^{-10} N_A \quad (3.28)$$

N_D and N_A respectively represent the concentrations of donor and acceptor impurities. Generally, at room temperature, for the vast majority of the depletion region, the impurities within it have already ionized. As seen from the above equation, in the depletion region, the carrier concentration is much smaller compared to the carrier concentration in the n and p regions, as if exhausted. Therefore, the depletion region is usually referred to as the depletion layer, implying that the carrier concentration within it is very small

and can be neglected, and the space charge density equals the impurity concentration. By solving the Poisson equation for the depletion layer electric field, we can determine the width of the depletion layer. The derivation process is as follows:

$$\nabla^2\psi(x) = -\frac{\rho(x)}{\epsilon}, \rho(x) = \begin{cases} -eN_A, & -x_p < x < 0 \\ eN_D, & 0 < x < x_n \end{cases} \quad (3.29)$$

The electric field can be determined from the Poisson equation as follows:

$$\begin{cases} \frac{d\psi_1}{dx} = \frac{q}{\epsilon}N_Ax + C_1, & p \text{ region} \\ \frac{d\psi_2}{dx} = \frac{q}{\epsilon}N_Dx + C_2, & n \text{ region} \end{cases} \quad (3.30)$$

And the potential can be determined as follows:

$$\begin{cases} \psi_1(x) = \frac{q}{2\epsilon}N_Ax^2 + C_1x + C_3, & p \text{ region} \\ \psi_2(x) = \frac{q}{2\epsilon}N_Dx^2 + C_2x + C_4, & n \text{ region} \end{cases} \quad (3.31)$$

According to the continuity condition of the electric field at $x = 0$ and setting the potential there to zero, we obtain:

$$\begin{cases} C_1 = C_2 \\ C_3 = C_4 = 0 \end{cases} \quad (3.32)$$

According to the boundary conditions:

$$\begin{cases} \frac{d\psi_1}{dx}(-x_p) = 0 \\ \frac{d\psi_2}{dx}(-x_n) = 0 \\ \psi_2(x_n) - \psi_1(-x_p) = V + V_0 = V_T \end{cases} \quad (3.33)$$

that is:

$$\begin{cases} -\frac{q}{\epsilon}N_Ax_p + C_1 = 0 \\ -\frac{q}{\epsilon}N_Dx_n + C_1 = 0 \\ -\frac{q}{2\epsilon}N_Dx_n^2 + C_1x_n - \frac{q}{2\epsilon}N_Ax_p^2 + C_1x_p = V + V_0 = V_T \end{cases} \quad (3.34)$$

V_0 represents the built-in voltage of the pn junction. V represents the externally applied voltage to the pn junction, when it does not exist, $V = 0$. combining the space charge neutrality condition:

$$N_Ax_p = N_Dx_n \quad (3.35)$$

we obtain:

$$\begin{cases} x_n = \sqrt{\frac{2\epsilon V_T}{q} \frac{N_A}{N_D(N_D+N_A)}} \\ x_p = \sqrt{\frac{2\epsilon V_T}{q} \frac{N_D}{N_A(N_A+N_D)}} \end{cases} \quad (3.36)$$

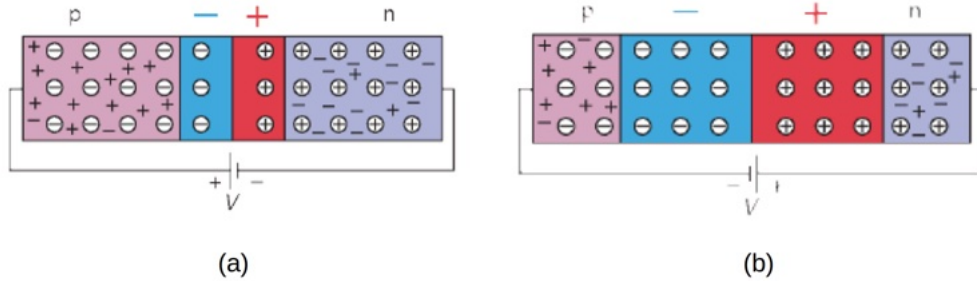


Figure (3.9) – (a) p-n junction with forward bias. (b) p-n junction with Reverse bias [87].

Therefore, the width of the depletion layer is:

$$W = x_p + x_n = \sqrt{\frac{2\epsilon}{q} \left(\frac{N_A + N_D}{N_A N_D} \right) V_T} \quad (3.37)$$

From the above equation, it can be seen that when there is an external voltage applied, if a positive voltage is applied to the n-type region and a negative voltage is applied to the p-type region, then V becomes positive, and $V + V_0 = V_T$ increases, causing the depletion layer width to further expand. Conversely, if a positive external voltage is applied to the p-type region and a negative voltage is applied to the n-type region, then V becomes negative, and $V + V_0 = V_T$ decreases, causing the depletion layer width to shrink. This is illustrated in Figure 3.9.

In practical applications, the doping concentration N_A is typically much greater than N_D , so $x_p \ll x_n$. Furthermore, considering that the built-in voltage V_0 is generally only $0.7V$, equation 3.37 can be rewritten as:

$$W \approx x_n \approx \sqrt{\frac{2\epsilon V}{qN_D}} = \sqrt{2\epsilon\mu\rho V}, \rho = \frac{1}{q(\mu_h n_e)} \quad (3.38)$$

Therefore, for a detector with a thickness D , as the reverse bias increases, when the depletion layer width increases to equal the thickness of the silicon detector (fully depletion), its full depletion voltage is represented by Equation 3.39. The operating voltage of a typical silicon detector is usually slightly higher than the full depletion voltage, known as over-depletion. Further increasing the voltage effectively drives out the carriers generated by thermal excitation from the depletion layer, and increases the drift velocity of carriers, reducing losses during carrier diffusion.

$$V_{Fdepl} = \frac{D^2}{2\epsilon\mu\rho} \quad (3.39)$$

In addition to changes in the depletion layer width, when the external voltage applied to the pn junction is altered, the current-voltage ratio of the pn junction also varies

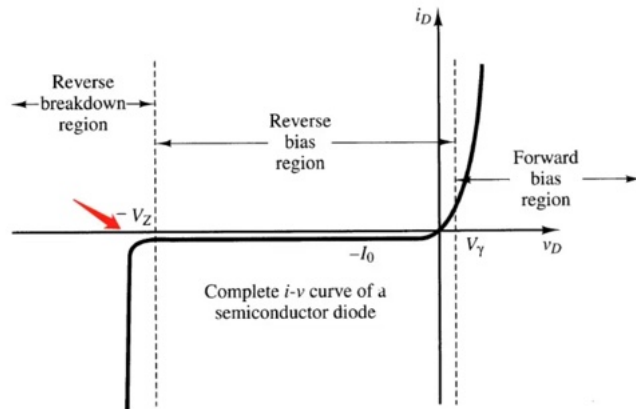


Figure (3.10) – p-n junction VI characteristics.

and is nonlinear, as shown in Figure 3.10. For an ideal pn junction, this nonlinearity can be described by the Shockley diode equation.

$$J = J_s \left[e^{\frac{qV}{k_0 T}} - 1 \right] \quad (3.40)$$

The above equation indicates that under forward bias, the forward current density increases rapidly with the forward bias voltage in an exponential relationship. At room temperature where $k_0 T / q = 0.026V$, thus $e^{\frac{qV}{k_0 T}} \gg 1$, Equation 3.40 can also be expressed as:

$$J = J_s e^{\frac{qV}{k_0 T}} \quad (3.41)$$

Under reverse bias voltage, where $V < 0$, when $q|V| \gg k_0 T$, $e^{\frac{qV}{k_0 T}} \rightarrow 1$, Equation 3.40 becomes:

$$J = -J_s \quad (3.42)$$

In the above equation, the negative sign indicates that the direction of the current density is opposite to that under forward bias. Additionally, the reverse current density remains constant, independent of the applied voltage. Therefore, $-J_s$ is referred to as the reverse saturation current density. Experimental observations have shown that when the reverse bias increases to a certain value, the reverse current density suddenly begins to increase rapidly. This phenomenon is known as pn junction breakdown. There are three types of breakdown in pn junctions [88]: Avalanche breakdown, Zener breakdown, and Thermal runaway.

Avalanche Breakdown:

As the reverse bias voltage increases, the force acting on charge carriers in the electric field increases, leading to an increase in acceleration. Consequently, they gain more

kinetic energy. When their kinetic energy becomes sufficiently large to collide with lattice atoms and dislodge the valence electrons from the atomic nucleus, overcoming the covalent bond energy, an additional pair of electron-hole is generated. These newly generated electron-hole pairs will continue to accelerate under the influence of the electric field. When their kinetic energy is large enough, they will continue to collide, producing further electron-hole pairs. This rapid increase in carrier concentration, akin to the process of an avalanche, is thus termed avalanche breakdown.

Zener Breakdown:

As the reverse bias voltage increases, the valence band of the p-type region in the band diagram will align with or even slightly exceed the conduction band of the n-type region. Due to the abundance of electrons in the valence band of the p-type region and the abundance of holes in the conduction band of the n-type region, according to the quantum mechanical tunnelling effect, the charge carriers in the valence band of the p-type region may no longer need to overcome the barrier height and can directly tunnel into the conduction band of the n-type region.

Thermal Runaway:

Unlike the previous two types of breakdown, thermal runaway is irreversible. Under higher reverse bias voltages, charge carriers gain energy, which is then transferred to the lattice through collisions, increasing the lattice energy and consequently raising the temperature of the pn junction. As the temperature rises, the concentration of intrinsic carriers rapidly increases, leading to a rapid increase in reverse saturation current. The increase in reverse saturation current further raises the temperature of the pn junction, causing an infinite increase in both current and temperature, ultimately resulting in the destruction of the pn junction.

3.2 The single-sided microstrip detectors

In general, pure silicon is not suitable for direct use as a medium for particle detection. The average ionization energy of silicon is $W=3.62$ eV, and the average energy loss per unit distance (dE/dx) for a Minimum Ionizing Particle (MIP) is 3.87 MeV/cm [89]. Therefore, for a pure silicon medium with a thickness $d = 300\mu\text{m}$ and an area $A = 1\text{cm}^2$,

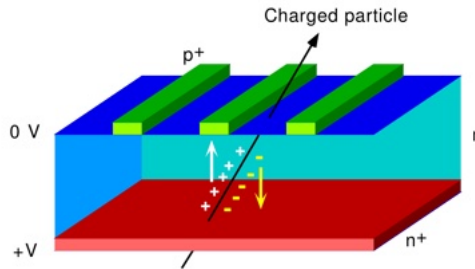


Figure (3.11) – Working principle of a single-sided microstrip detector.

the number of electron-hole pairs produced by a MIP is:

$$N_{MIP} = \frac{dE/dx \cdot d}{W} = \frac{3.87 \cdot 10^6 \text{ eV/cm} \cdot 0.03 \text{ cm}}{3.62 \text{ eV}} \approx 3.2 \cdot 10^4 \quad (3.43)$$

For the same volume of pure silicon medium, at $T = 300\text{K}$, the number of intrinsic charge carriers generated due to thermal effects is:

$$N_{intrinsic} = n_i \cdot d \cdot A = 1.45 \cdot 10^{10} \text{ cm}^{-3} \cdot 0.03 \text{ cm} \cdot 1 \text{ cm}^2 \approx 4.35 \cdot 10^8 \quad (3.44)$$

Then, the number of carriers generated due to thermal effects is much greater than the number of carriers generated by MIPs and MIP signals would be overshadowed by thermal noise. To overcome the background from thermal noise, the most common method is to construct a pn junction beneath the surface of pure silicon and operate it at an over-depletion voltage under reverse bias.

Thanks to the development of silicon semiconductor technology, it is now possible to fabricate strip or pixel-like electrodes on the surface of silicon to achieve high spatial resolution. In this thesis, we will focus on discussing single-sided silicon strip detectors¹. As shown in Figure 3.11, on the upper surface of the n-type silicon wafer, there are uniformly parallel heavily doped p^+ microstrips. The lower surface consists of a heavily doped n^+ layer formed after doping. Under sufficiently high reverse bias, the intermediate portion between the upper and lower surfaces forms the entire depletion layer, known as the sensitive region of the detector. The thickness of this sensitive region cannot be too large, as it may lead to the generation of secondary particles and multiple scattering. Conversely, it cannot be too small to ensure the generation of a sufficiently large signal by producing enough electron-hole pairs. An appropriate value is around $300\mu\text{m}$.

When electron-hole pairs are generated in the detector, they drift towards the electrodes under the influence of an applied electric field, although it should be mentioned that

¹in jargon, this is referred as SSSD, while the ones in double-side technology are referred as DSSD. Generally, when is clear from the context (i.e. only one technology is used), they are also referred, in short, as SSD.

the signal produced on the electrodes is due to the instantaneous change of electric flux through the electrodes, rather than the charge they receive [90],[91]. This can be expressed as:

$$i = -qvE_w \quad (3.45)$$

where q is the charge moving with velocity v , and E_w is commonly referred to as the weighted electric field, which depends solely on the geometry of the detector. Despite the opposite drift directions of electrons and holes, their contributions to the direction of the signal current are the same due to the opposite polarity of the charges they carry. Another effect that should be taken into account when studying the spatial distribution of the signal, is the e/h spatial diffusion while drifting, which follows a time-dependent Gaussian distribution with a standard deviation of:

$$\sigma_D = \sqrt{2Dt} \quad (3.46)$$

Where D is the diffusion coefficient, which depends on the properties of the material and t the diffusion time. It should be noted that $D = KT/e\mu$, being μ the mobility of the carriers. Diffusion time t can be expressed as $t = d/v = d/\mu E$ so that the width of the distribution is the same for e/h carriers:

$$\sigma_D \sim \sqrt{2 \frac{kT}{e} \frac{d^2}{V_{bias}}} \quad (3.47)$$

Thanks to diffusion signal can reach adjacent strips, resulting in an improved spatial resolution.

In the following, we will introduce the key structures of single-sided silicon strip detectors.

3.2.1 AC coupling and DC coupling

There are two methods to extract the generated charge signal from the heavily doped p+ strips: Direct Current (DC) and Alternate Current (AC) coupling. As shown in Figure 3.12(b), in the case of DC coupling, the heavily doped p^+ strips directly contact the aluminum readout strips. Its advantage lies in its simple structure and lower production cost. However, DC coupling can lead to baseline drift of the detector, affecting its dynamic range, even causing detector saturation, and may result in leakage current superimposing on the readout signal, increasing noise. In contrast, in the case of AC coupling, as shown in Figure 3.12(a), a layer of SiO_2 is added between the aluminum readout strips and the heavily doped p^+ strips to form a capacitive structure. In this case, the electrical signal obtained by the detector is capacitively coupled to the readout

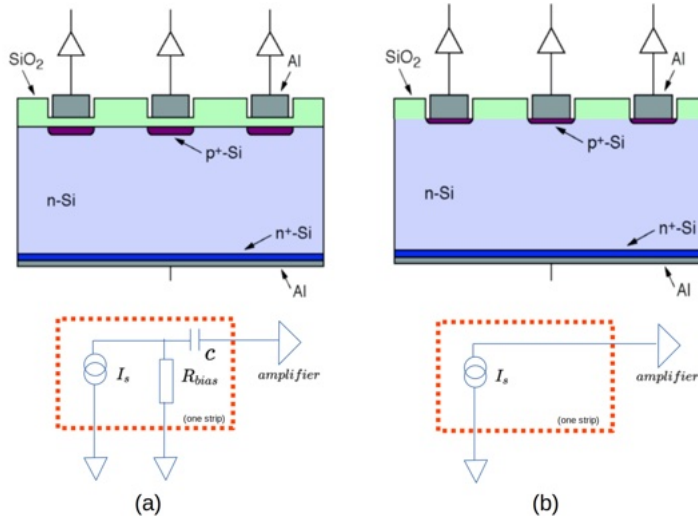


Figure (3.12) – (a) AC coupled strip sensor. (b) DC coupled strip sensor.

circuit. The advantage is that it can shield the influence of leakage current on the readout signal, and bias resistors can also avoid baseline drift. Therefore, AC coupling has been widely used in silicon microstrip detectors.

3.2.2 Bias rings

In order to operate the detector in full depletion mode and to ensure the correct functioning of the charge division process, it is necessary to provide each p^+ strip with a sufficiently high and completely identical reverse bias voltage. There are three common voltage biasing methods: FOXFET biasing, punch-through biasing, and polysilicon biasing. Figure 3.13 illustrates schematic diagrams of these three biasing methods.

Punch – through biasing : the heavily doped p^+ stripes are slightly spaced from the bias ring, meaning they are not directly connected. The bias ring is grounded, while a positive voltage is applied to the backplane. Because the p^+ stripes are not grounded, they have almost the same potential as the backplane. When the voltage applied to the backplane increases, the guard ring depletion zone extends and eventually merges with the strip depletion zones. After the depletion areas have merged, a hole current from the strips to the guard ring appears as there is no barrier against holes at the reverse junction. This punch-through current charges the strips, spreading the strip depletion volume. The punch-through current stops as soon as the strips are charged enough to establish a potential barrier to retain holes. Subsequent voltage increases will extend the depletion zone, while the potential difference between the guard ring and the strips will remain practically constant. With this method, all the strips are at the same voltage,

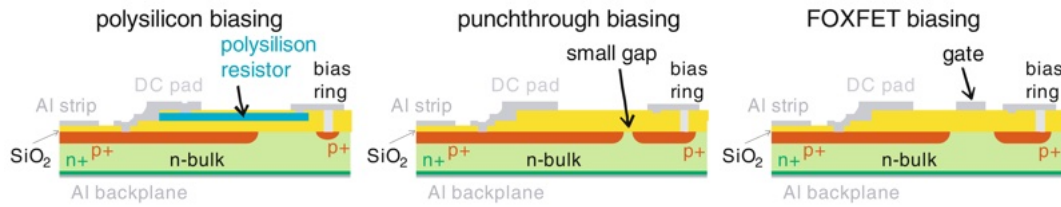


Figure (3.13) – Schematic diagrams of the three methods for applying bias voltage [92].

and as the guard ring is biased, the depletion zone will extend beyond the outermost strips.

FOXFET biasing : the region between the strips and the bias ring is supplemented with metal gates at the top, forming a structure similar to that of a MOSFET. On the p-side of a microstrip detector, the bias acts as the source, while each strip serves as a drain. The function of the gate is to exert good and uniform control over the strip polarization resistances. When this gate electrode is activated by an external signal, it establishes a pathway between the strips and the bias ring, equalizing their voltages.

Polysilicon biasing : a voltage path is formed between the bias ring and the strips through polycrystalline silicon resistors. High resistance values are achieved by depositing winding poly structures. Therefore, the significant drawback of polycrystalline silicon biasing is the use of more material and additional manufacturing steps, which further increases costs. However, compared to the other two methods, polycrystalline silicon biasing offers better radiation tolerance. Hence, this method is the most widely used in silicon microstrip detectors.

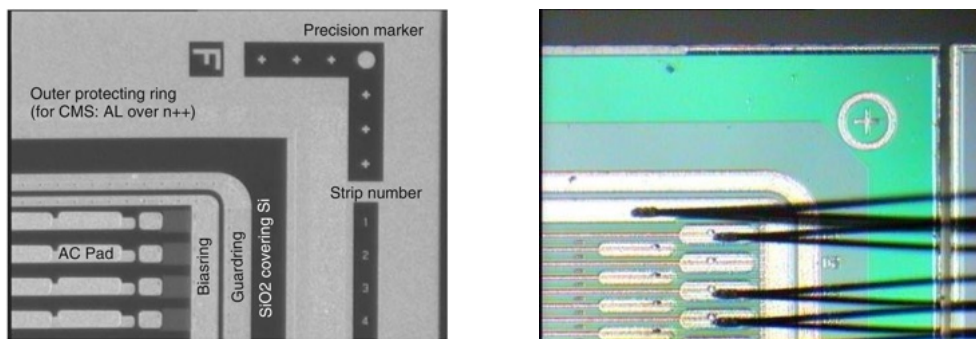


Figure (3.14) – Left: the top view of a sensor with the ring structures [92]. Right: the top view of a sensor with the interleaved readout scheme.

3.2.3 Guard rings

At the outer periphery of the detector bias ring, there is typically a guard ring, as shown in Figure 3.14 (left). Cutting silicon detectors often leads to the creation of defects along their edges, which in turn increases the surface conductivity of those edges. During detector operation, bias voltage applied to the bottom electrode causes current to flow from the edges of the detector into the active area, affecting the detector's performance. The guard ring can establish a stable electric field outside the active area of the detector, reducing the impact of surface defects on detector performance.

3.2.4 Floating strips

The core performance parameter of silicon microstrip detectors is its spatial resolution. It is evident that the most direct method to improve position resolution is by reducing the pitch between strips. Smaller pitch leads to better position resolution. However, reducing the strip pitch not only increases the manufacturing cost of the detector but also significantly increases the number of electronic readout channels, resulting in higher power consumption. A reasonable solution, as shown in Figure 3.14 [right], is to adopt an interleaved readout scheme while further reducing the strip pitch. This involves reading one strip every N strips. The strips between two readout strips are referred to as floating strips. Although the floating strips are not directly connected to the readout system, the induced signals on them can be coupled to adjacent readout strips through the capacitance between the strips and the capacitance between the strips and the backplane. While this approach can improve the charge sharing effect between strips and hence enhance position resolution while maintaining the same number of electronic readout channels, it may reduce charge collection efficiency. The impact of floating strips on detector charge collection efficiency is discussed later in this Chapter (3.4.2).

3.2.5 Ladder

Silicon sensors have a typical size $< 100 \text{ cm}^2$, and to instrument large surfaces, as those of AMS-02 L0 or the HERD SCD, thousand sensors or more will be needed. Would be both inefficient and hardly manageable to readout signals from each sensor separately. The space needed to locate front end electronics would in fact reduce the area available for signal detection, and the large number of readout channels would have an impact on power consumption and signal handling. An effective solution to this problem is to



Figure (3.15) – Left: detail of the $25 \mu\text{m}$ Al wire bonding between two silicon sensors. Right: L0 ladder during production, ten sensors are daisy chained and connected to the front end electronics on the left end.

build arrays of sensors, usually referred as *ladders*, where strips of adjacent sensors are connected together in a daisy-chain by thin bonds, with front end electronics placed at the ladder end, as shown in figure 3.15. The advantage of this configuration is that it allows for a larger detection area while limiting the number of readout channels. However, the drawback is that longer strips have greater capacitance, which may lead to more significant electrical noise in the front-end electronics.

3.3 Signal formation and acquisition

All semiconductor detector systems include the same basic elements (as shown in figure 3.16): radiation is absorbed by the sensor and then converted into an electrical signal. This initial signal is typically weak, being amplified within a preamplifier, then fed into a pulse shaper, and finally converted into a digital format for storage. Below, we will introduce each of these elements.

3.3.1 Energy deposition

The electromagnetic interaction between charged particles and detector media typically involves three mechanisms: ionization, Cherenkov radiation, and bremsstrahlung. Ionization is the most widely utilised in semiconductor detectors. When charged particles

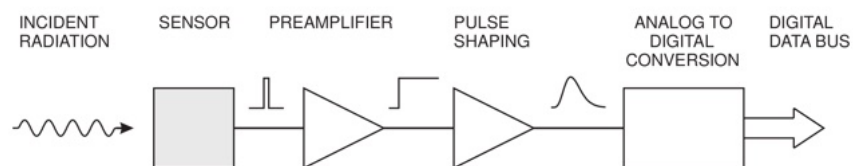


Figure (3.16) – Basic detector elements [93].

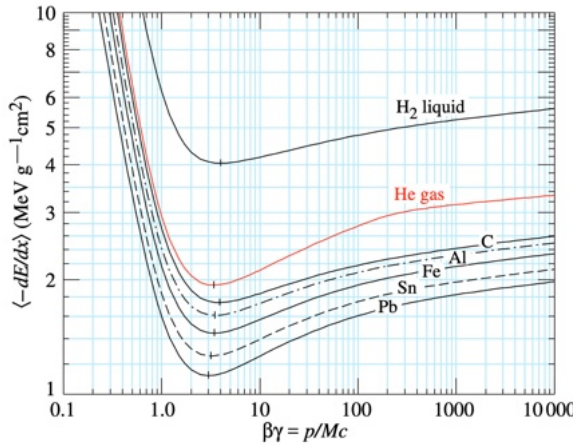


Figure (3.17) – Mean energy loss rate of charged particles in different substances [94].

traverse through the medium of a semiconductor detector, they lose kinetic energy through electromagnetic interactions, with some of the kinetic energy transferred to the electrons within the medium. If the electrons acquire sufficient energy, they can undergo transitions, resulting in the formation of free electrons and positively charged ions. Therefore, this process is termed ionization. For heavier charged particles, the average energy loss as they traverse through the medium is described as a function of their velocity β and γ factor by the Bethe-Bloch equation: [94].

$$\left\langle -\frac{dE}{dx} \right\rangle = Kz^2 \frac{Z}{A} \frac{1}{\beta^2} \left[\frac{1}{2} \ln \frac{2m_e c^2 \beta^2 \gamma^2 W_{max}}{I^2} - \beta^2 - \frac{\delta}{2} \right] \quad (3.48)$$

where m_e denotes the electron mass, z represents the charge of the incident particle, Z and A represent the atomic number and atomic mass of the medium, I represents the average excitation energy of the medium; δ is a parameter describing the degree of screening of the transverse electric field of the incident relativistic particle by the atomic electron charge density and W_{max} is a mass dependent factor which accounts for the maximum possible energy transfer to a recoil electron. Figure 3.17 depicts the variation with $\beta\gamma$ of the average ionization energy loss of single charged particles in different substances. A minimum is observed for $\beta\gamma \sim 3 - 4$, which defines the *MIP* region. Energy losses are much larger for slow particles, as they have longer interaction time to ionize the medium, and a moderate rise is observed at higher velocities due to the enlarged interaction range with the medium by the increase of transverse electric field from Lorentz contraction. The rise is then mitigated as the velocity further increases by the shielding effect of atomic electron charge density, which effectively leads to saturation of energy loss.

Equation 3.48 describes the average ionization energy loss of incident particles in

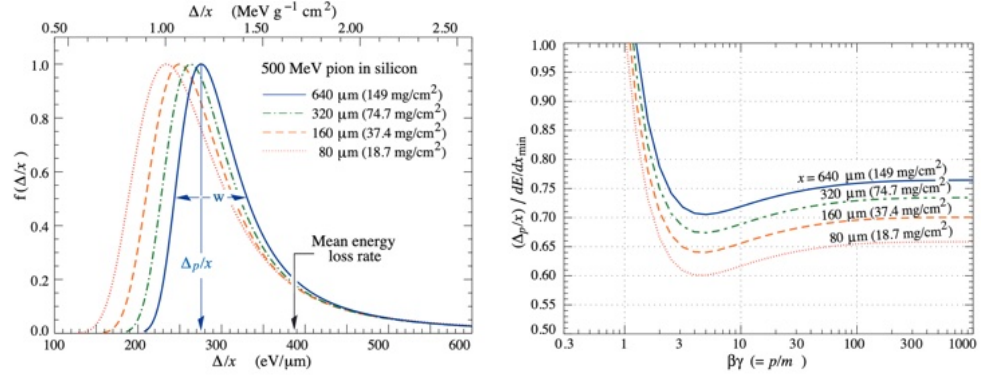


Figure (3.18) – Energy loss in thin silicon sensors, detailed explanation in the text [94].

a medium. However, the actual ionization energy loss fluctuates when dealing with a single particle in a thin medium, the mean of the energy loss given by the Bethe equation becomes ill-defined experimentally and the most probable energy loss becomes the relevant quantity. For detectors of relatively small thickness, in fact, the energy loss distribution approaches a Landau distribution due to the presence of seldom energetic collision of the incident particles and electrons of the detector medium. Fig. 3.18[left] illustrates the distribution of the energy loss Δ per unit length (μm) of 500 MeV pions in silicon sensors of different thicknesses. Normalization of different curves is to unity at the most probable value. The mean energy loss rate is also indicated as a reference. On the right, the most probable energy loss in silicon, scaled to the mean loss of a minimum ionizing particle is shown as a function of $\beta\gamma$: for a $\sim 300\mu\text{m}$ thick silicon, the most probable value of a MIP signal is $\sim 60\%$ of the average loss.

3.3.2 Noise contributions

In a detector, there are many factors associated with noise, primarily including the detector's load capacitance (C_d), leakage current caused by reverse bias (I_L), parallel resistance of strip metallization (R_s), and polarization resistance (R_p) that can be modeled as shown in Fig. 3.19. The contributions of different noise sources to the total noise follow a quadratic summation relationship [95], and are typically presented in the form of equivalent noise charge (ENC):

$$ENC_{tot} = \sqrt{ENC_{C_d}^2 + ENC_{I_L}^2 + ENC_{R_p}^2 + ENC_{R_s}^2} \quad (3.49)$$

1. noise caused by leakage current:

$$ENC_{I_L} = \frac{e}{2} \sqrt{\frac{I_L \cdot t_p}{q_e}} \quad (3.50)$$

2. noise caused by polarization resistance:

$$ENC_{R_p} = \frac{e}{q_e} \sqrt{\frac{I_L \cdot t_p}{q_e}} \quad (3.51)$$

3. noise caused by strip metallization:

$$ENC_{R_s} = C_d \cdot \frac{e}{q_e} \sqrt{\frac{k_B T R_s}{6 t_p}} \quad (3.52)$$

4. noise caused by detector's load capacitance:

$$ENC_{C_d} = a + b \cdot C_d \quad (3.53)$$

where k_B is the Boltzmann constant, e is a mathematical constant, q_e is the electron charge, t_p is the shaping time of the preamplifier, T is the operating temperature of the detector, and a and b are parameters determined by the preamplifier chip. For example, the charge-sensitive amplifier used both in AMS-L0 and HERD-SCD is the chip IDE1140 [96], from IDEAS company, with a shaping time of $6.5\mu s$ and noise parameters $a = 139 e$, $b = 5 e/pF$. The b parameter is usually proportional to the intrinsic voltage noise of the IDE1140 chip and inversely proportional to the shaping time.

Additionally, for multi-channel readout electronic systems, such as chip IDE1140 which possesses 64 readout channels, all channels share the same electronic unit with a common signal loop. During the signal readout process, signal currents can cause voltage fluctuations which are superimposed on all connected readout channels, resulting in common-mode noise. When performing data analysis and processing for detectors, it is necessary to analyze and subtract this common-mode noise.

3.3.3 Charge-sensitive amplifier

Charge-sensitive amplifiers are used to enhance the tiny signal released by particles crossing the detector, to minimize signal losses they are usually placed as close as

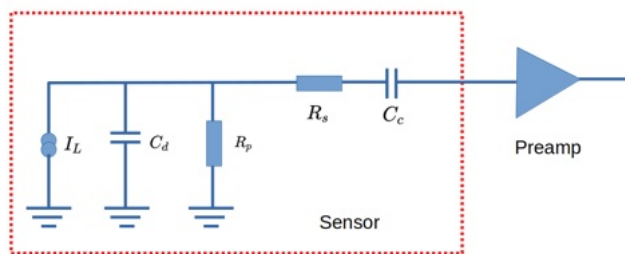


Figure (3.19) – The simplified noise model of a single channel.

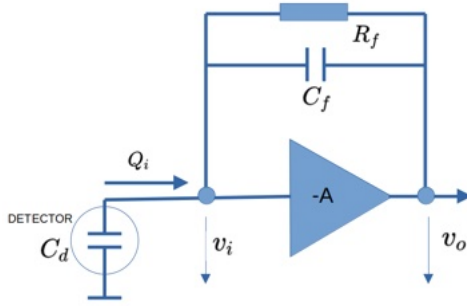


Figure (3.20) – Diagram illustrating the basic operating principle of a charge-sensitive amplifier [93].

possible to the detector itself, and are part of the so called *front-end* electronics. As shown in Figure 3.20, the charge-sensitive amplifier mainly consists of a reverse amplifier with high input impedance and a feedback capacitor C_f connected to the input and output terminals of the amplifier. The high resistance feedback resistor R_f connected in parallel to C_f is used to discharge the charge accumulated on C_f . When a charge signal generates a voltage v_i at the input of the amplifier, the output voltage at the output terminal is $v_o = -Av_i$. At this time, the voltage difference across C_f is $v_f = (A + 1)v_i$, so the charge stored on C_f is $C_f(A + 1)v_i$. Since the input impedance of the amplifier is usually very high, the current flowing through the input terminal of the amplifier can be ignored, hence $Q_f = Q_i$. At this point, the equivalent input capacitance C_i of the reverse amplifier input terminal is:

$$C_i = \frac{Q_i}{v_i} = C_f(A + 1) \quad (3.54)$$

So for a unit input charge, the voltage gain of the amplifier is:

$$A_Q = \frac{v_o}{Q_i} = \frac{Av_i}{C_i v_i} = \frac{A}{A + 1} \cdot \frac{1}{C_f} \approx \frac{1}{C_f}, \text{ if } (A \gg 1) \quad (3.55)$$

From the above equation 3.55, it can be seen that the gain of the charge-sensitive amplifier is determined by the feedback capacitor C_f . When charged particles pass through the detector, the generated charge signal Q_s is partially distributed to the detector capacitance C_d , and partially to the input capacitance C_i of the charge-sensitive amplifier. The distribution ratio is:

$$\frac{Q_i}{Q_s} = \frac{C_i}{C_d + C_i} \quad (3.56)$$

From the above equation 3.56, it can be observed that when the capacitance C_i is much larger than the detector capacitance C_d , the electric signal Q_s generated by the detector will be predominantly collected by the feedback capacitance C_i of the charge-sensitive amplifier.

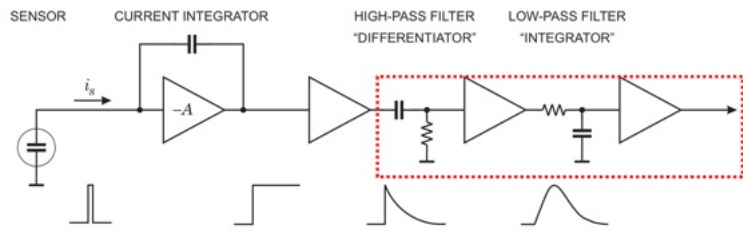


Figure (3.21) – Components of a pulse shaping system [93].

3.3.4 Pulse shaper

The signal output from the charge-sensitive amplifier must undergo processing by pulse shaping circuits to enable better measurement. Pulse shaping circuits serve two main functions: on one hand, they filter out some of the noise originating from the charge-sensitive amplifier, thereby improving the signal-to-noise ratio; on the other hand, they shape the signal to output a quasi-Gaussian waveform with a relatively flat top, facilitating subsequent circuitry alignment for sampling. The peak of the output quasi-Gaussian waveform is directly proportional to the charge signal collected by the charge-sensitive amplifier. As shown in Figure 3.21, pulse shaping circuits are typically composed of a combination of capacitor-resistor ($C - R$) circuits and resistor-capacitor ($R - C$) circuits. The $C - R$ differentiating circuit can shorten the decay time of the pulse, while the $R - C$ integrating circuit can broaden the rising edge of the pulse. If n $R - C$ integrating circuits are connected in series after a single $C - R$ high-pass filtering circuit, the shape of the output pulse will further approach a Gaussian waveform. The output pulse is given by:

$$V_0(t) \propto \left(\frac{t}{\tau}\right)^n e^{-\frac{t}{\tau}} \quad (3.57)$$

In Equation 3.57, the time constant τ is referred to as the shaping time of the filtering circuit. After a time of $t_p = n\tau$, the signal reaches the peak of the quasi-Gaussian waveform, hence t_p is termed as the peaking time.

3.3.5 Chip IDE1140 - VA

The amplification and shaping of the signals are implemented in Application Specific Integrated Circuit (ASIC) chips, typically designed to optimise the mounting next to the strips, minimise the noise and the power consumption. Both in AMS-L0 and HERD-SCD the used ASIC is the chip IDE1140 [96], also called VA (*Viking Architecture*) after the name of the first ASIC progenitor of the series. Figure 3.22 shows the VA schematic diagram, with each unit connected to 64 channels of the detector. For each channel, the input

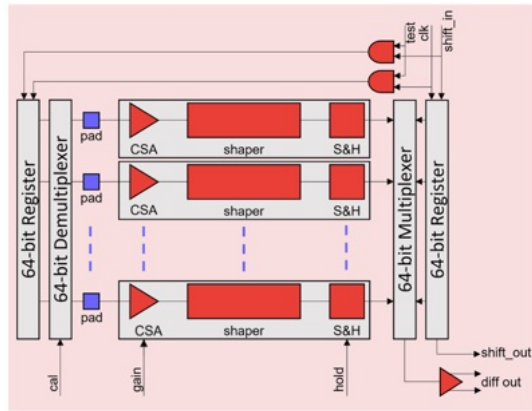


Figure (3.22) – Simple schematic diagram of IDE1140 chip structure [97].

signal proceeds sequentially through a charge-sensitive amplifier (CSA), which provides a signal pulse height proportional to the charge collected by the strip, followed by a 6.5-microsecond $CR - (RC)^n$ shaper. All the channels are sampled at the same moment and the signal held via a Sample & Hold (S&H) module. The power consumption per channel is ~ 0.3 mW for a total of about 20 mW per chip. After the sampling, the output of the S&H is switched via an analog multiplexer to a differential current buffer to drive it out of the die and input to an external Analog to Digital Converter (ADC) for digitisation and readout.

The nominal signal peak time of the IDE1140 chip is $6.5 \mu\text{s}$, but the actual value to be used to optimise the sampling moment can be determined based on experimental data. As example, as shown in Figure 3.23, with data obtained with a pulsed laser on the strips, it has been measured that the best sampling time is about $8 \mu\text{s}$ after the particle has passed through the detector.

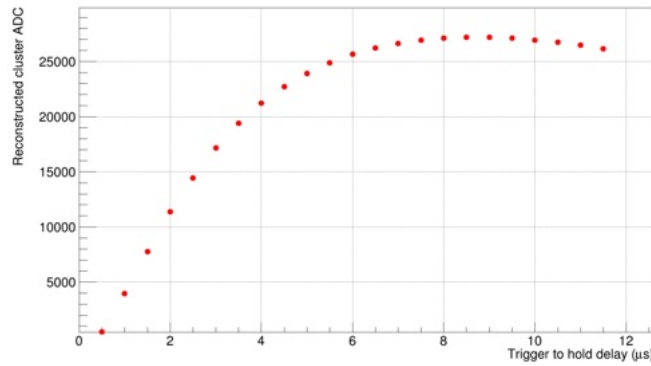


Figure (3.23) – IDE1140 response as a function of delay from trigger to the signal, due to the pulsed laser, sampling [98].

3.4 Signal Analysis

The *raw* data collected in output from the detector must undergo to different procedures in order to measure the physical signal, i.e. the position and charge of a traversing particle. Preliminary to position and charge reconstruction, detector must be *calibrated* to evaluate its response in absence of signal. Then *clusters* of strips corresponding to the crossing of a particle are defined and the particle impact position and charge can be evaluated. In the following we will deal with each step of the signal extraction process.

3.4.1 Calibration

A raw event is defined as the raw content of all the read out strips of the detector. A set of consecutive events is a run. We define a “calibration run” a collection of a minimum of 3000 and up to 10000 events, without external radiation source, to calibrate the sensor’s response.

When no particles pass through the silicon microstrip detector, the ADC measurement values in each channel are generally normally distributed around a value called “pedestal”. The pedestal value is defined by the electric characteristics of the silicon sensor itself, of the read-out ASIC and its value is typically drifting as a function of the temperature. Since the temperature drift is of the order of fraction of ADC counts per $^{\circ}\text{C}$, is safe to consider the pedestal as constant and as a “fingerprint” of the module created by the combination of a particular silicon sensor with a particular read-out ASIC: one of the goal of the calibration procedure is to measure the pedestal value for

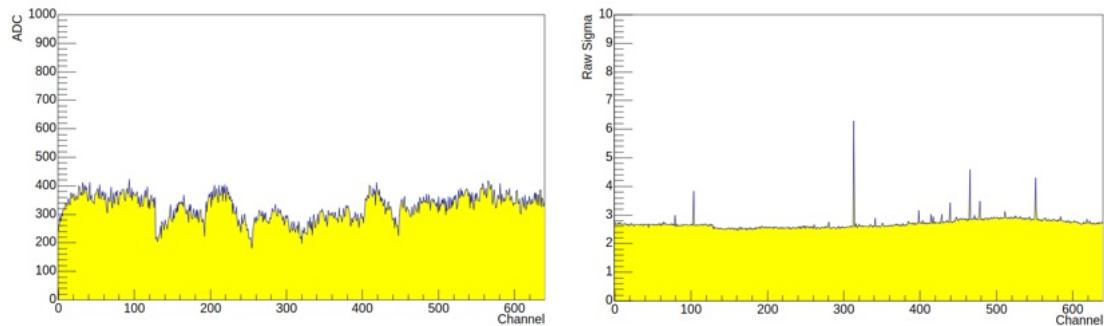


Figure (3.24) – Pedestal (left) and raw sigma (right) values, in ADC counts, as a function of the readout channel, derived from a calibration run of the SCD prototype sensor 05, from the 2023 HERD beam test.

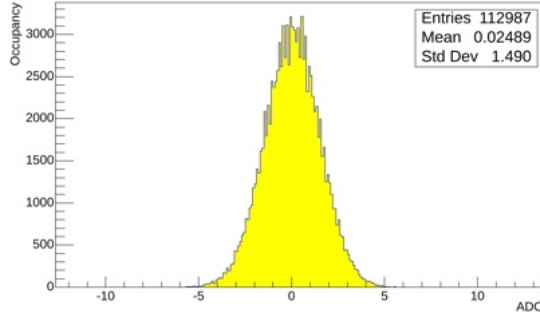


Figure (3.25) – Common Noise Distribution, in ADC counts, of one full sensor (SCD prototype sensor 06, from the 2023 HERD beam test).

each channel. If, with a random trigger and in absence of crossing particles, N readings of the output voltage of the j -th channel are taken, it is possible to estimate the value of its pedestal PED^j according to:

$$PED^j = \sum_i^N \frac{ADC_i^j}{N} \quad (3.58)$$

where ADC_i^j is the output voltage of the j -th channel read in the i -th event, expressed in ADC counts.

For each channel, j , the typical fluctuation of the read-out value can be estimated by the standard deviation of the ADC_i^j value, around the pedestal value, PED^j , after N readings and can be computed as:

$$\sigma_{raw}^j = \sqrt{\sum_i^N \frac{(ADC_i^j - PED^j)^2}{N}} \quad (3.59)$$

and σ_{raw}^j can be considered as composed of the following two contributions:

1. the common mode noise (CN), that is, a time-varying signal level common to a set of strips due to their interconnections at the same circuit. For example, offset common to all 64 reading channels belonging to the same preamplifier chip IDE1140 (VA), offset common to all reading channels belonging to the same ADC, or the same sensor;
2. the incoherent noise, determined by the electrical properties of individual strips, such as the level of leakage currents or the quality of the connections between the sensor and the readout electronics.

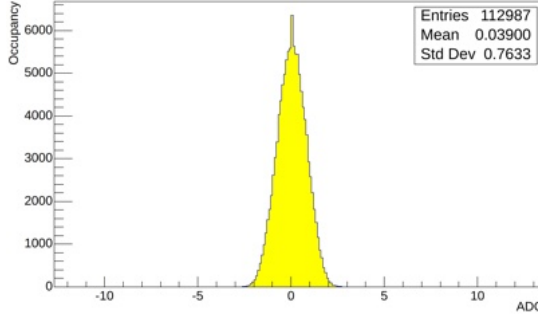


Figure (3.26) – Common Noise Distribution , in ADC counts, of one single ADC (first ADC of the SCD prototype sensor 06, from the 2023 beam test).

The presence of common mode noise is affecting the read out signal as an event by event random fluctuation, typically distributed as gaussian around zero. The offset for the k -th integrated circuit component (VA, ADC, sensor) at the i -th event can be computed as:

$$CN_i^k = \sum_j^n \frac{ADC_i^j - PED^j}{n} \quad (3.60)$$

The expression above, with n the number of readout strips connected to the same integrated circuit component, is a effective way to compute, on event by event basis, the fluctuation due to the common mode noise. Unfortunately there are some conditions that can artificially bias the estimation: the presence, even if in only few channels, of the additional signal due to the, accidental, passage of a real particle and the presence of channels out of the nominal functioning (very low signals, i.e. “dead”, and very large signals, i.e. “noisy”). The former is corrected by considering only channels that have a

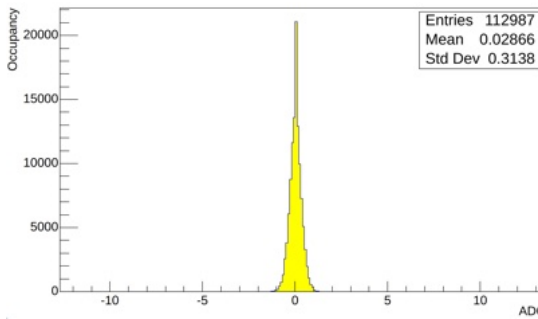


Figure (3.27) – Common noise distribution, in ADC counts, of one single VA (first VA of the SCD prototype sensor 06, from the 2023 beam test).

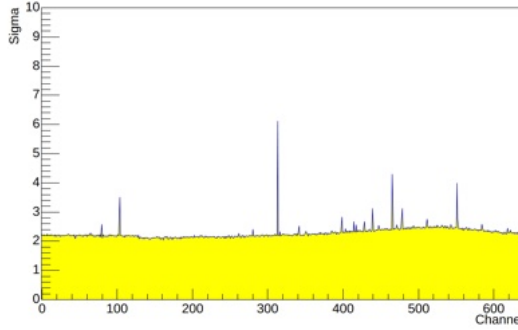


Figure (3.28) – Value of the sigma, in ADC counts, as a function of the readout channel, derived from a calibration run of the SCD prototype sensor 05, from the 2023 HERD beam test.

signal below a specific threshold ($|ADC_i^j - PED^j| < 3.5\sigma_{raw}^j$, where the absolute value is used in the different to avoid a potential bias coming from a cut that is asymmetrical with respect to zero. This relies on the assumption that the typical fluctuation due to common mode noise is smaller than the one due the incoherent, per channel, noise. A common mode noise larger or comparable to the incoherent noise could bias an estimate performed using a simple average algorithm. In addition to this, if during calculations there are noisy or dead strips and this are not removed from the average computation, it will result in inaccurate outcomes. The solution to overcome the risk of bias in the mean computation is to use an estimate much more robust to outliers, as the median. During the work related to this thesis, the median method to calculate CN was employed exclusively. Since averaging over a certain number of channels allows to measure the CN, this gives the possibility to subtract it on event by event basis. This will be possible, again on event by event basis, also for the events collected in presence of particles passing through, i.e. during an actual data taking. For an efficient and more accurate evaluation of the signal, seen by each channel, due to the passage of a particles is better to compare the total signal read out by a channel not with the sum of the common mode noise and of incoherent noise, i.e. σ_{raw}^j , but only with the latter. The incoherent noise of a single strip, σ^j , is defined as the standard deviation of the distribution of its voltage around the pedestal value, once the common mode offset has been subtracted.

For the j -th strip, using N events, when no particles are passing through, we obtain:

$$\sigma^j = \sqrt{\sum_{i=1}^N \frac{(ADC_i^j - PED^j - \sum CN_i^k)^2}{N}} \quad (3.61)$$

where, for the CN, there's a sum over the different common mode noises identified (sensor, ADC or VA), the index k refers to the “element” (again sensor, ADC or VA) where the j -th strips belong to. Effectively, in absence of a significative number of dead/noisy channels in the VAs, calculation of the events by CN at the VA level is faster and sufficient.

3.4.2 Cluster search

Once the calibration is done, when particles pass through, it is possible to evaluate, event by event, the absolute voltage level at the output of the j -th channel as follows, only due to the particle energy deposition, as:

$$S_i^j = ADC_i^j - PED^j - \sum CN_i^k \quad (3.62)$$

The significance of the signal defined as above is generally compared to the expected incoherent noise level for the channel under examination, defining the signal-to-noise ratio (S/N) for the individual j -th channel in i -th event as:

$$\left(\frac{S}{N}\right)_i^j = \frac{S_i^j}{\sigma^j} \quad (3.63)$$

This ratio is used in the “cluster identification” process. The “cluster” is defined as a collection of strips with signal magnitudes exceeding a certain threshold near the particle hit position, as shown in Figure 3.29.

The cluster identification is a two step process, repeated until all the channels of a sensor are scanned. In a first step, the signal S_i^j of each channel is compared to its σ_j , requiring $S_i^j \geq H\sigma^j$ to possibly identify a signal level due to a particle. H is the High threshold, ranging from 3.5 to 5, required to trigger the clusterization process. The strip with the highest signal satisfying the high threshold condition will be the *seed* of the cluster and will be used as the center to look for neighbouring strips that have potentially shared the charge from particle ionization. In order to be selected for clusterization, neighbouring strips should have a signal $S_i^j \geq L\sigma^j$, with L typically close to unity. The above process is then repeated scanning all the strips not already included in a previous cluster. The actual values of H and L depend on the detector performance (typical S/N figure of merit), the need of early suppression of readings from uninteresting channels (i.e. data reduction before transfer from space to ground segment) and on the conditions required for specific analyses.

In this thesis, a $H = 5$ and $L = 1$ values have been generally used, with some exceptions to maximize efficiency, position resolution or charge identification in specific

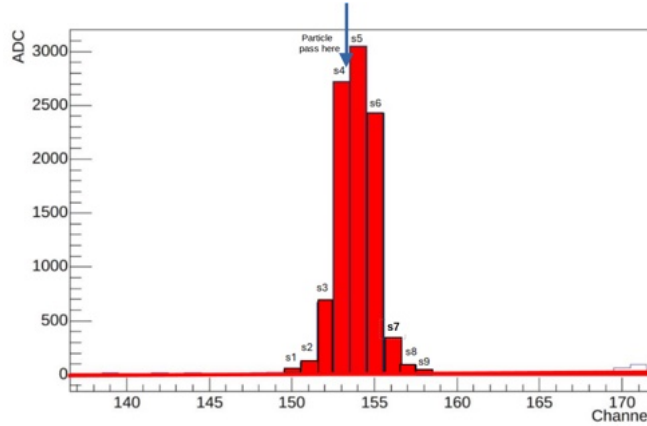


Figure (3.29) – The signal, after pedestal and common mode noise subtraction, of the readout channels (zoom from channel ~ 135 to channel ~ 175) of one sensor when a particle passes through. Channels from ~ 150 to ~ 158 are clearly affected by the passage of a particle and their read out value is clearly different from zero. The blue arrow points to an estimation of the passage point of the particle (i.e. between channel 153 and channel 154).

studies.

The sum of the signals from all readout strips in a cluster is referred to as the cluster integral or cluster charge, defined as follows:

$$I = \sum_{j_1}^{j_n} S_i^j \quad (3.64)$$

In the above equation, S_i^j is defined by Equation 3.62 and j_1 and j_n are the first and last readout strips in the cluster. The magnitude of the cluster integral is proportional to the energy deposited when a particle passes through the detector layer. For a given silicon microstrip detector, according to the Bethe-Bloch formula, the deposited energy depends only on the charge and velocity of the incident particle. Therefore, once the velocity is determined, the charge carried by the particle can be inferred by measuring the energy deposited in the detector.

In addition to measuring the charge carried by the passing particle, the main function of a silicon microstrip detector is to reconstruct the particle's impact point and, in the case of a tracker made by multiple layers, its trajectory. A raw estimate of the particles impact point, referred as *hit* in the following, can be provided by the channel, within a cluster, with the highest signal or by the mid-point between the two highest ones. But a more precise hit position can be obtained by calculating the Center Of Gravity (*COG*) of the cluster, still using only the two channels with the highest signal, by using the

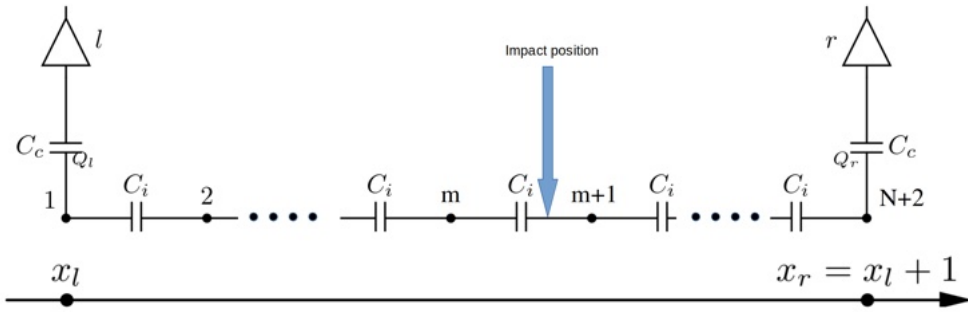


Figure (3.30) – Simple model of capacitive coupling with N intermediate strips

following formula:

$$COG = \frac{S_l x_l + S_r x_r}{S_l + S_r} = \frac{S_l x_l + S_r (x_l + 1)}{S_{tot}} = x_l + \frac{S_r}{S_{tot}} = x_l + \frac{Q_r}{Q_{tot}} \quad (3.65)$$

In the above formula, S_l and S_r represent the left and right highest signals channels and so, logically, the signals from the readout strips on the left and right sides of the particle impact point in the cluster. Since the signal is proportional to the charge collected by the readout strips, S_l and S_r can also be replaced by Q_l and Q_r , which represent the charge collected by these two readout strips. The measured charge value are used as weights that multiply x_l and x_r , the position of the two strips expressed in readout pitch units. Because the readout strips closer to the impact point have stronger signals, these two strips in the cluster have a higher signal-to-noise ratio compared to other readout strips. Therefore, they can more accurately indicate the actual impact position of the particle. The principle of Eq. 3.65 can be explained through a simple model that includes also the floating strips not read out by the ASIC.

As shown in Fig. 3.30, let's assume there are N intermediate strips with an implant pitch of p (in readout pitch units). The amount of signal read out by the front end electronics will depend on all the capacitances, as discussed later for now let's concentrate only on two: C_i represents the interstrip capacitance, while C_c represents the capacitance to the electronics. Since C_c is much larger than C_i , once the signal (i.e. the current generated by the energy deposit and flowing to the electronics) is close to the read out channels, almost no charge is transmitted to the additional second neighbouring readout strips (not drawn in Fig. 3.30, but on the very left and very right edges of the sketch). Ignoring the coupling to the backplane, the charge released by the traversing particle will be shared only between the intermediate strips m and $m + 1$,

which are on the left and right sides of the particle impact point, respectively. Therefore:

$$Q_{tot} = Q_m + Q_{m+1} \quad (3.66)$$

We assume that x is the particle impact point, and the ratio of Q_m and Q_{m+1} is a function² of x , then:

$$\alpha(x) = \frac{Q_{m+1}(x)}{Q_{tot}} \quad (3.67)$$

The charge collected by the intermediate strips m and $m+1$ induces charges $(Q_{m,l}, Q_{m+1,l})$ on the left readout strip, and also $(Q_{m,r}, Q_{m+1,r})$ on the right readout strip. The charge induced by a given intermediate strip, im , on a certain read out one, ro , will depend exclusively (if, again, we neglect, for now, the capacitance to the backplane) on the capacitance, C , between the intermediate and the read out:

$$Q_{ro} \propto C Q_{im} \quad (3.68)$$

Considering the two read out strips, one on the left, rol , and one on the right, ror , with their respective capacitances to the intermediate in the middle, C_l and C_r , is trivial to demonstrate that:

$$Q_{rol} = \frac{C_l}{C_{tot}} Q_{im} ; \quad Q_{ror} = \frac{C_r}{C_{tot}} Q_{im} \quad (3.69)$$

and thus

$$\frac{Q_{rol}}{C_l} = \frac{Q_{ror}}{C_r} \quad (3.70)$$

so independently from the charge on the intermediate itself and on the total capacitance (that could, for example, include also a contribution towards another electrode, e.g. the backplane, that collects part of the shared charge).

Therefore, the charge collected on the left and right readout strips (Q_l, Q_r) is the sum of the contributions from intermediate strips m and $m+1$:

$$Q_l = Q_{m,l} + Q_{m+1,l} \quad (3.71)$$

$$Q_r = Q_{m,r} + Q_{m+1,r} \quad (3.72)$$

Using the relation in Eq. 3.70:

$$\frac{Q_{j,l}}{C_{j,l}} = \frac{Q_{j,r}}{C_{j,r}} \text{ with } j=m, m+1 \quad (3.73)$$

²is easy to show as, for the Shockley-Ramo's theorem, for a particle entering, close to one strip, on one side and exiting on the other side, always close to that strip (i.e. "vertical"), the charge must be collected only by the closest strip. But for a particle passing in the middle between two strips and not vertical but with a certain angle, there's a "charge sharing" between the two intermediate strips. Also the diffusion of the charge, around the average drift path, contributes to this sharing. See later.

where $C_{j,l}$ and $C_{j,r}$ correspond to the equivalent capacitance between the intermediate strip j and the left (right) readout strip, respectively. We get:

$$Q_{j,r} = Q_j \cdot \left(1 + \frac{C_{j,l}}{C_{j,r}}\right)^{-1} \text{ with } j=m, m+1 \quad (3.74)$$

In the above formula, the couplings $C_{j,l}$ and $C_{j,r}$ can be expressed as:

$$C_{j,l} = \frac{C_i}{j-1} \quad (3.75)$$

$$C_{j,r} = \frac{C_i}{N+2-j} \quad (3.76)$$

Leading to an expression for the center of gravity 3.65 as:

$$COG = x_l + \frac{1}{Q} \cdot \sum_{j=m}^{m+1} Q_j \left(1 + \frac{C_{j,l}}{C_{j,r}}\right)^{-1} \quad (3.77)$$

$$= x_l + \frac{1}{Q \cdot (N+1)} \sum_{j=m}^{m+1} Q_j (j-1) \quad (3.78)$$

$$= x_l + \frac{m-1+\alpha(x)}{N+1} \quad (3.79)$$

As $x_m = x_l + p(m-1)$, and $p \cdot (N+1) = 1$,

$$COG = x_m + p \cdot \alpha(x) \quad (3.80)$$

In the above formula, x_m is the position of the intermediate strip m , and p is the implant pitch, that is the distance between the two intermediate stripes, in readout pitch units. Therefore, whether the COG can accurately represent the particle impact point and depends entirely on the $\alpha(x)$ function. Now let's look at the specific expression of the $\alpha(x)$ function.

As shown in Figure 3.31, we assume that a “vertical” particle impacts the detector between the two intermediate strips at position x , and it releases, thanks to diffusion and multiple scattering inside the material, a charge tube with a width of δ . According to the distribution of electric field lines within the depletion region and the Shockley-Ramo’s theorem, the charge carriers located at a position $x < x_m + p/2$ will accumulate on strip m , else they will be collected by strip x_{m+1} . Therefore, $\alpha(x)$ can be expressed as the following piecewise function.

$$\alpha(x) = \begin{cases} 1 & \text{if } x > x_m + \frac{1}{2}(p + \delta) \\ \frac{1}{\delta}(x - x_m) + \frac{1}{2\delta}(\delta - p) & \text{if } x \in [x_m + \frac{1}{2}(p - \delta) : x_m + \frac{1}{2}(p + \delta)] \\ 0 & \text{if } x < x_m + \frac{1}{2}(p - \delta) \end{cases} \quad (3.81)$$

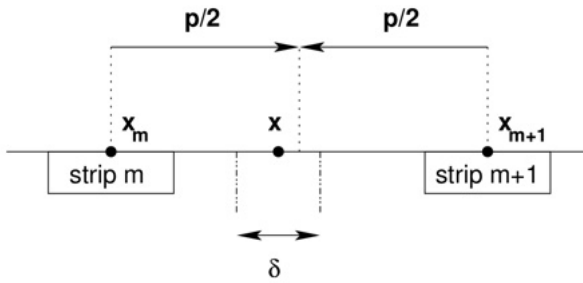


Figure (3.31) – Simple model of charge sharing, x is particle impact position.

And the center of gravity expression 3.80 becomes:

$$COG = \begin{cases} x_{m+1} & \text{if } x > x_m + \frac{1}{2}(p + \delta) \\ x_m + \frac{p}{\delta}(x - x_m) + \frac{p}{2\delta}(\delta - p) & \text{if } x \in [x_m + \frac{1}{2}(p - \delta) : x_m + \frac{1}{2}(p + \delta)] \\ x_m & \text{if } x < x_m + \frac{1}{2}(p - \delta) \end{cases} \quad (3.82)$$

By observing formula 3.82, it can be found that when $\delta = p$, the center of gravity calculated corresponds completely to the impact position. Figure 3.32 shows the different correspondence between the impact coordinate x and the center of gravity calculated for a detector with 3 intermediate strips when the ratio of δ to p varies. From the figure, it can be seen that as p gradually increases relatively to δ , the relation between the center of gravity and the impact position is not anymore linear, i.e. the reconstructed center of gravity tends to “accumulate” to the strip positions.

Typically, the thickness of a silicon microstrip detector is of few hundreds of microns, and the diffusion process spreads the released charges to a width of approximately 10-20 microns. To achieve the best spatial resolution, the implant pitch needs to be of the same order of magnitude. In principle, without increasing the number of readout strips, we can always reduce the implant pitch to the desired magnitude by increasing the number of intermediate strips. However, it is important to note that all the above discussions are based on a simplified model where we only considered the coupling between strips and ignored the coupling between the strips and the backplane, and thus did not account for charge loss. In practice, although increasing the number of intermediate strips can improve spatial resolution, it also reduces the charge collection efficiency (more charge reaches the backplane), making the signals generated when particles pass through the detector more susceptible to being drowned out by noise, which can, in turn, degrade spatial resolution. In addition, since the amount of charge collected to the backplane

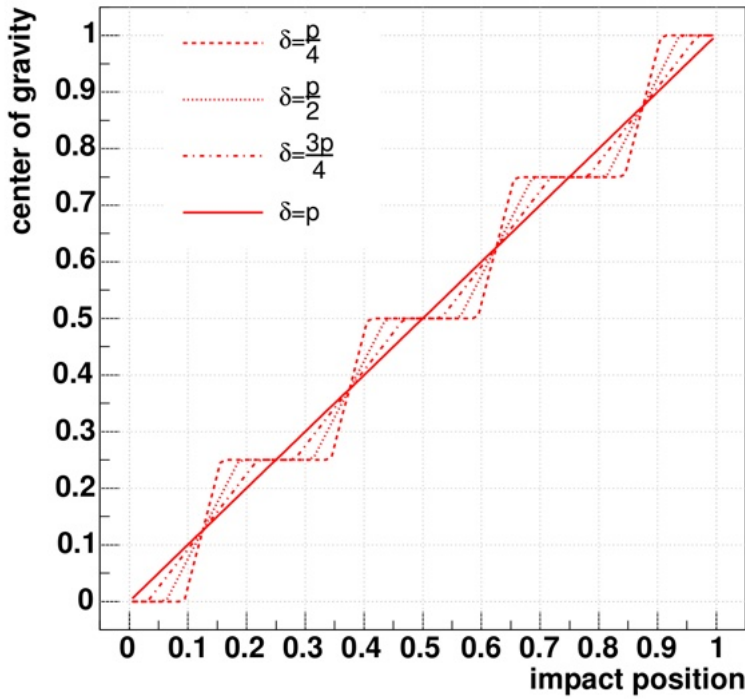


Figure (3.32) – Correspondence between the impact coordinate x and the center of gravity calculated for a detector with 3 intermediate strips, for different sensor layout.

is also depending on the distance (i.e. the capacitance) between the intermediate strip and the read out one, with respect to the capacitance between the intermediate strips and the backplane, the total collected charge will also have a dependence on the actual impact point, and this is of particular importance when using the sensor to measure the Z of the impinging particle. For a better explanation, the following will discuss two different scenarios as examples: one intermediate strip, and three intermediate strips.

1: one intermediate strip

In Figure 3.33, a particle that perpendicularly strikes an intermediate strip of the detector, generating a total charge of Q . A fraction of this charge is coupled to the neighbouring strips on the left and right, denoted as Q_{int_L} and Q_{int_R} , respectively, while another fraction is coupled to the backplane, denoted as Q_b . Thus, the total charge Q can be expressed as:

$$Q = Q_{int_L} + Q_b + Q_{int_R} \quad (3.83)$$

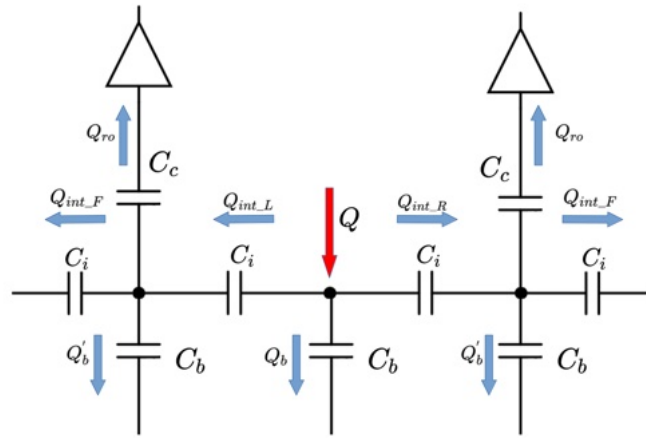


Figure (3.33) – Equivalent circuit of the system of two read out strips and one intermediate one.

$$= \frac{QC_i}{C_b + 2C_i} + \frac{QC_b}{C_b + 2C_i} + \frac{QC_i}{C_b + 2C_i} \quad (3.84)$$

The charges Q_{int_L} and Q_{int_R} , coupled to the adjacent strips on both sides, are similarly distributed across the electronic output capacitance C_c , the interstrip capacitance C_i , and the backplane capacitance C_b . Taking Q_{int_L} as an example (Q_{int_L} and Q_{int_R} are the same, due to symmetry):

$$Q_{int_L} = Q_{int_F} + Q_b + Q_{ro} \quad (3.85)$$

$$= \frac{Q_{int_L}C_{int_F}}{C_{int_F} + C_b + C_c} + \frac{Q_{int_L}C_b}{C_{int_F} + C_b + C_c} + \frac{Q_{int_L}C_c}{C_{int_F} + C_b + C_c} \quad (3.86)$$

In the above equation, C_{int_F} represents the equivalent capacitance when the charge is coupled to the far end on the left side. For convenience in calculation, it is assumed that the relationship between the backplane capacitance C_b and the interstrip capacitance C_i is as follows:

$$C_b = kC_i \quad (3.87)$$

Generally³, k is less than 1, and C_c is much greater than C_b and C_{int_F} . The actual charge Q_{ro} coupled to the left capacitance C_c and read out is:

$$Q_{ro} = Q_{int_L} \cdot \frac{C_c}{C_{int_F} + C_b + C_c} \quad (3.88)$$

$$= Q \cdot \frac{C_i}{C_b + 2C_i} \cdot \frac{C_c}{C_{int_F} + C_b + C_c} \quad (3.89)$$

³when the detector thickness is significantly greater than the implant pitch

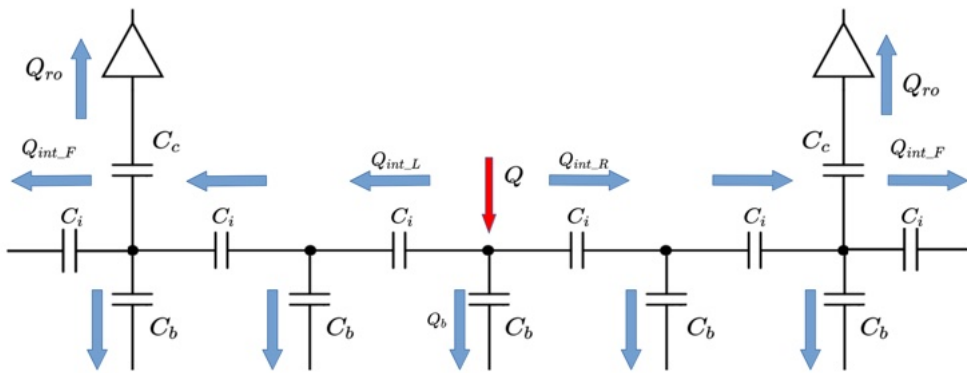


Figure (3.34) – Equivalent circuit of the system of two read out strips and three intermediate ones.

$$\approx \frac{Q}{k+2} \quad (3.90)$$

Thus, the total charge collection efficiency (CCE) is:

$$CCE_{one} = \frac{2Q_{ro}}{Q} = \frac{2}{k+2} < 1 \quad (3.91)$$

From formula 3.91, it can be seen that the backplane capacitance C_b causes the charge collection efficiency to be less than 1, and the larger the backplane capacitance C_b with respect to the interstrip capacitance C_i , the lower the collection efficiency.

2: three intermediate strips

Figure 3.34 is the equivalent circuit diagram of a silicon microstrip detector with three intermediate strips. For ease of comparison, compared to Figure 3.33, in Figure 3.34 the readout strip pitch and the particle impact position remain unchanged.

Similar to the previous discussion, but in this case the actual charge Q_{ro} coupled to one side readout strip through capacitance C_c is⁴:

$$Q_{ro} = Q \cdot \frac{(C_i + C_b) \parallel C_i}{2((C_i + C_b) \parallel C_i) + C_b} \cdot \frac{C_i}{C_b + C_i} \cdot \frac{C_{ro}}{C_{ro} + C_{int_F} + C_b} \quad (3.92)$$

By substituting formula 3.87 into the above formula, the charge collection efficiency can be calculated as:

$$CCE_{three} = \frac{2Q_{ro}}{Q} \approx \frac{2}{k^2 + 4k + 2} \quad (3.93)$$

⁴the symbol \parallel denotes, when referred to capacitances, the series value of the capacitances before and after the symbol.

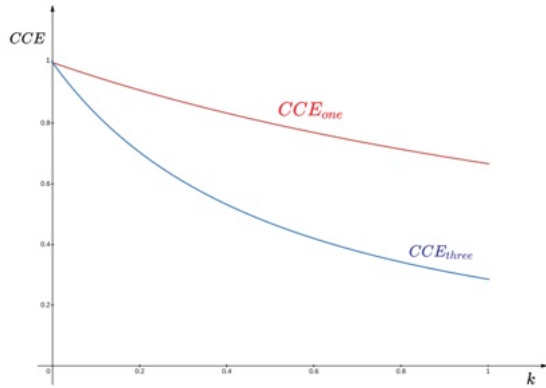


Figure (3.35) – Comparison chart of the charge collection efficiency of one middle strip versus three middle strips, as a function of the k value.

It is clearly evident that the charge collection efficiency with three middle strips is significantly lower than that with only one middle strip.

Figure 3.35 is the comparison chart of the charge collection efficiencies at different k values. From the figure, it can be seen that as k increases, the difference in charge collection efficiency also increases.

Typically, the charge collection efficiency is not only related to the number of intermediate strips but also to the specific position of the particle impact point relative to the readout strip. For example, in Figure 3.36, the particle impact point from Figure 3.34 is moved from the central position to a location closer to the left readout strip.

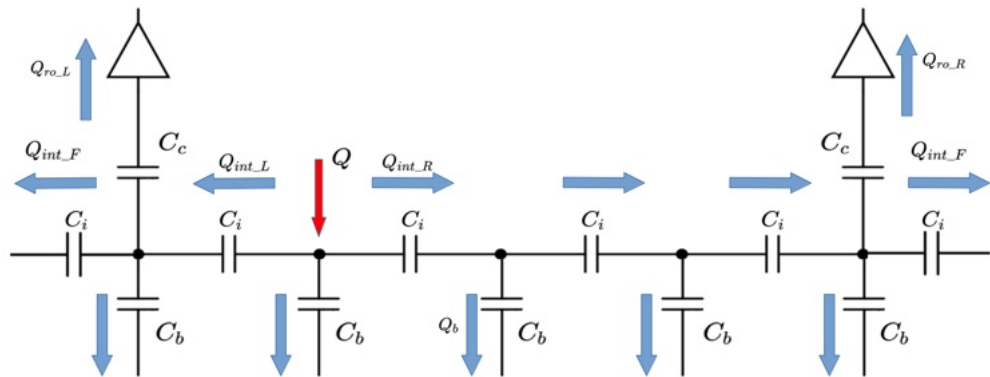


Figure (3.36) – Same as Fig. 3.34 but with the particle impact point is moved from the central position to a location closer to the left readout strip.

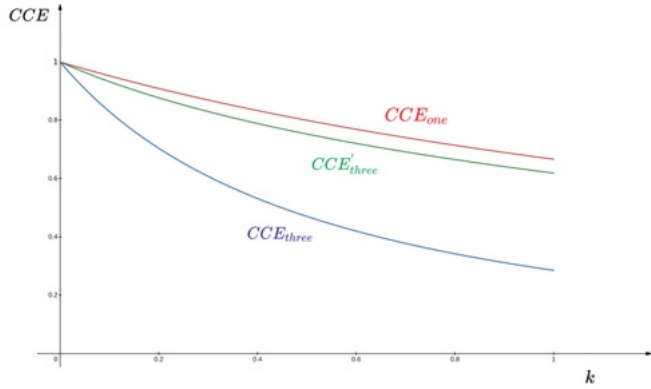


Figure (3.37) – Comparison chart of CCE_{one} , CCE_{three} and CCE'_{three} , as a function of the k value.

At this point, the charge collected by the readout strip on the left side of the particle impact point is:

$$Q_{ro_L} = Q \cdot \frac{C_i}{C_i + C_b + C_{eq_R}} \cdot \frac{C_c}{C_c + C_{int_F} + C_b} \quad (3.94)$$

The charge collected by the readout strip on the right side of the particle impact point is:

$$Q_{ro_R} = Q \cdot \frac{C_{eq_R}}{C_i + C_b + C_{eq_R}} \cdot \frac{C_c}{C_c + C_{int_F} + C_b} \quad (3.95)$$

In the above equation, C_{eq_R} is the equivalent capacitance on the right side of the particle impact point:

$$C_{eq_R} \approx ((C_i + C_b) \parallel C_i + C_b) \parallel C_i \quad (3.96)$$

By substituting Equation 3.87 into Equations 3.94 and 3.95 above, the new charge collection efficiency can be calculated as:

$$CCE'_{three} = \frac{Q_{ro_L}}{Q} + \frac{Q_{ro_R}}{Q} \quad (3.97)$$

$$\approx \frac{k^2 + 4k + 3}{k^3 + 6k^2 + 10k + 4} + \frac{k^2 + 3k + 1}{k^3 + 6k^2 + 10k + 4} \quad (3.98)$$

$$\approx \frac{2k^2 + 7k + 4}{k^3 + 6k^2 + 10k + 4} \quad (3.99)$$

Figure 3.37 is the comparison chart of CCE_{one} , CCE_{three} and CCE'_{three} at different k values. From the figure, it is clearly evident that because the impact point has moved closer to a specific readout strip, it now has a different (higher) charge collection efficiency compared to the previous position.

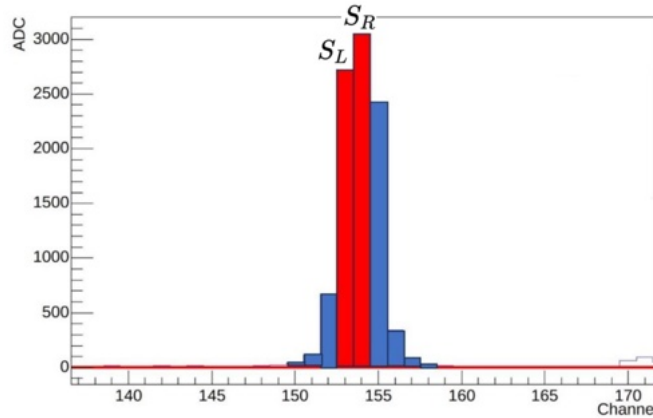


Figure (3.38) – Example of cluster to show the position of S_L and S_R .

In the actual use of silicon microstrip detectors, the impact points of particles are random. This phenomenon, where different charge collection efficiencies occur due to varying positions relative to the readout strip, can lead to inaccuracies in measuring the deposited energy of particles passing through the detector, thereby affecting the measurement of the charge carried by the particles. Therefore, a method is needed to correct the charge collection efficiency at different positions. The next section will discuss the methods for this correction.

3.4.3 η correction

From the previous discussion, it can be seen that the charge collection efficiency depends only on the relative position of the particle impact point to the adjacent readout strips. Therefore, using the cluster center of gravity to describe positions with different charge collection efficiencies is not convenient. To facilitate the study, the concept of η (eta) can be introduced, defined as follows:

$$\eta = \frac{S_R}{S_R + S_L} \quad (3.100)$$

As shown in Figure 3.38, let's define, as conventional direction for the increasing readout strip numbers in a silicon microstrip sensor, the one from left to right. Therefore, in Eq. 3.100, S_L and S_R represent the signal values of the left and right readout strips, respectively, which have the strongest signals in the cluster and are the closest to the particle impact point.

The value of η ranges from zero to one. Neglecting the possible saturation effect, in the electronics, when the collected signal is too high and also the fact that, given a

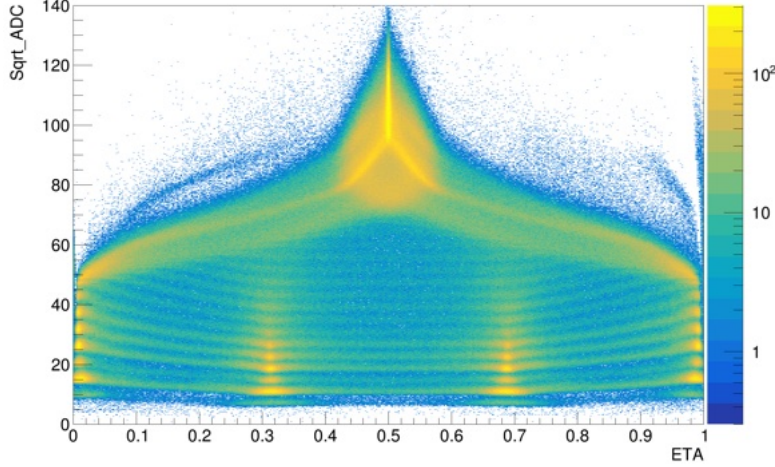


Figure (3.39) – Square root of the total collected signal as a function of η . Data from the HERD prototype beam test in 2023.

cluster finding algorithm as the one discussed in Sec. 3.4.2, is not possible to have S_L or S_R below a certain threshold, η has a one-to-one correspondence with the position of the particle impact point relative to its adjacent readout strips. This means any relative position of the particle impact point can be represented by a η number between zero and one. For any given cluster, the particle impact position is unique, and thus, its η value is also unique. Similar to the previously mentioned "cluster integral" η can be also regarded as a characteristic quantity of the cluster and used for cluster classification.

Figure 3.39 is a two-dimensional plot of the "cluster integral" as a function of eta. In this plot, the horizontal axis represents eta, while the vertical axis represents the square root of the total collected signal in units of ADC. The square root is used because the cluster integral corresponds to the energy deposited by a particle passing through the detector, and according to the Bethe-Bloch formula, the deposited energy is proportional to the square of the charge Z carried by the particle. Using the square root, ideally, the values on the y axis of Fig. 3.39 are linearly proportional to the charge of the particle.

This plot categorizes clusters based on the two features: cluster integral and eta. Each bin in the plot corresponds to a unique pair of eta and cluster integral values, and the color of each bin indicates the number of clusters that fall into that bin. The brighter the color, the more clusters are present in that bin.

Upon observation, it can be seen that bright bins form several almost horizontal curves, often referred to as "charge lines". These curves appear because the deposited energy by high-energy (i.e. ultra-relativistic) particles with the same charge follows a

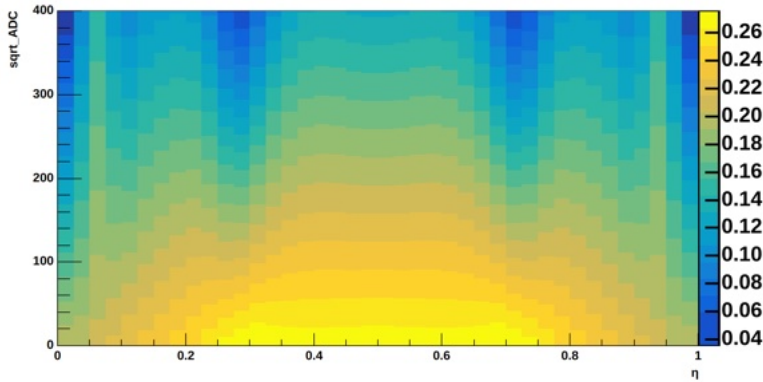


Figure (3.40) – Conversion map used to pass from a doublet, ($S_L + S_R = S_{tot}, \eta$), to the Z of the crossing particles, by using the z axis, Z/S_{tot} .

Landau distribution (approximated by a Gaussian distribution for thicker detectors), and these bright curves correspond to the peak deposited energy of particles with different charges, with the dependence by the Z of the particle being particularly clear.

Examining the direction of these charge lines, it is apparent that they are symmetrically centered around an eta value of 0.5 and gradually bend downward near the center. This downward bending is a visual representation of the charge collection efficiency varying with the eta value, as discussed in the previous section. The areas where the curves bend downward the most, indicate lower charge collection efficiencies, meaning more charge is lost to the backplane and not read out.

Figure 3.39 provides us a map for identifying the charge carried by particles passing through the detector: in principle, if we know the cluster integral and eta corresponding to a passing particle, we can find its position on this plot. Then, the nearest charge line determines the actual charge carried by the particle.

The above process is called “ η correction”. Figure 3.39, not easily determined from first principles. must be used as reference to asses the correct input charge.

In Figure 3.40, differently from Figure 3.39, the z coordinate represents the value of “charge/cluster integral” (Z/S_{tot}). A distribution like the one in Fig. 3.40 acts similarly to a “conversion map”, when the cluster integral and the η value of the clusters generated as the particle passes through are known. The corresponding Z/S_{tot} value can be retrieved and, by multiplying this value by the cluster integral, the actual charge carried by the passing particle can be determined. The Z/S_{tot} value for each bin in Figure 3.40 needs to be calibrated through the map as in Fig. 3.39. This step is quite easy and effective, since

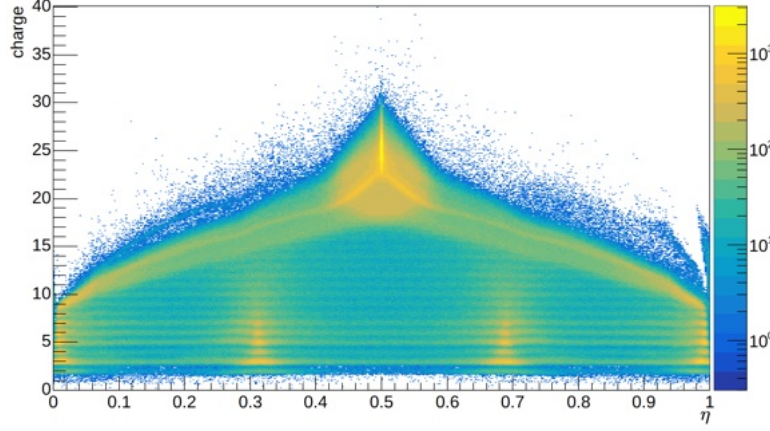


Figure (3.41) – Estimated particle charge as a function of η , as in Fig. 3.39, after η correction. Data from the HERD prototype beam test in 2023.

for each certain η value, the Z/S_{tot} value is a linear function of S_{tot} :

$$\frac{Z}{S_{tot}} = a_i \cdot S_{tot} + b_i \quad (3.101)$$

Therefore, by obtaining the coefficients a_i and b_i through linear fitting, the Z/S_{tot} values for all bins corresponding to the same η value can be calculated. In the above equation, i represents the index of the bin on the η coordinate axis. Figure 3.41 shows the charge versus η , plot after the η correction. As can be seen from this figure, the charge line becomes flat, which means that after correction, the measured charge of the particle is no longer dependent on η .

This η correction only works when the saturation effect of the readout strips has not occurred. For example, by observing Fig. 3.39 it is clear that in the high signal region where the η value is close to 0 (1), the earliest occurrence of symmetric bending towards the center is seen. Due to the high charge carried by the particle, the resulting high deposited energy signal causes the closer left (right) readout strip to saturate (the closer the distance to the readout strip, the lower the deposited energy required for saturation). At this point, due to the saturation effect, the η value calculated from the readout signals of the strips is incorrect, and the readout signals cannot perfectly reflect the amount of deposited energy. Therefore, it is not possible to determine the true charge carried by the particle, even after η correction.

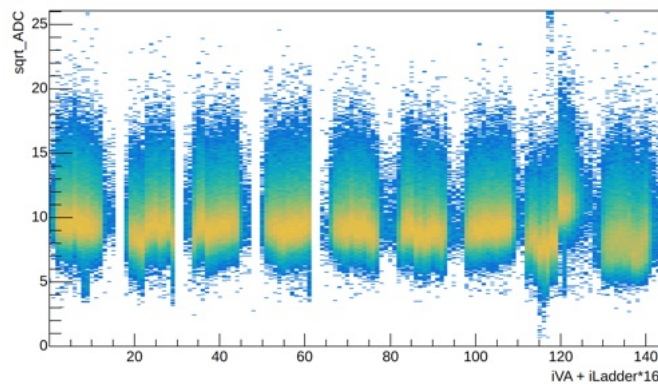


Figure (3.42) – Cluster total collected signal as a function of the VA index. Data from the AMS02-L0 prototype beam test in 2023.

3.4.4 VA equalization

In addition to η correction, the VA (IDE1140) correction is also very important. As mentioned earlier, a VA has 64 channels and can amplify and shape the signals from 64 readout strips of a silicon microstrip detector. Since a silicon microstrip detector typically has a large number of readout strips, multiple VAs are required to read all the strips simultaneously. Measurements have shown that there are slight differences in signal response between different VAs, which can lead to inaccuracies in calculating the charge carried by particles from the readout signals. In Figure 3.42 the vertical axis represents the cluster integral, which is related to the deposited energy of the particles, while the horizontal axis represents the indices of all the VAs used. The silicon microstrip tracker (AMS02-L0 prototype beam test 2023) of this example has nine layers, each with 1024 channels, requiring a total of 144 VAs. This detector measures particles with the same charge ($Z = 1$), but as clearly visible, the signal peak values measured by different VAs differ, due to variations in their response.

The process for the VA correction is as follows: when measuring particles with the same charge, any VA response to the signal is selected as a reference. The ratio of the signal peak measured by this VA to the signal peaks measured by all the other VAs (the ratio for this VA with itself is 1) is evaluated.. Then these ratios are used as calibration factors and multiplied to the signals measured by the corresponding VAs.

Figure 3.43 shows the signal versus the VA, plot after calibration. The figure demonstrates as, after calibration, the signal peak values measured by all VAs are at the same level. This process is often referred as “VA equalization” or “gain equalization”.

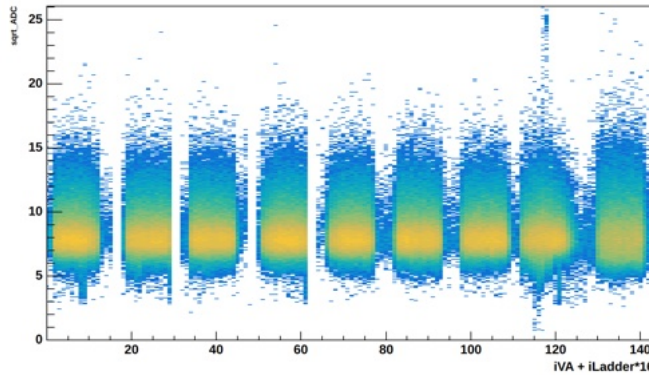


Figure (3.43) – Cluster total collected signal as a function of the VA index, after gain correction. Data from the AMS02-L0 prototype beam test in 2023.

Since the equalization is done via a multiplicative factor, to be applied to each VA response, this correction is belonging to a general family of corrections of the form:

$$S_{corr} = a + bS_{orig} \quad (3.102)$$

and the above depicted correction is only acting on the parameter b . The parameter a is essentially the output level seen by the ADC when the input charge is null (i.e. no signal from the silicon): the a parameter, so, is already equalized during the calibration procedure described above.

3.4.5 Alignment

An important function of silicon microstrip detectors is to measure the one-dimensional coordinates of particles hitting the detector plane through the microstrip structure. And by using multiple layers of silicon microstrip detectors, alternately placed orthogonally, the trajectory of particles in three-dimensional space can be reconstructed.

The accuracy of particle trajectory reconstruction depends not only on the performance of the detector itself but also on the relative “alignment” between the detector layers. Alignment essentially refers to correct knowledge of the position and orientation of each layer of a silicon microstrip tracker within the global coordinate system. If each detector layer position is described using a local coordinate system with the origin at the geometric center of the detector and the x and y axes corresponding to the directions perpendicular and parallel to the microstrips within the detector plane, respectively, then alignment can be defined as finding the correct transformation rela-

tionship between the local coordinate system of each layer and the global coordinate system.

When a particle hits a certain position on a detector layer in the x direction within the global coordinate system, its z coordinate in the local coordinate system is zero⁵. Using the signal readout from the microstrips of the detector, the local x coordinate can be directly determined. The local y coordinate cannot be directly measured, but it can be estimated through the reconstruction of the trajectory in the global coordinate system using the y -detectors of other layers and by applying the transformation between the global and local coordinate systems. Once the complete local coordinates of the impact point are known, the correct coordinates of the particle impact point in the global coordinate system can be calculated by once again applying the relationship between the local and global coordinate systems for coordinate transformation.

$$\vec{r}_i = R_x(\gamma)_i R_y(\beta)_i R_z(\alpha)_i \left(\vec{r}'_i + \vec{r}_{i0} \right) \quad (3.103)$$

where:

$$\vec{r}'_i = \begin{pmatrix} x'_i \\ y'_i \\ z'_i \end{pmatrix} \quad (3.104)$$

$$\vec{r}_i = \begin{pmatrix} x_i \\ y_i \\ z_i \end{pmatrix} \quad (3.105)$$

$$R_x(\gamma)_i = \begin{pmatrix} 1 & 0 & 0 \\ 0 & \cos\gamma & -\sin\gamma \\ 0 & \sin\gamma & \cos\gamma \end{pmatrix} \quad (3.106)$$

$$R_y(\beta)_i = \begin{pmatrix} \cos\beta & 0 & \sin\beta \\ 0 & 1 & 0 \\ -\sin\beta & 0 & \cos\beta \end{pmatrix} \quad (3.107)$$

$$R_z(\alpha)_i = \begin{pmatrix} \cos\alpha & -\sin\alpha & 0 \\ \sin\alpha & \cos\alpha & 0 \\ 0 & 0 & 1 \end{pmatrix} \quad (3.108)$$

⁵this assumes the hit position to be “concentrated” in one single point and to choose the middle of the silicon sensor thickness. Other choices are possible, such as locate the hit position on one of the two external surfaces, but once the system is fixed, any choice is equivalent to the others

In Equation 3.103, \vec{r}'_i represents the local coordinates of the particle hit point on the i -th layer of the detector, \vec{r}_i represents the coordinates of this hit point in the global coordinate system, and \vec{r}_{i0} represents the coordinates of the origin of the local coordinate system of the i -th layer in the global coordinate system. From the equation, it can be seen that the coordinates of a hit point in the local coordinate system can be transformed into the global coordinate system coordinates through translations (Δx , Δy , Δz) along the three coordinate axes and rotations (γ , β , α) around the three coordinate axes. In other words, the six parameters Δx , Δy , Δz , α , β , and γ can be used as alignment parameters to fully describe the position and orientation of the local coordinate system within the global coordinate system.

For a multi-layer silicon microstrip detector, the measurement accuracy of particle trajectories typically requires errors to be well below tens of micrometers. Thus, the determination of the aforementioned six parameters must also be at the corresponding micrometer level. Ordinary tools, such as laser alignment, can no longer meet such precision requirements. The following will introduce how to accurately determine these six alignment parameters by looking to the Unbiased Residuals (UR), which are the differences in coordinates between the actual hit points of particles on a layer of the detector and the estimated points on the trajectory reconstructed by only other sensors. By creating specific statistical quantities from these unbiased residuals and using the mean values of their distributions, these six alignment parameters can be precisely determined. This method is only useful when there is already a rough, imprecise understanding of the six alignment parameters. This is because, when calculating the unbiased residuals, it is necessary to assume that our understanding of the position and orientation of each detector layer is correct, i.e., that the reconstructed particle trajectory from multiple detector layers does not significantly differ from the true trajectory.

Misalignment on x or y

First, let's introduce the measurement of parameter Δx (the measurement of Δy is of course similar to that of Δx).

Let's assume that a certain multi-layer silicon microstrip tracker is composed of 8 layers, as shown in Figure 3.44, with four layers measuring the x coordinate and the other four layers the y one. Except for one layer, with an "unknown" translation Δx , the positions and orientations of the other layers, with respect to the global coordinate system have been precisely measured. The "unknown" here refers to the unawareness of the translation, meaning the wrong belief that this layer of the detector has the same

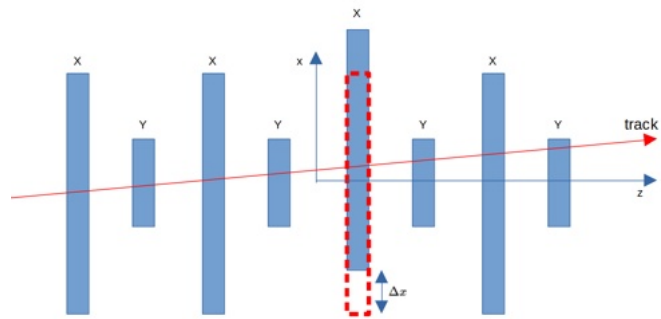


Figure (3.44) – Sketch of a of an arbitrary tracking system made by 4 layers measuring x and 4 measuring y . One of the x layers has a Δx translation.

position in the x direction as the other layers. In the figure, the blue arrows represent the axes of the global coordinate system, while the red arrow indicating the direction the particle passes through.

The translation Δx shown in Figure 3.44 can be more clearly represented using the positional relationship between the global coordinate system and the local coordinate system. As illustrated in Figure 3.45, the blue coordinate axes represent the global coordinate system, the black coordinate axes represent the local coordinate system of the detector layer actual position (with translation). The black dashed coordinate axes represents the local coordinate system of the detector layer incorrectly assumed position (without translation), the red arrow represents the particle trajectory, and the red circles represent the distribution of the actual measured hit point coordinates. From the figure, it is easy to see that the translation Δx can be represented by the average of the differences between the local coordinates x' of the measured hit points and the global coordinates x of the estimated points calculated from the particle trajectory, that is the average of the unbiased residuals in the x direction (UR_x^i). Assuming measurements have been taken for N events, then:

$$\Delta x = \frac{\sum_i^N UR_x^i}{N} \quad (3.109)$$

From the above formula, it is clear that for the detector layer in the x direction, the translation in the y direction cannot be determined (the opposite holds true for the detector layer in the y direction) because it is impossible to calculate the unbiased residual in the y direction (as the detector layer can only measure one-dimensional coordinates). However, this is not significant because, for the detector layer that measures the x (y) coordinate, the translation in the y (x) direction has no effect on the measurement.

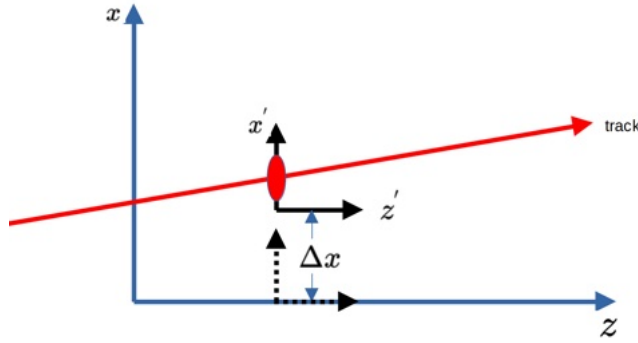


Figure (3.45) – Sketch showing the effect of the misalignment, Δx . The blue coordinate axes represent the global coordinate system, the black coordinate axes represent the local coordinate system of the detector layer actual position (with translation). The black dashed coordinate axes represents the local coordinate system of the detector layer incorrectly assumed position (without translation), the red arrow represents the particle trajectory, and the red circles represent the distribution of the actual measured hit point coordinates.

Symmetrically, the translation of the y -direction detector along the y -axis can be measured using the following formula:

$$\Delta y = \frac{\sum_i^N U R_y^i}{N} \quad (3.110)$$

Misalignment on z

Unlike the methods for measuring Δy and Δx , measuring Δz requires using a different statistical treatment.

Figure 3.46 shows an 8-layer tracker, where a layer has an “unknown” translation Δz , while the positions and orientations of all other layers, with respect to the global coordinate system, have been accurately measured. As before, by applying the transformation relationship between the global and local coordinate systems, one can more clearly represent the system as in Figure 3.47.

As in the previous case, in Figure 3.47, the black coordinate axes represent the local coordinate system of the detector layer actual position (with translation), the black dashed coordinate axes represents the local coordinate system of the detector layer incorrectly assumed position (without translation). It is easy to see from this figure that the translation Δz can be represented by the average of the following statistical quantity,

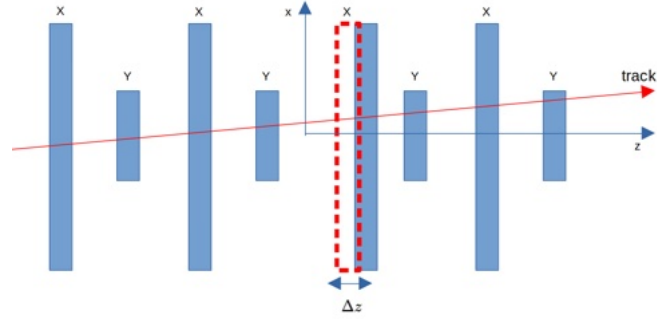


Figure (3.46) – Sketch of a of an arbitrary tracking system made by 4 layers measuring x and 4 measuring y . One of the x layers has a Δz translation.

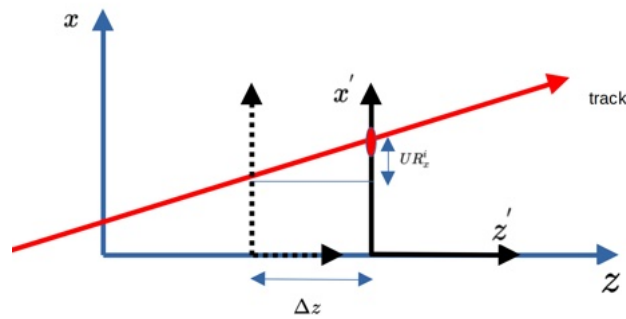


Figure (3.47) – Sketch showing the effect of the misalignment, Δz . The blue coordinate axes represent the global coordinate system, the black coordinate axes represent the local coordinate system of the detector layer actual position (with translation), the black dashed coordinate axes represent the local coordinate system of the detector layer incorrectly assumed position (without translation), the red arrow represents the particle trajectory, and the red circles represent the distribution of the actual measured hit point coordinates.

$$\Delta z = \frac{\sum_i^N UR_x^i / k_x^i}{N} \quad (3.111)$$

In the above formula, k_x represents the slope of the projection of each event's reconstructed trajectory in the $x - z$ plane. The formula shows that only events with k_x not equal to zero contribute to the measurement of Δz . Moreover, the narrower the distribution of k_x around zero, the more difficult it is to measure the translation Δz . For example, in beam experiments where the beam is almost perpendicular to the detector plane, Δz cannot be accurately measured by reconstructing the particle trajectories.

Similarly, the translation of the y -direction detector along the z -axis can be measured

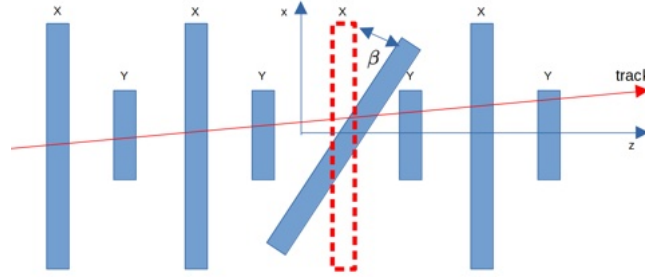


Figure (3.48) – Sketch of a of an arbitrary tracking system made by 4 layers measuring x and 4 measuring y. One of the x layers has a β angle rotation around the y-axis.

using the following approach:

$$\Delta z = \frac{\sum_i^N UR_y^i / k_y^i}{N} \quad (3.112)$$

Rotational misalignment on β or γ

In addition to the three translational degrees of freedom, each detector layer, similar to a rigid body, also has the freedom to rotate around the three coordinate axes. Let's first consider the rotation β around the y-axis (the measurement of rotation γ is similar to that of β).

Figure 3.48 shows an eight-layer tracker, with one layer with an unknown rotation angle β around the y-axis. Similarly to the previous approach, starting from Figure 3.48 and using the relationship between the global and local coordinate systems shown in Figure 3.49:

$$k_x^i = \frac{(UR_x^i + h_x^i) \cos \beta^i - h_x^i}{(UR_x^i + h_x^i) \sin \beta^i} \quad (3.113)$$

$$= \frac{UR_x^i \cos \beta^i + h_x^i (\cos \beta^i - 1)}{UR_x^i \sin \beta^i + h_x^i \sin \beta^i} \quad (3.114)$$

As mentioned earlier, this method is only useful when there is already a rough, imprecise understanding of the six alignment parameters. Therefore, the value of β^i is very small and $\cos \beta^i$ approaches 1. Additionally, it is evident that UR_x^i is much smaller than h_x . Thus, Equation 3.114 can be further simplified to:

$$k_x^i = \frac{UR_x^i}{h_x^i} \cdot \frac{1}{\tan \beta^i} \quad (3.115)$$

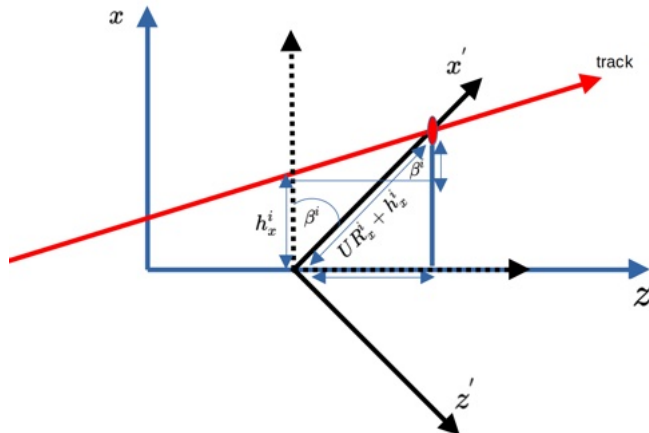


Figure (3.49) – Sketch showing the effect of the misalignment on β . The blue coordinate axes represent the global coordinate system, the black coordinate axes represent the local coordinate system of the detector layer actual position (with rotation), the black dashed coordinate axes represents the local coordinate system of the detector layer incorrectly assumed position (without rotation), the red arrow represents the particle trajectory, and the red circles represent the distribution of the actual measured hit point coordinates.

Therefore,

$$\beta = \arctan \sum_i^N \frac{UR_x^i}{k_x^i h_x^i} / N \quad (3.116)$$

Similarly, the rotation angle γ of the detector in the y direction around the x -axis can be expressed as:

$$\gamma = \arctan \sum_i^N \frac{UR_y^i}{k_y^i h_y^i} / N \quad (3.117)$$

It can be seen from Equation 3.116 and Equation 3.117 that only events with a non-zero trajectory slope contribute to the measurement.

Rotational misalignment on α

In addition to rotations around the x and y axes, the detector layer may also have a rotation around the z axis. Let's first consider the rotation of a detector layer in x direction (the case of a detector layer in the y direction is similar). Figure 3.50 shows that a detection layer in x direction has a counterclockwise rotation angle α around the geometric center, relative to the position and orientation we believe it should be in.

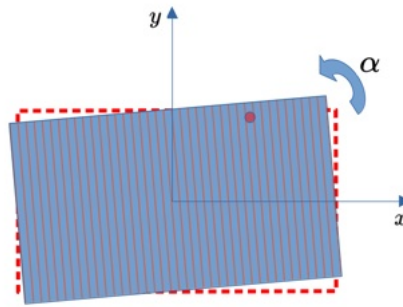


Figure (3.50) – Sketch of the α angle rotation around the z -axis of one x -direction layer of an arbitrary tracking system.

Figure 3.50 can be abstractly represented as Figure 3.51 by considering the relationship between the global coordinate system and the local coordinate system.

It is easy to see the following relationship from Figure 3.51,

$$h_x^i \cos \alpha^i + h_y^i \sin \alpha^i - h_x^i = UR_x^i \quad (3.118)$$

and therefore,

$$\sin \alpha^i = \frac{UR_x^i}{h_y^i} + \frac{h_x^i (\cos \alpha^i - 1)}{h_y^i} \quad (3.119)$$

Since α^i is very small, the left side of Equation 3.119 can be replaced with $\tan \alpha^i$ (which is more convenient), and the second term on the right side of the equation is zero. then,

$$\tan \alpha^i = \frac{UR_x^i}{h_y^i} \quad (3.120)$$

Assuming N events were measured, the average value of α is then:

$$\alpha = \arctan \sum_i^N \frac{UR_x^i}{h_y^i} / N \quad (3.121)$$

Similarly, the rotation angle α of the detector layer in the y direction around the z axis can be expressed as:

$$\alpha = \arctan \sum_i^N \frac{UR_y^i}{h_x^i} / N \quad (3.122)$$

Iterative alignment procedure

The above discussion covered how to “align” a detection layer using unbiased residuals. In that discussion, for simplicity, it was assumed that only one detection layer actual

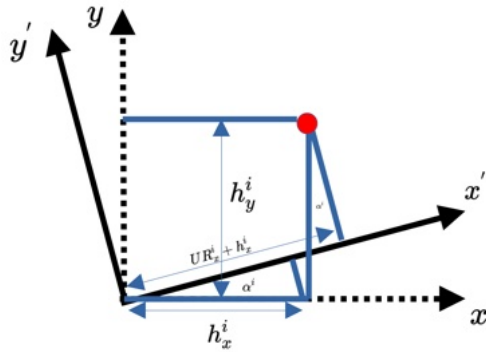


Figure (3.51) – Sketch showing the effect of the misalignment on α . The blue coordinate axes represent the global coordinate system, the black coordinate axes represent the local coordinate system of the detector layer actual position (with rotation), the black dashed coordinate axes represents the local coordinate system of the detector layer incorrectly assumed position (without rotation), the red circles represent one actual measured hit point coordinate.

position and orientation deviated from what we believe to be its intended position. However, in real-world situations, a detector with N layers may have small deviations in position and orientation for each layer, all of which require alignment. Therefore, the alignment must be studied across all $6N$ alignment coefficients.

When studying all the alignment coefficients together, and to speed-up the data processing, often ordinary residuals are used instead of unbiased residuals, and the alignment is carried out in multiple, iterative, steps. Assuming the process is divided into j steps, equation 3.103, which describes the transformation relationship between the local coordinate system of each detection layer and the global coordinate system, will be rewritten as the following series of equations:

$$\begin{aligned}\vec{r}_i^1 &= R_z(\gamma)_i^1 R_y(\beta)_i^1 R_x(\alpha)_i^1 \left(\vec{r}'_i + \vec{r}_{i0}^1 \right) \\ \vec{r}_i^2 &= R_z(\gamma)_i^2 R_y(\beta)_i^2 R_x(\alpha)_i^2 \left(\vec{r}'_i + \vec{r}_{i0}^2 \right) \\ &\vdots \\ \vec{r}_i^j &= R_z(\gamma)_i^j R_y(\beta)_i^j R_x(\alpha)_i^j \left(\vec{r}'_i + \vec{r}_{i0}^j \right)\end{aligned}\tag{3.123}$$

$$\vec{r}_i^j = R_z(\gamma)_i^j R_y(\beta)_i^j R_x(\alpha)_i^j \left(\vec{r}'_i + \vec{r}_{i0}^j \right)$$

From equation 3.123, it can be seen that in each step, there is a corresponding set of alignment coefficients that transform the local coordinate system, representing the position and orientation of a single detection layer, into a new position and orientation

relative to the global coordinate system. Through j steps, the local coordinate system is ultimately aligned to its correct position relative to the global coordinate system. At this point, the coordinates of the particle impact points in the local coordinate system are also transformed to their correct values in the global coordinate system through this series of transformations.

Overall, the alignment coefficients from all the steps combine to describe a “historical” process spanning j steps. The effect of this process is to transform the local coordinate system from its initially incorrect assumed position and orientation to its correct position and orientation relative to the global coordinate system.

In this process, the alignment coefficients for each step are actually calculated based on the latest position and orientation of the local coordinate system from the previous step. For example, at the beginning (first step), with no prior information, the coordinates of the impact points are transformed based on the assumed possible position and orientation of each detection layer. The first set of alignment coefficients is then calculated by measuring the residuals in the global coordinate system: if the assumed position and orientation happen to match the true position and orientation relative to the global coordinate system, the alignment coefficients will be nearly zero. Then, in the second step, the first set of alignment coefficients is used to transform the local coordinate system to a new position and orientation relative to the global coordinate system. The particle impact points are then recalculated in the global coordinate system, and the second set of alignment coefficients is determined by the residuals, which should be significantly smaller than the first set). This second set of alignment coefficients will also transform the local coordinate system from the position and orientation determined in the first step to a new position that is even closer to the true position, bringing the global coordinate values for the particle impact points closer to the correct values. As a result, the third set of alignment coefficients calculated by residuals will become even smaller. This process is repeated for the fourth, fifth, and j -th sets of alignment coefficients until the alignment coefficients are considered to be sufficiently close to zero.

CHAPTER 4

Detector Studies with Particle Beams

The AMS-02 L0 upgrade and the HERD SCD are both characterized by the use of single side silicon microstrip detectors daisy chained in long ladders, with up to 12 units connected to the same front end electronics. As the length of the daisy chained strips increases, detector performances could degrade due to the augmented strip capacitance. Tests with particle beams have been carried in the last couple of years, 2023 and 2024, to verify detector performances in terms of position resolution and charge separation. In this chapter we will first report on the results of L0 ladder tests with beam muons and ions beams, and then we will discuss the HERD SCD ladder tests with single charged particles and ions beams.

4.1 L0 beam tests

As mentioned in Chap.2, AMS-02 detector will undergo an upgrade in 2026 to increase its acceptance by means of a new silicon detection layer, L0, to be placed on top of the experiment. L0 will consist of two planes of silicon microstrip sensors, each composed of 36 ladder units. As shown in Figure 4.1 each ladder is composed of 8, 10, or 12 silicon sensors connected to a front-end electronics board, the L0 Electronics Front-end (LEF). A readout pitch of $110 \mu\text{m}$ is used, leaving in between three floating strips with an implantation pitch of $27.5 \mu\text{m}$. It can also be seen that the design of the LEF board includes not only the VA chip but also the ADC (14-bit) and a FPGA for data/command

processing. The board is equipped with 16 VA chips, for a total of 1024 analog channels. Every two VA chips are connected in multiplexed configuration to the same ADC to maximize the modularity of the system. Thanks to the onboard FPGA, the board has only a digital interface, and data compression is implemented in the FPGA itself to minimize the data volume to be moved to the next level of the DAQ system. This is quite different with respect the approach used in the AMS-02 tracker where data digitization and compression is performed in a dedicated board distinct from the front end electronics with VA chips. As shown in Figure 4.2, the L0 ladder differs from the ladder currently used in the AMS-02 silicon detector. Unlike the AMS-02 tracker, which is made by double-sided silicon sensors, L0 will use single-sided silicon sensors to simplify silicon sensors production, their assembly in longer ladder units and the ladder integration on planes. Also sizes are quite different, with $72 \times 41 \text{ mm}^2$ sensor size in the AMS-02 tracker to be compared the larger size of $113 \times 80 \text{ mm}^2$ in L0, to minimize the number of sensors needed to cover the large L0 surface.

The new detector and electronics design will naturally lead to changes in performance. To better understand the spatial resolution and charge detection capabilities of the L0 ladder, beam tests on the L0 ladder were organized at CERN in October 2023 and May 2024 using heavy ions and muons, respectively. In the following sections, these two beam tests will be introduced separately.

4.1.1 Beam Test with muons

As discussed in the previous chapter, the energy deposited by particles passing through the detector is proportional to the square of their charge (cfr Sec. 3.48): dealing with

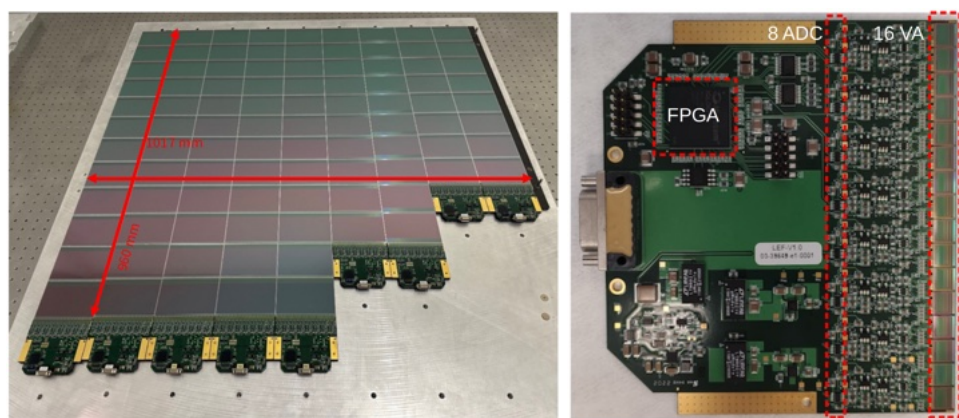


Figure (4.1) – Left: a quarter plane of L0 with ladders of different lengths. Right: close-up view of the LEF.

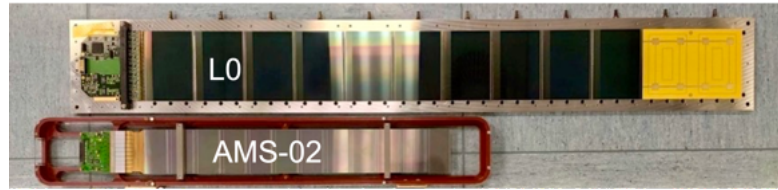


Figure (4.2) – A comparison between the L0 ladder and the AMS-02 tracker ladder.

a unit charge particle means to be in the lowest signal-to-noise ratio measurement conditions, i.e. worst case for detection efficiency and spatial resolution. Therefore, a beam test using muons as unit charge particles in the MIP regime has been carried out as a significant benchmark of the detector performance.

The beam test with muons was conducted in May 2024 at the H8 beam line of the Super Proton Synchrotron (SPS) at CERN for nearly a month. Two different setups were used focused on the study of single sensors (setup a) and of a 10 sensors prototype of the L0 ladder (setup b). Fig. 4.3 shows the schematics of the setup with the L0 ladder prototype, details of the different elements and their connections for one out of the two configurations used in the test. Beam is aligned along the z direction, i.e. orthogonal to the different setup elements.

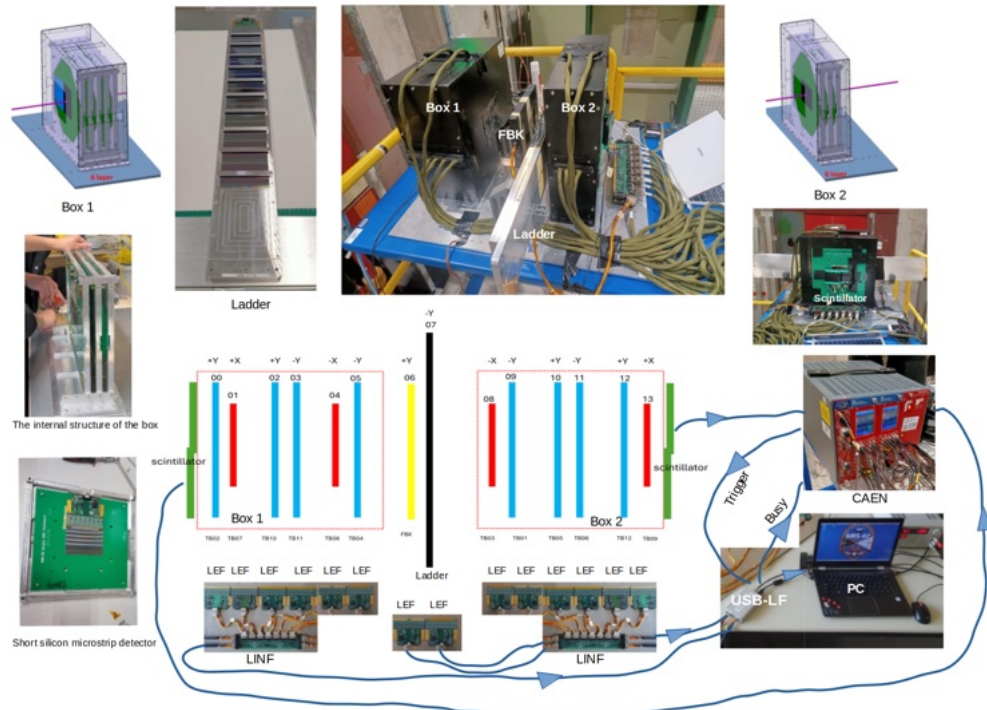


Figure (4.3) – Configuration of the setup (b) used to test L0 ladder in the muon beam test.

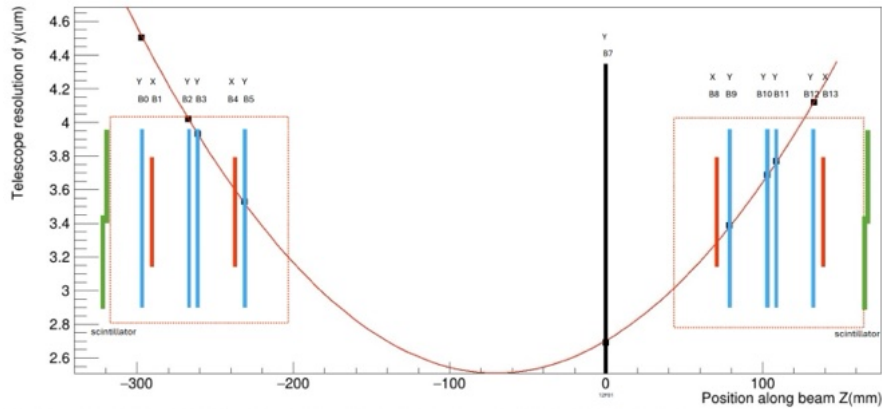


Figure (4.4) – The beam telescope tracking resolution as a function of the z coordinate along the beam, assuming a $7 \mu\text{m}$ resolution in the single point measurement.

Two scintillators, represented by green rectangles in the schematics, are installed on the outermost windows of the beam path regions in the front and rear boxes, providing high-quality trigger signals for the entire system via an "and" logic gate. Each scintillator consists of two smaller scintillators stacked together to form a larger scintillator, increasing the coverage area. 12 short silicon microstrip detectors are divided into two groups and installed in two boxes positioned in front of and behind the L0 ladder under test (black rectangle), respectively, serving as two beam monitors. These monitors are used to reconstruct the beam trajectory and help study the spatial resolution of the ladder. The short silicon microstrip detectors, measuring x (red rectangles) or y (blue rectangle) coordinates, consist of a single silicon microstrip sensor with the same structure and size as those used in the L0 ladder, plus a front-end electronic board (LEF). It should be noted that the front-end electronics board of the short silicon microstrip detector is identical to that of the L0 ladder. The L0 ladder used in the test is composed of 10 silicon microstrip sensors, close to it a different microstrip detector manufactured by FBK (Trento) is represented by the yellow rectangle, tested performances for this latter detector will not be discussed in this thesis. The same setup configuration, is presented in Fig.4.4 where actual positioning along the beam, i.e. in z , can be appreciated for the different elements. The red curve superimposed to the scheme represents the accuracy in the trajectory reconstruction, computed according to Eq. 4.3 by the beam monitor: the ladder is not positioned in correspondence of the beam telescope maximum resolution but slightly to the right. This is due to avoid interference of the ladder support structure with those of the other detectors positioned in front of and behind the ladder.

Figures 4.5 shows the setup configuration a) used during the beam test to study single sensor resolution and detection efficiency, in particular in the bias resistor area.

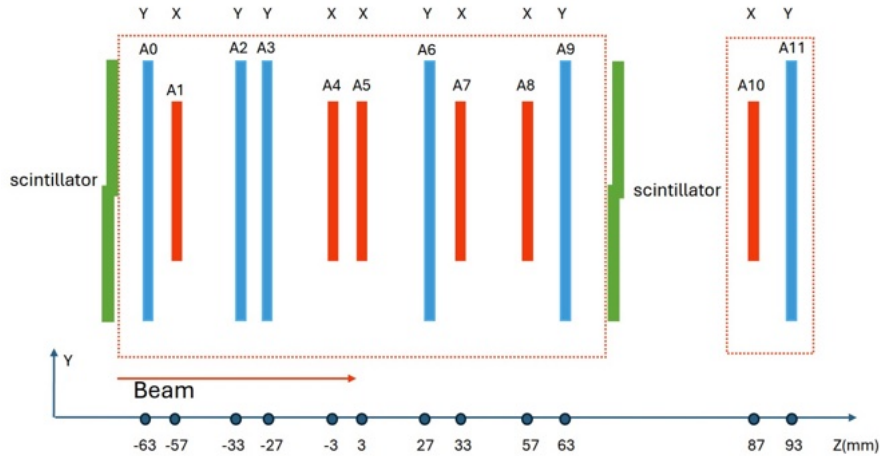


Figure (4.5) – Test beam setup (a) for the study of single sensors performances.

The bias resistor regions of the single silicon microstrip sensor are shown in Figure 4.6. In that scheme, the bias resistors of the readout strips are located at the right end of the detector, with a size of ≈ 2.8 mm, while the bias resistors for the floating strips are located at the left end, with a size of ≈ 11.6 mm. The high resolution images in the inserts clearly show the bias resistors as polysilicon serpentines and how the floating strips do not extend in the bias resistor region of the readout strip (right end), where as the readout strips run through the bias resistor region of the floating strips (left end). The structural differences in the bias resistor regions with respect the strip configuration along the silicon can result in different detection efficiencies and spatial resolutions

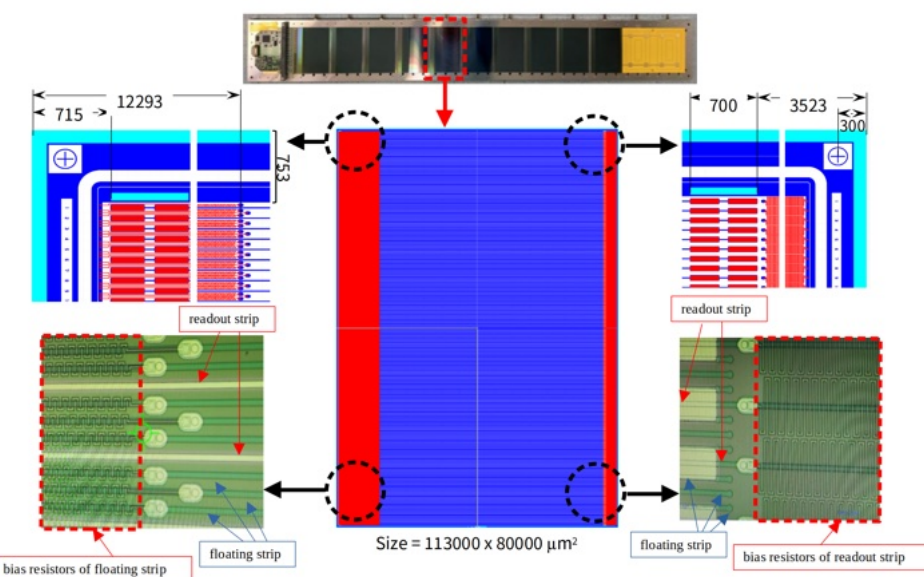


Figure (4.6) – The bias resistor regions on a silicon microstrip sensor.

when measuring particles.

Calibration & Alignment

Efficiency and position resolution studies were performed in the a) and b) setup configurations. As a first step data were calibrated and signal clusters defined as described in Chap. 4.1.1. Common noise, pedestal, noise levels and the signal over noise distributions (S/N) are reported in figures from 4.7 to 4.10 for the typical telescope sensor and the L0 ladder. As expected, the noise level in the L0 ladder is larger due to the long strip capacitance and correspondingly the S/N distribution for the L0 ladder peaks at ~ 7 whereas in the single sensor a most probable value for the S/N is ~ 12 . Any signal selection implying a cut on the signal over noise (S/N) of the *seed* strip will then result in a reduced efficiency, and also a worst spatial resolution is expected.

For both efficiency and position resolution studies, an accurate track prediction on the detector under analysis is needed. The spatial resolution for a given detector can be evaluated from the residual distribution, i.e. the difference between the predicted position for the particle and the measured one. At the same time, the signal efficiency is evaluated by the ratio of the number of detected particles and the number of particles passing through it. The latter requires an external prediction on the particles traversing the detector.

Following procedure of Sec.3.4.5 alignment of the beam monitor detectors and L0 ladder were performed after calibration. In Fig.4.11 examples of the distributions of residuals before (left) and after (right) alignment are shown for a beam monitor detector (top) and for the L0 ladder (bottom). Starting from these distributions, the spatial resolution has been estimated as described in the following paragraph.

Spatial Resolution & Efficiency

The unbiased residual on a detector is the difference between the coordinate of the particle impact point measured by the detector and the coordinate of the estimated impact point on the particle trajectory reconstructed by fitting data from other surrounding detectors. Therefore, the standard deviation, σ , of the unbiased residual distribution can be considered as the sum of two contributing factors. One contribution comes from the spatial resolution of the silicon microstrip detector itself (intrinsic spatial resolution), and the other contribution comes from the fitting prediction error. That is,

$$\sigma_{UR,i} = \sqrt{\sigma_{fit,i}^2 + \sigma_{res,i}^2} \quad (4.1)$$

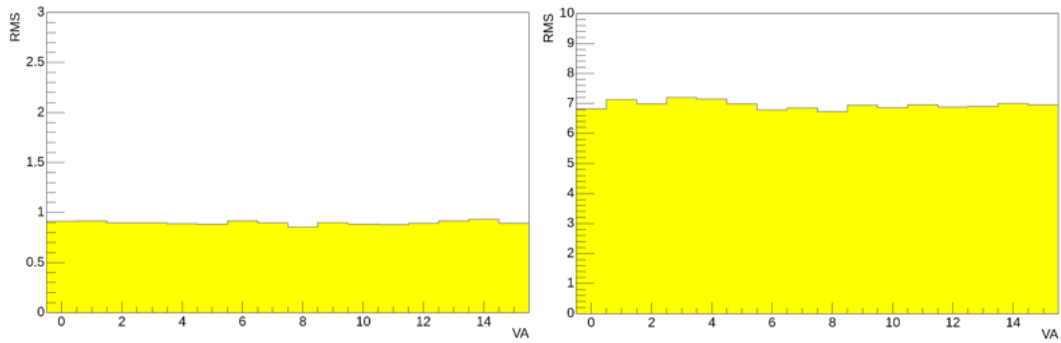


Figure (4.7) – Distribution of Common Noise width as a function of VA number for a beam monitor sensor (left) and L0 ladder (right)

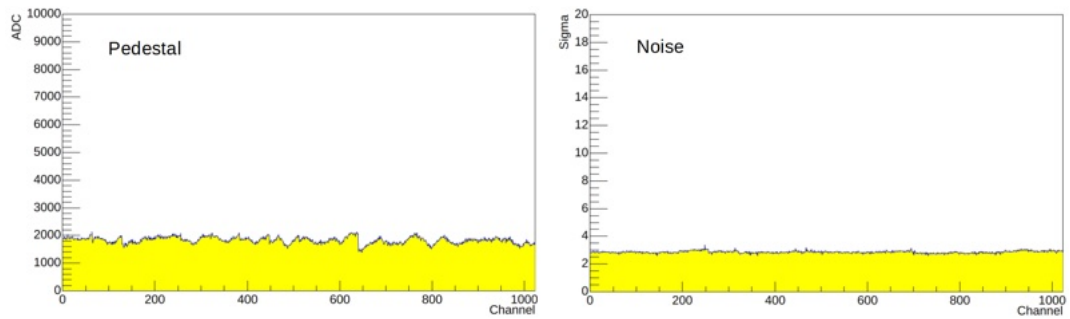


Figure (4.8) – Pedestals (left) and noise (right) for a beam monitor sensor.

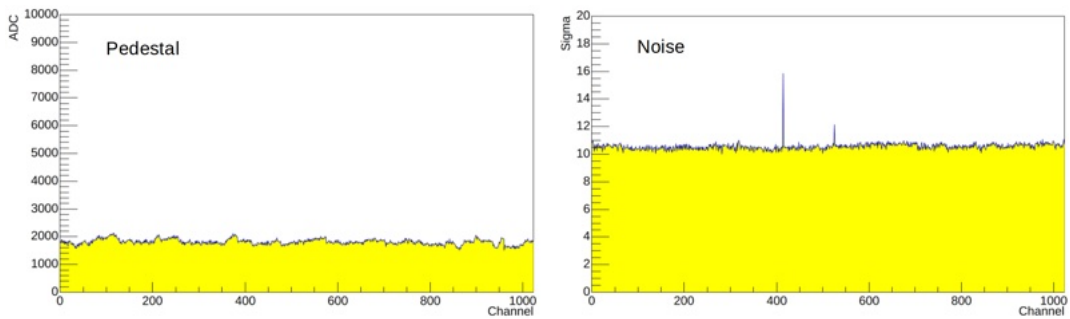


Figure (4.9) – Pedestals (left) and noise (right) for L0 ladder.

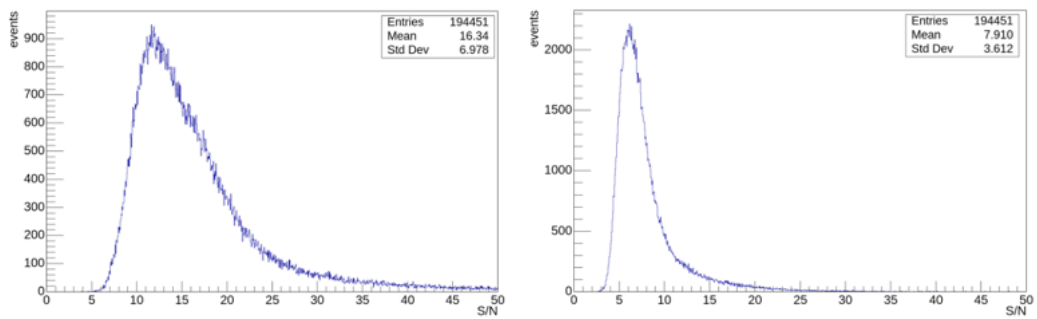


Figure (4.10) – Signal over Noise distribution in a single sensor (left) and on the L0 ladder (right).

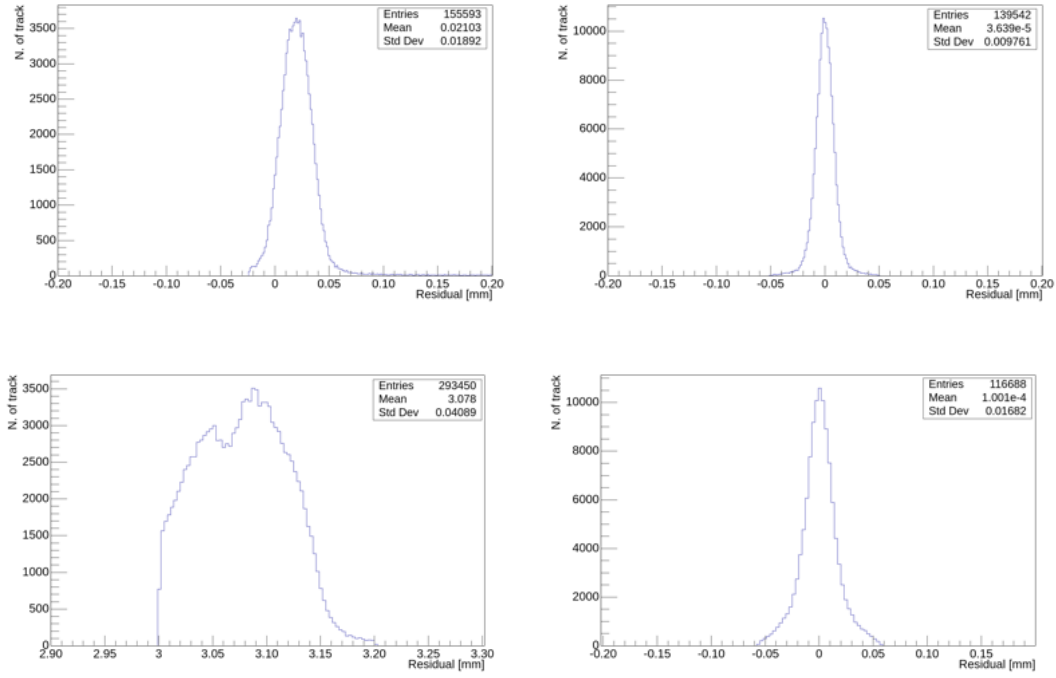


Figure (4.11) – Residual distribution before (left) and after (right) alignment for a beam telescope sensor (top) and the L0 ladder (bottom).

or

$$\sigma_{res,i} = \sqrt{\sigma_{UR,i}^2 - \sigma_{fit,i}^2} \quad (4.2)$$

In Equation 4.1 and 4.2, index i refers to the ladder under consideration, $\sigma_{UR,i}$ can be obtained by performing a Gaussian fit to the unbiased residual distribution of the i^{th} detector layer, and $\sigma_{fit,i}$ can be calculated using the following formula:

$$\sigma_{fit,i} = \sigma_s \sqrt{\left(\sum_j^n z_j^2 / n + z_i^2 - 2z_i \cdot \sum_j^n z_j^2 / n \right) / \left(\sum_j^n z_j^2 - \sum_j^n z_j \sum_k^n z_k \right)} \quad (4.3)$$

In Equation 4.3, σ_s is a rough estimate of the detector spatial resolution, taken to be $7\ \mu m$ as a reference in Fig.4.4, and z represents the coordinate of each detector layer along the z -axis. Figure 4.12 shows the fit to the residual distributions for a beam telescope detector (left) and the L0 ladder (right). The sum of two gaussian functions has been used to describe the *core* of the distribution and its *tails*. The intrinsic resolution, evaluated from the main gaussian and taking into account the prediction error according to Eq.4.2, is of $\sim 8.3\ \mu m$ and $11.3\ \mu m$ for the beam telescope detector and the L0 ladder (respectively). Similar results for the telescope sensors were obtained in configuration a).

The efficiency evaluation at the single sensor level has been first studied in configuration a) using just the ten sensors located in the first box, between the scintillator slabs.

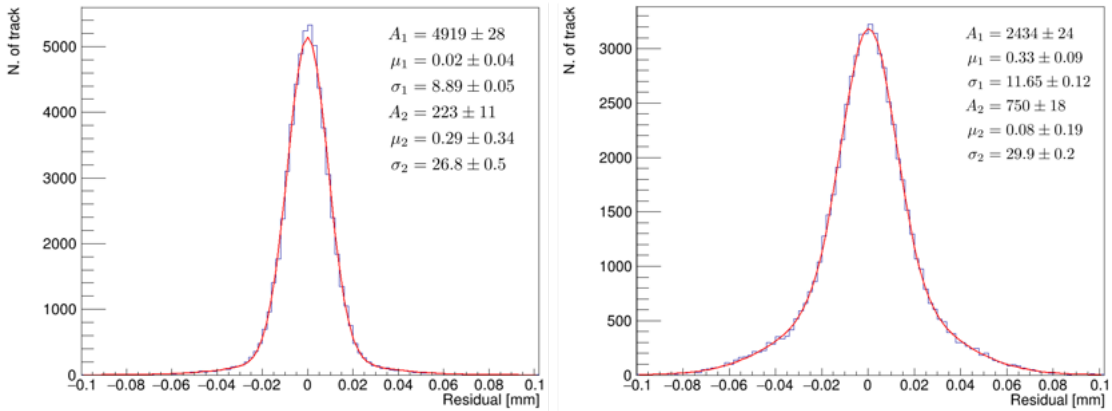


Figure (4.12) – The unbiased residuals distribution of the B05 telescope detector and the L0 ladder. Superimposed to the distributions the result of the fit with lengths measured in μm , with the sum of two Gaussian functions used to evaluate the intrinsic resolution.

Detectors A4/A5, located near the central symmetric position of the first box where the trajectory reconstruction error is minimal, were chosen as the subject of study. These detectors measure the x -coordinate, with the bias resistor regions located at both the top and bottom ends of the strips which are aligned along the y -axis. Therefore, the y -coordinate of the particle trajectory, reconstructed from the other y -direction detector layers, was used to determine efficiency along the strip length.

Fig.4.13 (left) shows the beam profile along y at the location of the A5 detector as reconstructed by A0, A2, A3, A6, A9 detectors. The beam profile ends at ± 56.5 mm due to the size along y of the reference detectors, whose strips run along x coordinate of the global reference system. The same distribution is presented on the right only for those events *detected* in the A5 detector, where a *detected* particle is defined if at least one readout strip signal on the A5 detector exceeds $5\sigma_{\text{noise}}$. Noticeable cutoffs in the distribution can be seen close to ± 40 mm, roughly corresponding to the 80 mm size of the sensor along that direction. The few events barely visible at $|y| > 40$ mm, i.e. out of the A5 detector area, can be attributed to a pile-up effect, that is the simultaneous passage of more than one particle, one entering A5 - thus being selected - and the other reconstructed by the other sensors out of the A5 geometrical area.

The ratio between the right and the left distributions of Fig.4.13 determines the detection efficiency as a function of y , as presented in Fig.4.14. Close to the edge, in the bias resistor area, a 100% efficiency is observed in a ~ 3 mm region compatible with the dimensions of the readout strip bias resistor region. A constant efficiency of $\sim 98\%$ characterizes the sensor at $y > -37$ mm. Efficiency drops to ~ 0 (not exactly 0 due to the pile up events) on both sensor edges within $\sim 400 \mu\text{m}$ from the nominal

sensor dimension, i.e. a couple bins at the distribution ends that are compatible to the boundary sensor regions with no strips. No significant effects on efficiency can be seen in the floating strip resistor bias region.

The same approach was used in the b) setup configuration to determine the L0 ladder detector efficiency at different x values (since the ladder measures the y -coordinate, its strips are parallel to the x -direction). Similarly to what was presented in Fig4.13 for the single sensor, the beam distribution along the global coordinate system x -axis, is presented on the left plot in 4.15 (left) while on the right the same distribution for only the events detected by the ladder Figure 4.15. The requirement to have a detected particle is that at least one readout strip signal exceeds $3.5\sigma_{\text{noise}}$, and this is expected to have a not negligible impact on the efficiency given the higher value of the noise in the ladder wrt the single sensors (cfr. Figg. 4.8, 4.9). Also in this configuration the beam profile has the size of the reference detectors, but it is not truncated in the detected events since it is not limited anymore by the single sensor length. The sudden drop in the detected events distribution close to the x -axis origin is due to the gap between the two adjacent sensors aligned with the beam center. The ratio between the two distributions of Fig. 4.15 is presented in Fig. 4.16.

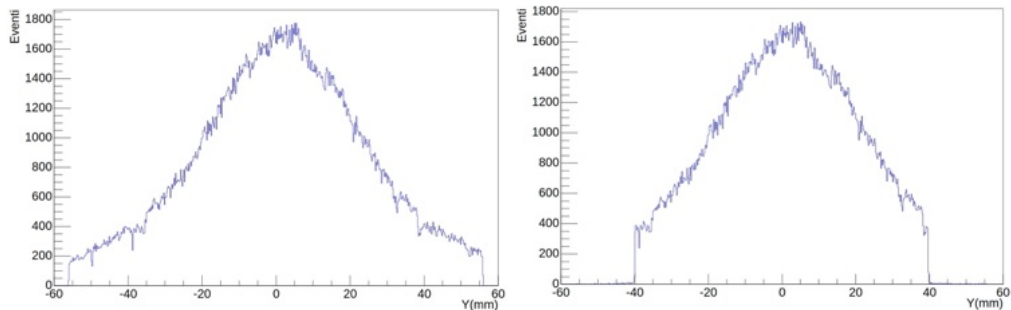


Figure (4.13) – The beam profile along the global coordinate system's y -axis at the location of the A5 detector for all particles (left) and for those detected in the A5 detector (right).

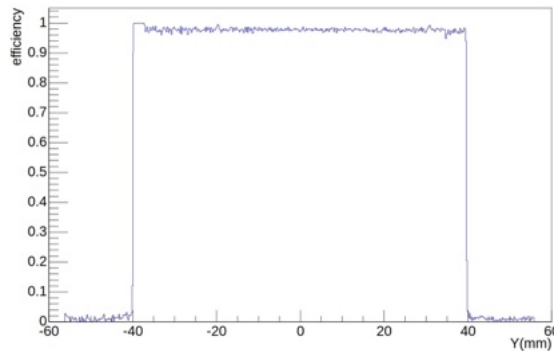


Figure (4.14) – The detection efficiency of the A5 detector as a function of the y coordinate along the strip.

A detection efficiency of $\sim 92\%$ characterizes the ladder far from its edges, less than for the single sensor case as expected due to the higher intrinsic noise. On the left of the efficiency drop in the detector gap, a restricted region of ~ 3 mm with 100% efficiency is observed as on the edge of the single sensor study.

This effect, given its size, can be associated to the region of the resistor bias for the readout strips. In that region, floating strips are not implanted anymore and there is a minimal charge lost to the backplane due to capacitive coupling. This results in a higher readout signal that is more likely to exceed the threshold and be detected, thus leading to higher detection efficiency in this region compared to other regions.

The performance in bias resistors region have been studied also in terms of spatial resolution, both in the L0 ladder and at the single sensor level. Figure 4.17 shows the unbiased residuals distribution as a function of the different positions along the strip direction for A05 and the L0 ladder. As observed in the figure, the distribution of unbiased residuals is wider in the readout strip bias resistor region. This can be better

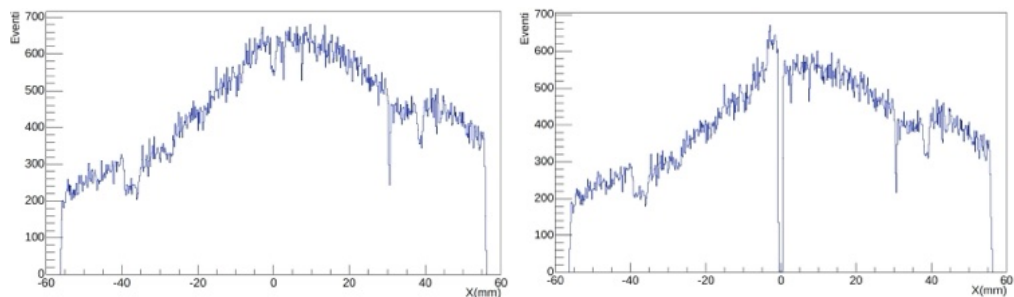


Figure (4.15) – The beam profile for all reconstructed events at the L0 ladder location (left) and for those also detected in the ladder (right).

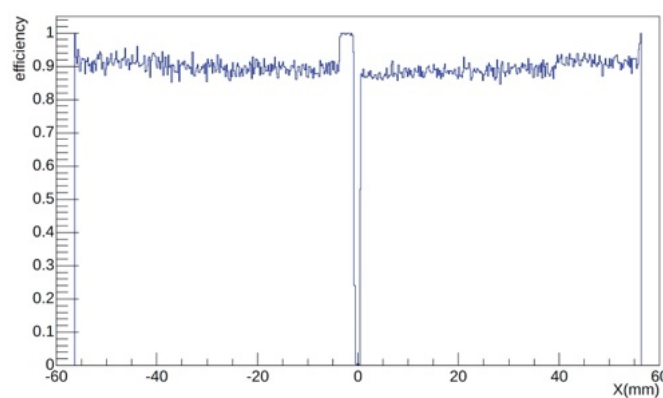


Figure (4.16) – The detection efficiency of the L0 ladder as a function of the x coordinate along the strips.

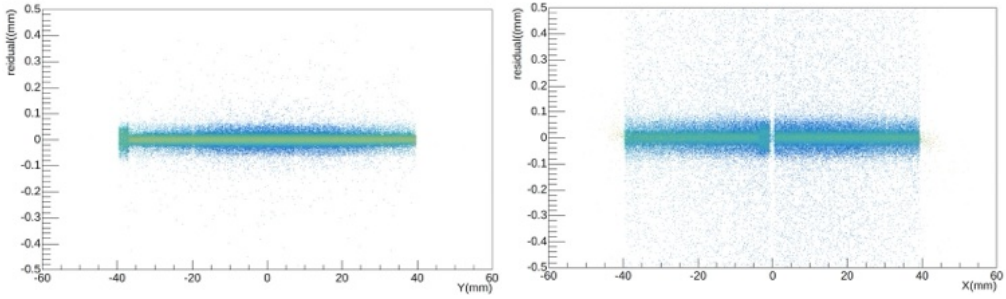


Figure (4.17) – The unbiased residuals at different positions along the strip direction a single sensor (left) and the L0 ladder (right).

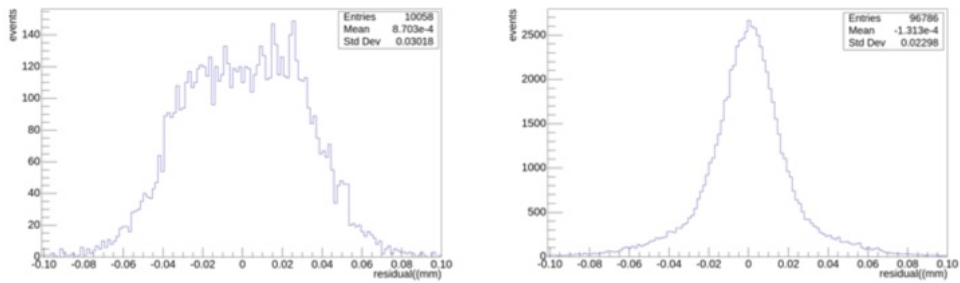


Figure (4.18) – The L0 ladder unbiased residuals distribution for the readout strip bias resistor region (left) and the nominal sensor zone (right).

appreciated in Fig. 4.18 where the unbiased residuals distributions are shown in L0 ladder separately for the readout strip bias resistor region (left) and the *nominal* sensor zone (right). In the nominal sensor zone the distribution reflects the spatial resolution presented in Fig.4.12, whereas a nearly uniform distribution characterized the readout strip bias resistor region with a width comparable to that in the silicon digital readout case with no coupling between adjacent readout strips, i.e. $p/\sqrt{12}$ being p the inter strip pitch. Neither in efficiency nor in spatial resolution significant effects have been pointed out by this study in the floating strips bias resistor region, both at the sensor and at the ladder level.

4.1.2 Test with heavy ions

In October 2023, a five-days heavy ion beam test was conducted at CERN for the L0 ladder with a beam of $Z < 82$ fragments, produced by directing a lead nucleus beam on a beryllium target. A longer beam time was originally foreseen on the H4 beam line of the Super Proton Synchrotron (SPS), however, due to a sudden H4 beam line failure, the already installed setup had to be relocated to the H8 beam line, and the beam time shared with another experimental team. As a result, part of the original test

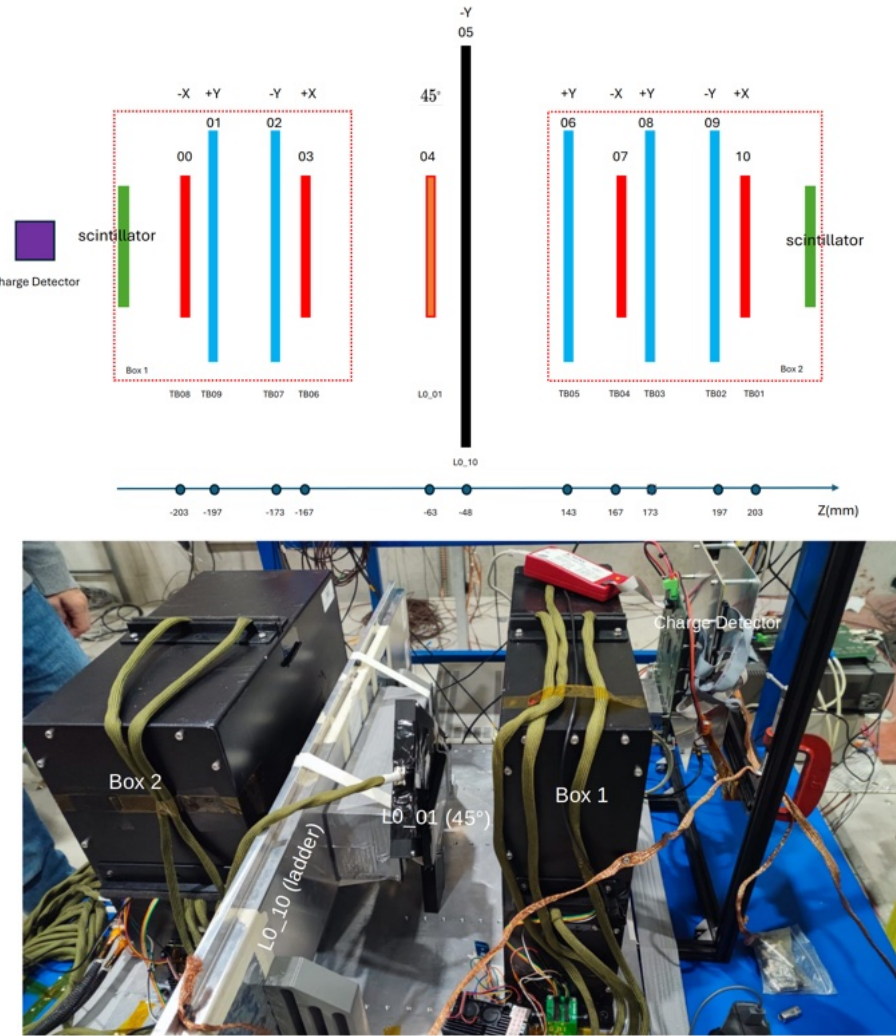


Figure (4.19) – Schematics (top) and actual configuration (bottom) of the ion beam test setup. On the picture of the actual setup, the beam would come from the right, i.e. the Z axis is in the opposite direction with respect to the the schematics.

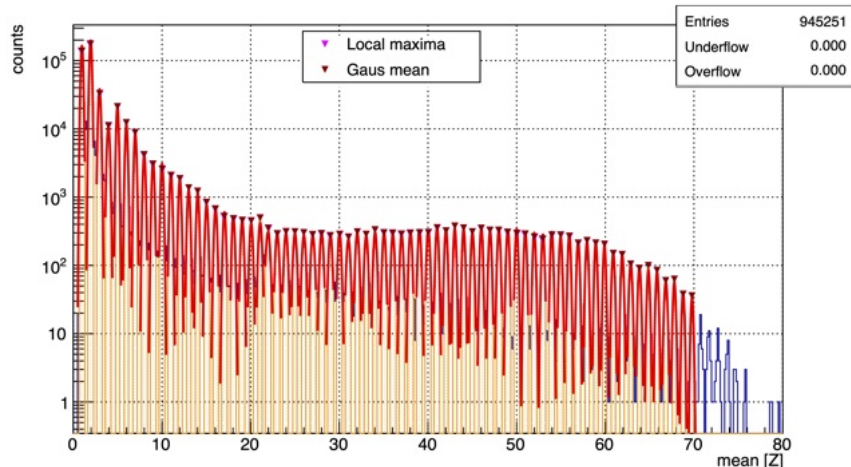


Figure (4.20) – Charge distribution as measured by the Charge Detector.

objectives - related to spatial resolution at different Z values - could not be achieved due to time constraints and insufficient statistics. Therefore, in the following only an overview analysis related to the charge measurement will be discussed.

The test beam schematics and its actual configuration are shown respectively in the upper and lower parts of Fig.4.19. The setup is quite similar to that of the muon beam test, short microstrip detectors were installed in the two boxes at the front and rear as beam monitors, and the same L0 ladder with 10 sensors was placed between the two boxes. In addition, a charge detector (CT) provided by the INFN Florence group was installed in front of all the detectors to supply an independent external measurement of the particle charge. As shown in Figure 4.20, the CT has strong charge identification capability, which can significantly aid in studying the charge measurement properties of the ladder.

As discussed in Sec.3.4.3 the reconstructed charge exhibits a dependence on the particle's impact relative to the readout strip, which is commonly approximated with the η parameter. As the particle charge increases, the study of reconstructed charge dependence on η is further complicated by effects of saturation in the VA chip.

Figures 4.21 shows the distribution of the cluster charge vs η for one reference sensor of the beam monitor (left) and the L0 ladder (right). Since the energy loss scales with Z^2 , the square root of the cluster signal is used in these distributions to have immediate reading of non linearity and saturation effects versus Z. The clusters included in the statistics are those with the largest signal detected by each detector for each event. The observed structures reflect different effects. At low charge values, events populate the full η interval with a gradual depletion of $\eta = 0$ and $\eta = 1$ regions as the signal starts to

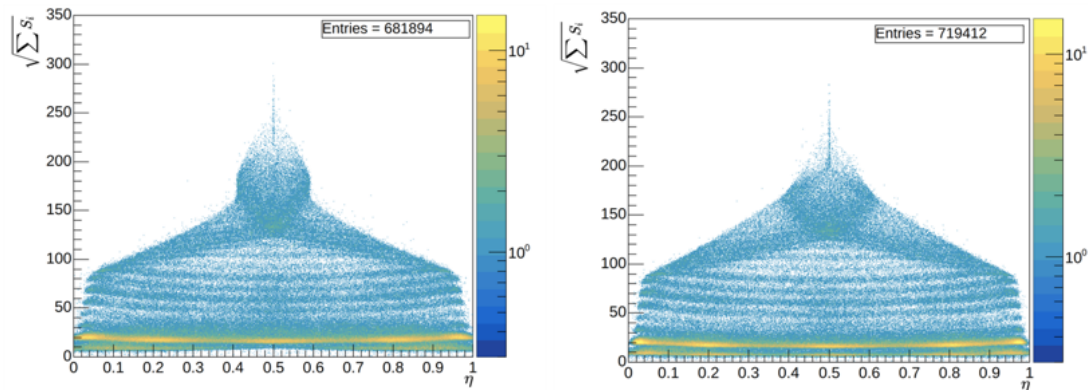


Figure (4.21) – Cluster integral charge vs η in a beam monitor sensor (left) and in the L0 ladder (right).

increase also on the second highest strip in the cluster. Also the expected effect of charge loss in the intermediate η region can be appreciated in the bending of the horizontal lines. As the charge increases, not only events tend to populate the central η region, but saturation effects clearly deform the distribution.

Figure 4.22 shows the different η distributions for the square root of cluster signals < 80 ADC (left) and ≥ 80 ADC (right). In the signal linear regime, the η distribution reflects the expected behaviour for the three floating strips implantation between the readout strips. At higher signals, the η distribution is dominated by non linear effects, and tends to 0.5 since both strips used for its definition are in a saturation regime. Saturation for single strip signal is indeed expected at ~ 14000 ADC, whose square root is ~ 118 . The 14 bit ADC would in fact correspond to a maximum signal of 16384 ADC, with a pedestal of ~ 2000 ADC to be subtracted. As a matter of fact, saturation on the highest strip signal effectively spoils the η calculation, that becomes ill-defined and fixed to 0.5 as both strips are saturated. Figure 4.23 shows the cluster charge distribution for the L0 ladder into different η regions, at the extremes of the η range $\eta \sim 0, 1$ (left) and in the

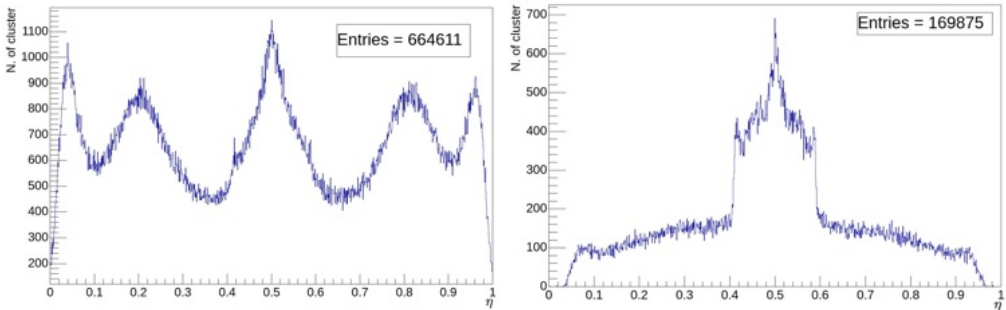


Figure (4.22) – The η distribution in the ladder at low, < 80 ADC (left), and high, ≥ 80 ADC (right), cluster charges.

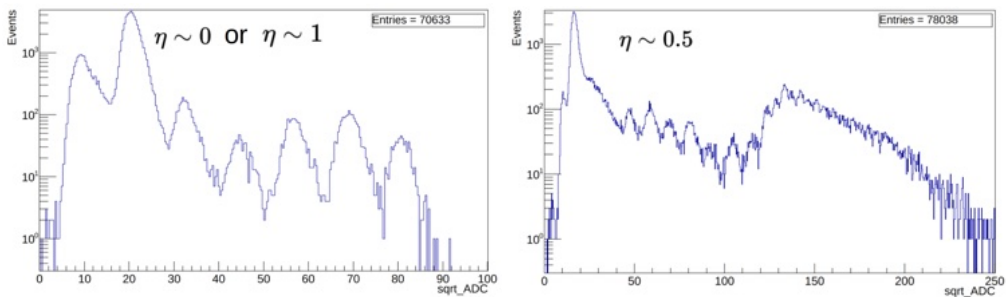


Figure (4.23) – The cluster charge distribution for the ladder at the extreme $\eta \sim 0, 1$ values (left) and in the central $\eta \sim 0.5$ region

central part $\eta \sim 0.5$ (right). The different peaks in the charge distribution correspond to ions with increasing Z : only $Z < 9$ charges can be reconstructed for $\eta \sim 0, 1$, whereas a wider charge range is covered by η value is near 0.5.

However, charge separation is lost at high Z values, due to the combination of different effects. The non linearity in the VA response effectively compresses the scale, bringing the peaks closer and closer as Z increases. Moreover, at high Z , up to 10-15 strips can be used in defining the cluster charge, and the convoluted effect of the single strip noise in the definition of cluster charge effectively widens the charge peak distribution, worsening the charge separation between adjacent peaks. This latter effect, can be mitigated by using the signal of the seed strip in the cluster instead of the cluster integral. Figure 4.24 shows the square root of the signal in the seed strip as a function of η for the L0 ladder, the different charge patterns are clearly visible as well as the saturation in the central part η region (right) where the standard η correction approach to retrieve identify different charge values is effectively prohibited by the steep and compressed V shaped pattern in the central η region.

We therefore abandoned the η correction approach, directly studying the features of the two readout strips with the highest signals, the seed strip s_1 and the closest with higher signal s_2 .

Figure 4.25 shows the s_1 versus the s_2 distribution for the L0 ladder (left). The events within the red rectangular box correspond to those with η values near 0.5. Rotating the distribution counterclockwise by 45° yields the rightmost distribution.

Projecting onto the ordinate the region within the red rectangle of the rightmost

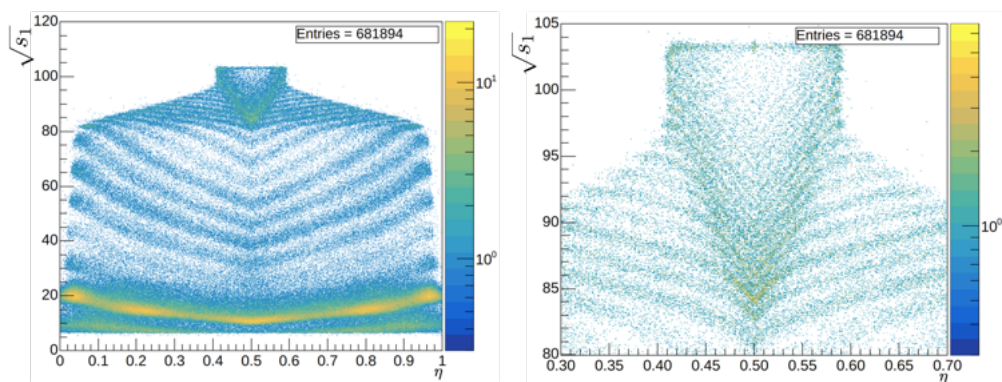


Figure (4.24) – Square root of the signal in the cluster seed strip in the L0 ladder (left), on the right an enlarged view of the central η region close to signal saturation region.

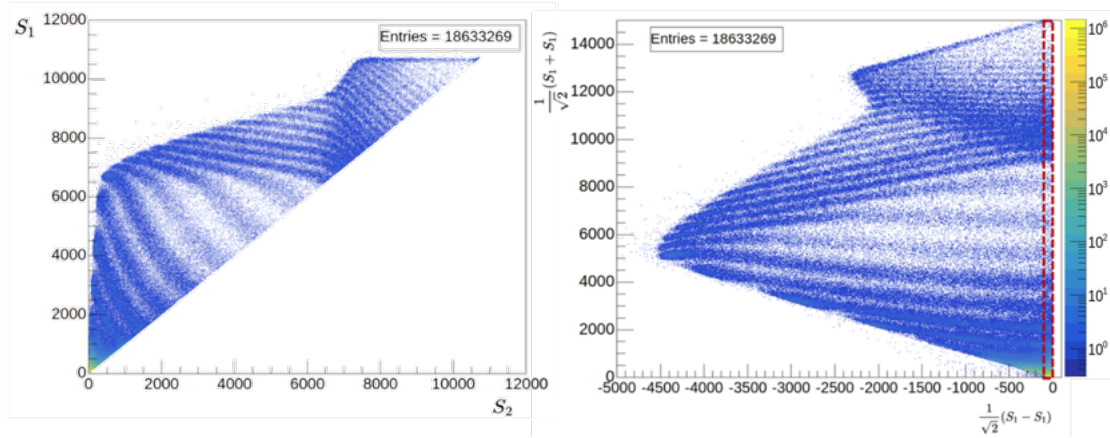


Figure (4.25) – The s_1 versus the s_2 distribution (left) and its rotation counterclockwise by 45° (right).
The red box delimits the region around $\eta = 0.5$.

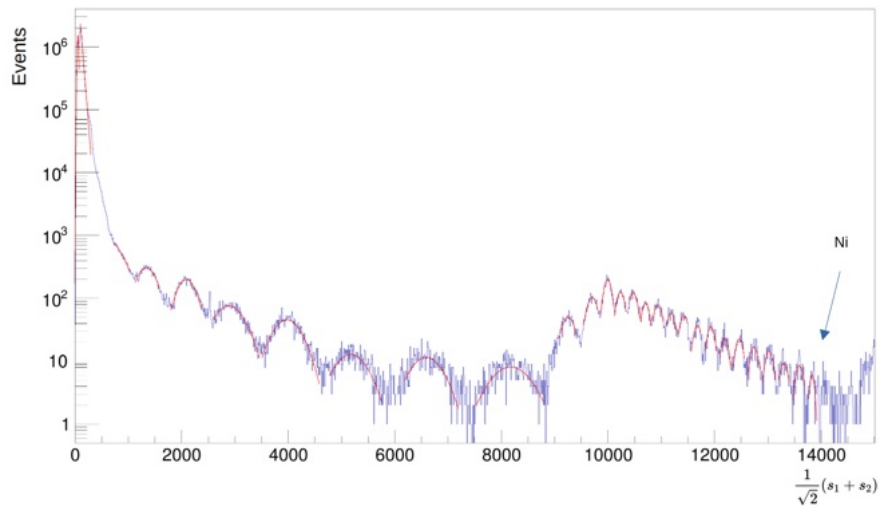


Figure (4.26) – The projection of the area within the red rectangle in Figure 4.25 onto the vertical axis.

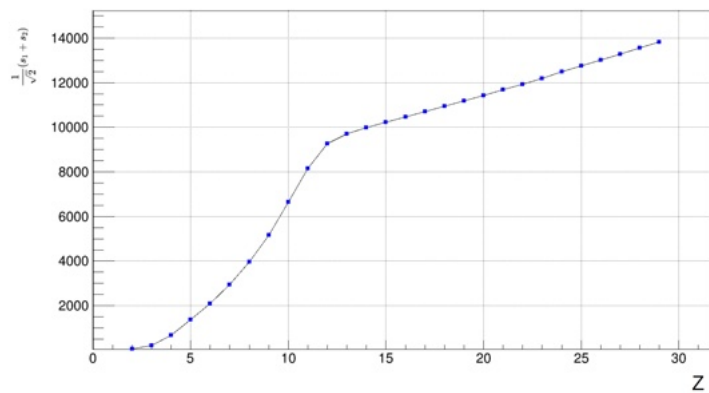


Figure (4.27) – The $\frac{1}{\sqrt{2}}(s_2 + s_1)$ versus Z plot for the LO ladder.

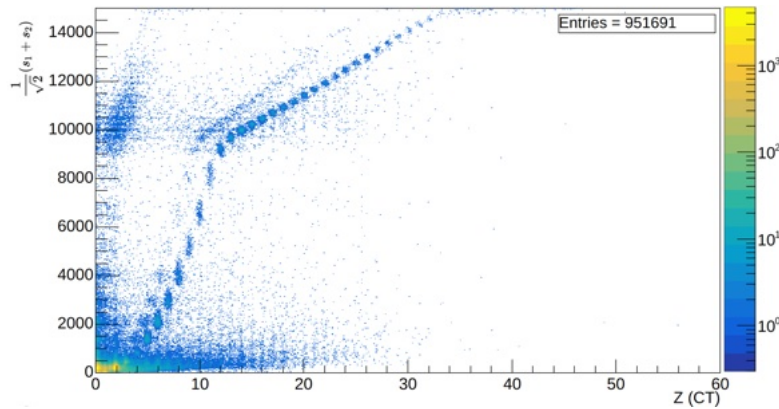


Figure (4.28) – $(s_1 + s_2)/\sqrt{2}$ signal from L0 vs the external Z measurement from the independent Charge Tagger.

distribution in fig.4.25 yields the distribution represented in Fig.4.26: the peaks from left to right correspond to ions with gradually increasing charges measured from the beam. It can be seen that the L0_10 detector (ladder) is capable of identifying ions up to nickel. By performing Gaussian fitting on the peaks in this figure, the peak value of different charges can be obtained and correlated to the Z value, as presented in fig.4.27. A clear change in the detector response at high Z values is visible starting with Z=12: the functional dependence of the signal to charge is not anymore quadratic but becomes linear, this allows to identify charges as high as Z=30 within the dynamic range of the VA. The charge selection has been verified against the measurement in the same events of the CT charge detector, as shown in figure 4.28 where the L0 ladders signal, $(s_1 + s_2)/\sqrt{2}$, is compared with the response in Z from the CT. In this distribution, the same behaviour of the L0 signal vs. Z evaluated in Fig.4.27 is observed and it can also be appreciated complete saturation when the charge exceeds Z=32, since the readout signal no longer increases with the ion charge.

The approach based on s_1, s_2 has proven its feasibility at central η values, and in principle could be extended characterising the charge peaks in different *slices* of Fig.4.27. However, it could be really impractical since the changes in the $(s_1 + s_2)$ distribution with $(s_1 - s_2)$ should be described with high granularity, i.e. in tiny $(s_1 - s_2)$ intervals, and this could result in a statistical limitation of the approach, that would be unfeasible in flight.

Multivariate approach for charge measurement

To overcome the limitations of the charge reconstruction approach presented beforehand, a Machine Learning (ML) [99] based analysis was adopted. In particular, the choice was to use a combination of the Random Forest, RF classification (sometimes improperly referred also as BDT, Boosted Decision Tree) with the Support Vector Machine, SVM, model. SVM has been used to map the inputs to a high-dimensional feature space, while the second is used to provide a sort of “feedback” to the first one, in an iterative procedure. The model is fully *supervised* [100] since the Charge Tagger, CT, has been used to *label* each event used in the training with an external measurement of the charge.

Figure 4.29 shows the model designed and implemented for this thesis work. The events chosen (i.e. the runs) for the training of the model are randomised (A1 yellow box in the Fig.) and filtered (A2 box). The randomisation process is used to prevent that an event sequence due to the fragmentation of the beam along the beam line (namely: each high-Z event being followed by a prompt low-Z event generated by the fragments of the previous one) could influence the SVM part. The filtering process, based on the CT information, is used to equalize, as much as possible, the different input charges, since the beam is naturally more abundant towards lower Z values. After this filtering part, the events used in training are 81757: the choice was to not to use the fully acquired statistics to not *overtrain* the model.

From each event, 9 quantities, *features*, measured by the detector under test were identified. The chosen features are:

- the total signal of the largest cluster in each event;

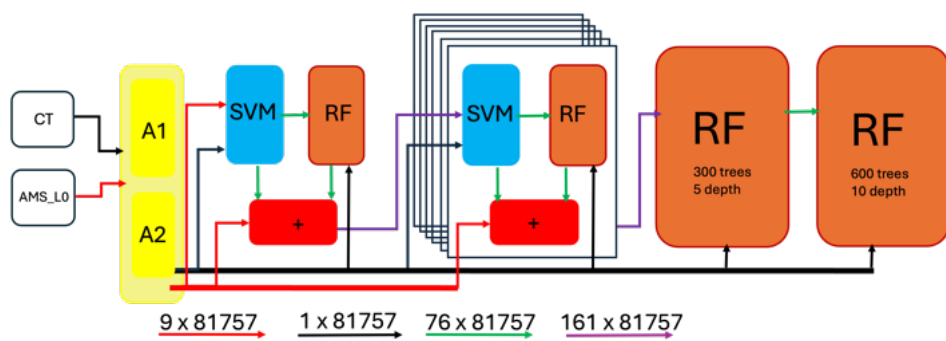


Figure (4.29) – Model design diagram for the implemented machine supervised learning.

- the signals of the three strips with largest signal in that cluster;
- the position of the three strips with largest signal;
- the η value;
- the total number of strips forming the cluster.

In addition to these features, for the training only, the CT measured charge has been used.

The SVM part is used to map the input features on a hyperplane needed for classification, defined in a 76 dimensional space. Dimensions of the space correspond to the Z=1 to 75 charge values with enough event statistics and that will be possible classify as "true", and includes the "null" charge value, i.e. 0, for possible misidentifications. In brief, the SVM computes the distance to the hyperplane, based on the set of features value for each event. A set of 76 values (corresponding to the distances) will become the new feature values. The purpose of this part is to generate more refined feature vectors, starting from the basic features directly from the detector.

To provide feedback to the SVM and optimize the hyperplane definition (e.g., improve robustness), the features generated by the SVM are also mapped as new features through the RF part that, given the input 76 features, classifies each event to 76 classes (i.e. the output is a vector containing 76 values that are proportional to the probability, for that event, of having such features if coming from each one of the 76 possible input charges).

The original 9 features, plus the 76 out from the SVM part and the 76 out from the RF part are then combined, for a total of 161 feature values.

After the initial step, where the SVM is fed with 9 features, the same combination of SVM and RF is iterated for additional 6 times to improve the power of the model. While the RF part is essentially the same for all the 7 iterations, the SVM for the last 6 is fed with all the 161 features from the previous step. The depth of the iteration procedure has not deeply studied in details, but the number of iterations has been optimized on empirical base.

An example of the output of the SVM+RF part is presented in Fig. 4.30: each bin, Z , essentially contains the probability, for an ion with charge Z , to give the particular set of features used as input to the classifier.

The final supervised learning section consists of two Random Forest models. The use of two models, with different numbers of trees and depths, has been adopted to reduce the risk of over-fitting and under-fitting. Also in this case, the optimisation of the

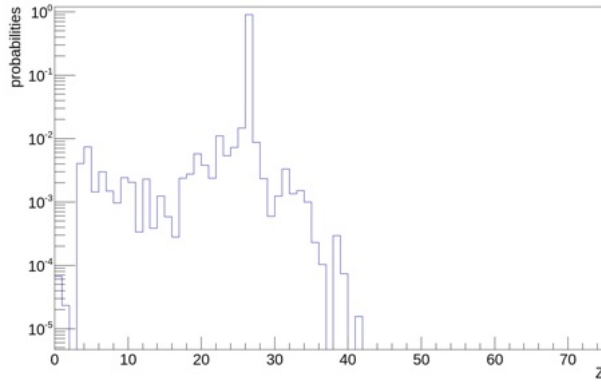


Figure (4.30) – Example of the classification, from the SVM+RF part, in the chosen 76 classes: each bin, Z , contains the probability, for an ion with charge Z , to give the particular set of features used as input to the classifier.

parameters, for the reduction of over- and under-fitting has been evaluated on empirical base and a deep study was not performed.

The output of this last section is still a vector of 76 values, similar to the output of the SVM+RF part presented in Fig. 4.30. Several choices can be done to combine this 76 values into a single value to be used as *measured Z*: quoting the charge corresponding to the higher value in the vector, quoting the average of the values, quoting a probability to be a certain ion (this in general requires, in the probability inversion using the Bayes' theorem, to have an estimate of the a-priori probability to be that certain ion), or other

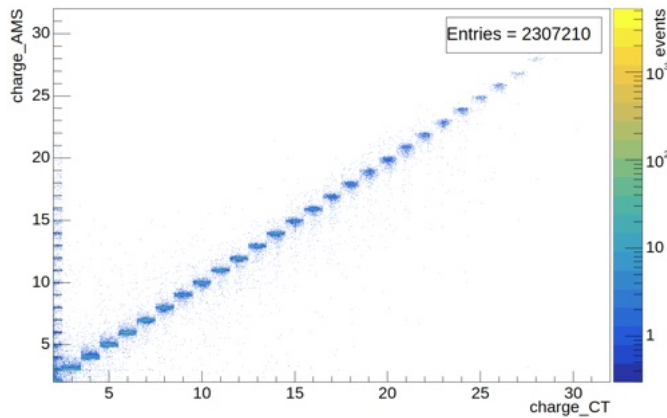


Figure (4.31) – Charge measured by the AMS-L0 sensor using a ML approach as a function of the one measured by the CT.

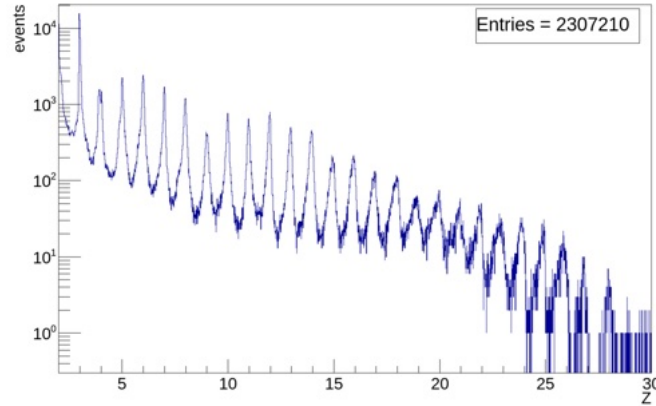


Figure (4.32) – Distribution of the charge measured by the AMS-L0 sensors using a ML approach.

choices, but for this thesis work the choice was to use a simple average of the values. One could also use the standard deviation of the values as estimate of the uncertainty of the result, but this has not been studied in details.

Figure 4.32 and Figure 4.31 show the test made on a test sample containing ~ 2.5 M events. Figure 4.31 shows the comparison with the Charge Tagger and should be noted as low-Z x -axis bin contains, on y , charges, measured by the AMS sensor, up to around 20: this must not be considered as a misidentification of the classifier, but to the reduced size of the Charge Tagger that, for part of the total sample, only measured a fragment or a δ -ray particle and not the high-Z primary ion. Figure 4.32 is a projection, on the y -axis, of the previous plot, and shows as in the distribution of the measured charges all the peaks are well separated, up to a charge of around 30.

4.2 HERD-SCD beam tests

As described in Chap. 2, the Silicon Charge Detector (SCD) is the outermost sub-detector of the HERD instrument. It consists of five units, each composed of eight layers of orthogonally placed single-sided silicon microstrip detectors, which encase the other sub-detectors surrounding the calorimetric core. The SCD is designed to measure the absolute charge of incoming particles, before their possible fragmentation in other detectors, and to reconstruct the trajectory of the incoming particles together with the FIT .

In the fall of 2023, a beam test campaign with single charged particles and heavy ions was conducted at CERN. This was the first beam test with all the HERD sub-detector prototypes, disposed along the beam arrival direction in order to replicate the incident path of cosmic rays once in flight. Figure 4.33 shows the setup used during the tests at the SPS H4 beamline.



Figure (4.33) – The setup of fall 2023 HERD beam test at the CERN SPS H4 beam line.

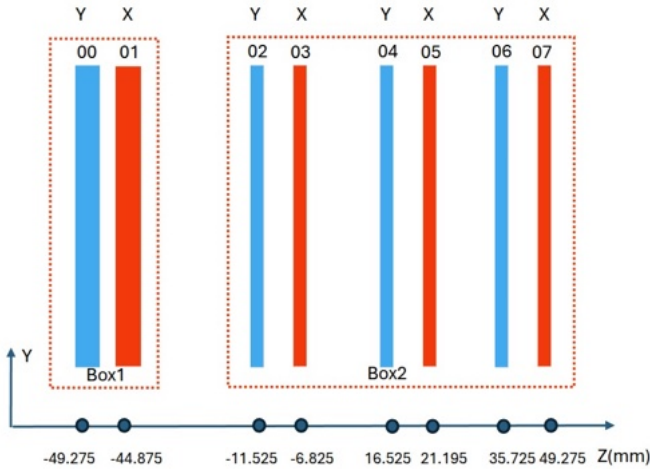


Figure (4.34) – Arrangement of SCD-IT prototypes during the fall 2023 HERD beam test: a first box with two (1 x and 1 y modules) 300 μm thick silicon sensors and a second box with six (3 x and 3 y modules) 150 μm thick ones.

As shown in Figure 4.33, along the beam direction, the following sub-detectors are arranged in sequence: a plastic scintillator acting as main trigger, the Italian prototype for the SCD (SCD-IT), the Chinese SCD prototype (SCD-CN), the Chinese PSD prototype (PSD-CN), the Italian PSD (PSD-IT), the FIT prototype, and the CALO one (with both the CMOS and the PhotoDiode read out). All the detectors are triggered by the same trigger logic, share a synchronised DAQ and, in general, data were acquired simultaneously such to allow for combined data analysis. The goal of the beam test was to measure the performances of the different sub-detectors while operating all the detectors in a common data acquisition.

For the SCD, the beam test was relevant to measure the charge measurement performance, mainly, as well as the spatial resolution. The SCD-IT and SCD-CN prototypes have different designs, involving different sensor thicknesses, different implant pitches, strip widths, different numbers of floating strips, and different decoupling capacitors in the readout chain. This thesis work will focus only on the test results of the SCD-IT. In the following we will then refer to it simply as SCD.

As shown in Figg. 4.34 and 4.35, the Italian SCD prototype consists of eight single-sided Silicon Strip Detectors (SSDs). These eight SSDs are installed in two boxes with the strip directions in orthogonal arrangement so to have a tracker able to measure, with similar accuracy, both the x and y coordinates. The two SSDs in the first box have a thickness of 300 μm , while the six SSDs in the second box have a thickness of 150 μm . Apart the difference in thickness, the SSDs in both boxes have the same structure. Each

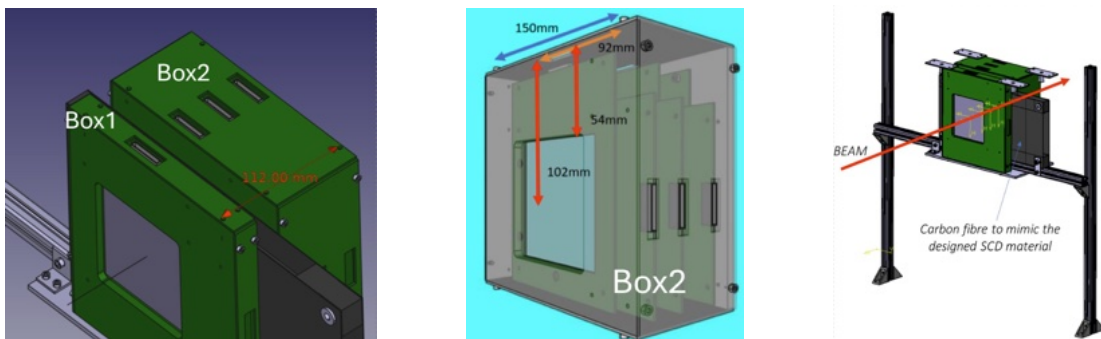


Figure (4.35) – Arrangement of SCD-IT prototypes during the fall 2023 HERD beam test: (left) detail, from the CAD drawing of the setup, of the two boxes, (center) CAD drawing of the Box2 with the view of the sensors inside, (right) the two boxes on the mechanical structure to hold them, aligned with the beam.

SSD measures $96 \times 96 \text{ mm}^2$ and has 640 readout strips with a readout (implant) pitch of $150\mu\text{m}$ ($50\mu\text{m}$), with two intermediate strips between every two readout strips.

Figure 4.36 and 4.37 illustrate the DAQ system of the SCD. As shown in the figure, the 640 readout strips of each silicon microstrip sensor are read out by 10 VAs (IDE1140) located on a Hybrid board close to the sensor, with each VA devoted to 64 readout strips. Digitization is performed in a separate board, the ADC board, reading the analog signals from two Hybrid boards. To improve readout live-time ensuring that the maximum dead time is kept below 500 microseconds, each ADC board is equipped with 10 12-bit ADCs. Each ADC digitises the analog signals from two VAs and transmits them to the DE10Nano board, which is directly mounted on the ADC board. The DE10Nano board [101] is a commercially available board featuring an Intel Cyclone V System-On-Chip, which combines an Intel FPGA with a Cortex-A9 ARM-based hard processor system (HPS) CPU. The Cyclone V handles the IDE1140s and ADCs through



Figure (4.36) – Detail of the SCD-IT DAQ system: sensor and Hybrid board (left), DE10Nano board (center), ADC board (right).

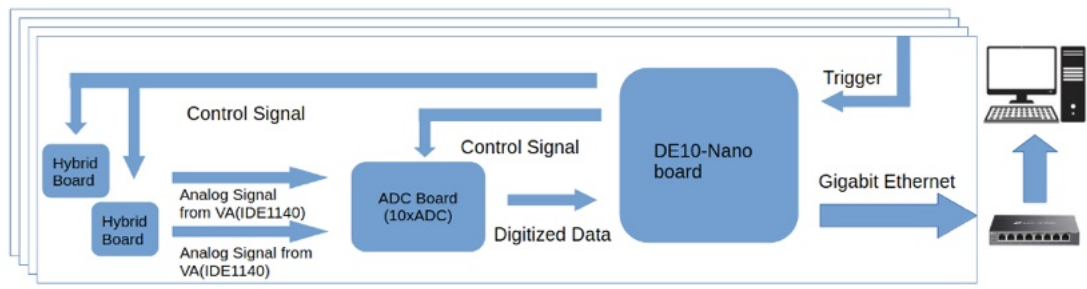


Figure (4.37) – Scheme of the SCD-IT DAQ system.

its FPGA component and communicates with the higher-level DAQ system using its CPU component via the board 1 Gbps Ethernet connection.

4.2.1 Beam test with electrons

The study of the HERD response to electrons was part of the beam campaign focussed to study the CALO performance in measuring electromagnetic showers. At the same time, however, the 243 GeV electron beam was used to study the performances of the SCD-IT with unitary charged particles. As already pointed out in the discussion of AMS-L0 tests, dealing with a unit charge particle means to be in the lowest signal-to-noise (S/N) ratio measurement conditions, i.e. worst case for detection efficiency and spatial resolution. This is particularly relevant for SCD-IT where the signal amplitude in sensors of different thickness, 150 and 300 μm , was studied.

Calibration & S/N performance

Raw data reduction is naturally the first step in the data analysis: the readout of all SCD channels is processed to extract the few strips with the signal from interacting particles. Common noise, pedestal, noise levels were evaluated according the procedures described in Chap. 4.1.1 and examples of the results are presented in Figures 4.38 and 4.39 showing the typical pedestal (left) and noise (right) for a 300 μm and a 150 μm thick sensors respectively. The two sensors show similar pedestal values (300-400 ADC counts) and noise levels (~ 2 ADC counts), however half of the energy deposition is expected for a particle passing through the thinner silicon, such that the S/N level for unitary charges will be depressed, possibly leading to inefficiencies in the thinner sensor.

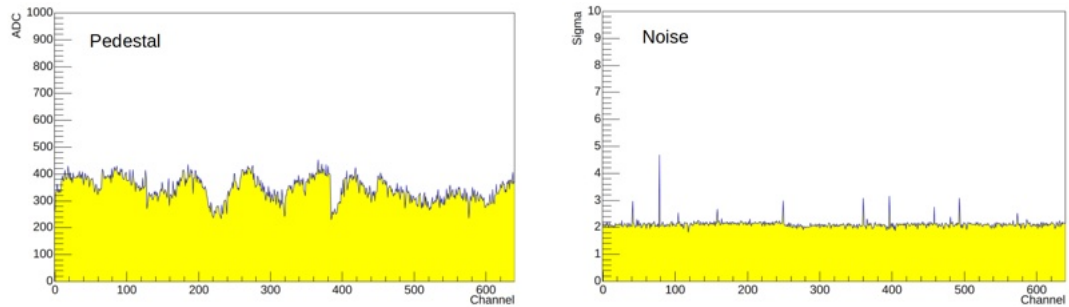


Figure (4.38) – Pedestal (left) and noise (right) of a SCD 300 μm thick sensor.

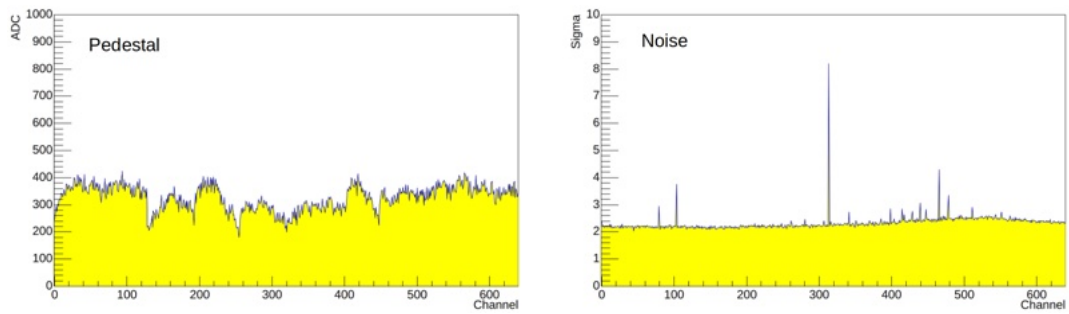


Figure (4.39) – Pedestal (left) and noise (right) of a SCD 150 μm thick sensor.

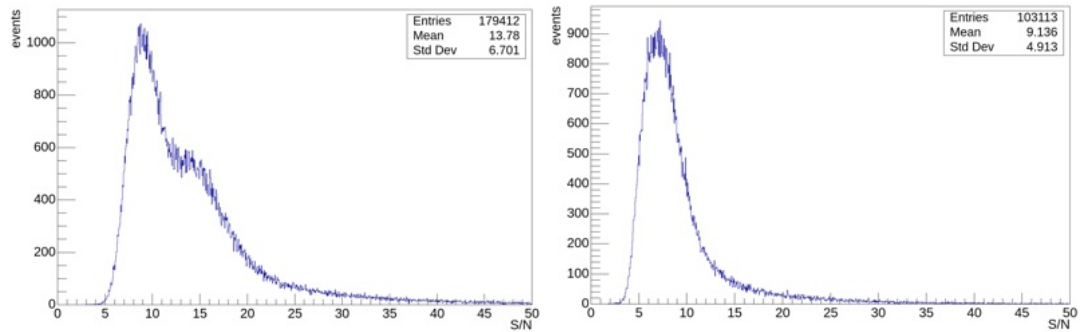


Figure (4.40) – S/N distribution for 300 μm (left) and 150 μm (right) detector thicknesses.

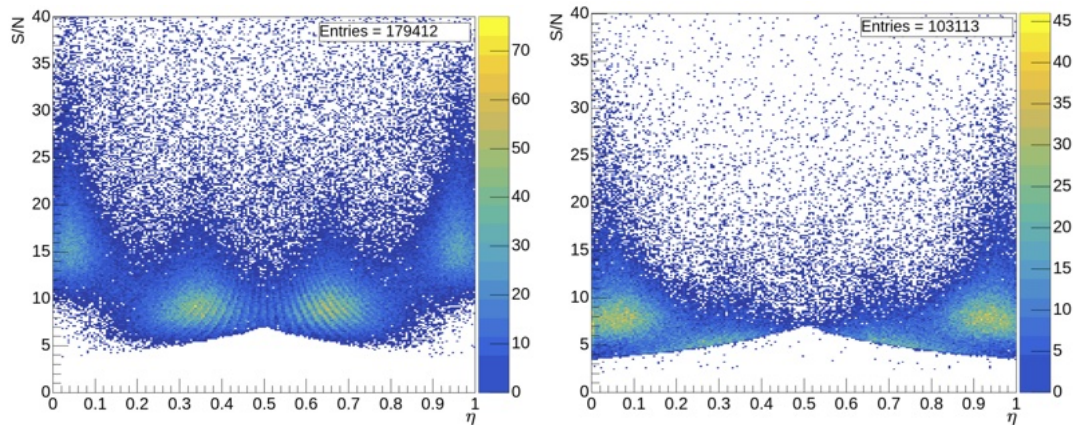


Figure (4.41) – S/N distribution vs η for 300 μm (left) and 150 μm (right) detector thicknesses.

When comparing calibration values with those presented for AMS-L0 sensors beforehand (Fig.4.8,4.9), the different meaning of the ADC units should be taken into account. Both AMS-L0 and SCD-IT have the VA chip as charge amplifier and the analog signal in output from the sensors has the same dynamic range. Conversely the digital units after conversion have different sensitivity for the two readout systems. The conversion to digital units is performed by a 14-bit ADC in L0 and 12-bit ADC in SCD. This 2-bit difference implies that one digital unit in SCD-IT readout corresponds to $2^2 = 4$ times that of AMS-L0. As an example, typical SCD pedestals are ~ 400 ADC counts, whereas AMS-L0 are close to ~ 1600 ADC counts. Both AMS-L0 and SCD exhibit a single strip noise level of ~ 2 ADC counts, but should be kept in mind that this directly translates to a factor 4 larger noise in SCD with respect to AMS-L0. This could be due to the different approach in the digitization. In the AMS-L0 prototypes, as well as in the flight modules, the ADC is physically placed on the very same electronic board, the LEF, with just few mm long PCB traces to connect it to the ASICs. In the SCD prototypes the ADC board is connected by a 20-30 cm long cable to the hybrid circuit hosting the VAs, and this could cause some noise pickup. We therefore expect a lower efficiency in detecting unitary charged particles in SCD with respect to AMS-L0 for the same requirement (typically $S/N=5$) on the seed strip to identify the cluster.

Fig.4.40 presents cluster S/N distributions as measured for a $300\ \mu m$ (left) and a $150\ \mu m$ (right) SCD sensor. As a general figure of merit, the most probable value (MPV) of the S/N is 5 for the $150\ \mu m$ thick sensor and for a $300\ \mu m$ thickness is ~ 6.5 , not too far away from $MPV\sim 8$ for the L0 sensor. However, other features should be taken into account.

Starting from the same beam events statistics, the number of events with a reconstructed cluster on the thinner sensor is $\sim 57\%$ of the thicker one. That means that for $\sim 43\%$ of the events the request of a $S/N \geq 5$ on the seed strip suppresses cluster reconstruction in the thinner sensor, i.e. what is observed is just part of the original distribution whose $MPV < 5$. On the thicker sensor a structure is also observed at $S/N \sim 10$. Looking at the S/N distribution versus η , shown in Fig.4.41 we can observe peculiar structures. On the $150\mu m$ thick sensor clusters are mostly reconstructed near the $\eta = 0, 1$ regions whereas the central η region is depleted, meaning that when the charge is nearly equally shared among two readout strips, the signal value on the single strip is too low with respect its noise to satisfy the cut on the minimum S/N to trigger the cluster reconstruction. On the $300\ \mu m$ thick SCD sensor clearly appears that the structure at $S/N \sim 10$ is related to clusters close to $\eta = 0, 1$, whereas the bulk of the S/N distribution is at the intermediate η values, peaked in correspondence to the floating strip regions,

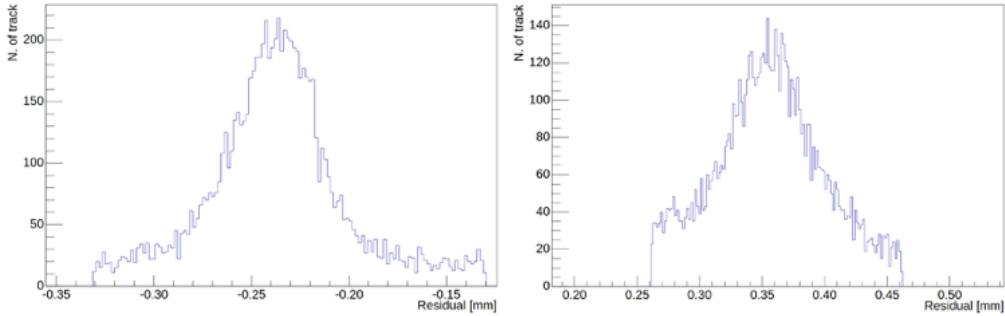


Figure (4.42) – Distribution of the unbiased residuals for a $300\text{ }\mu\text{m}$ (sensor 01, left) and a $150\text{ }\mu\text{m}$ (sensor 03, right) detector, before the alignment procedure.

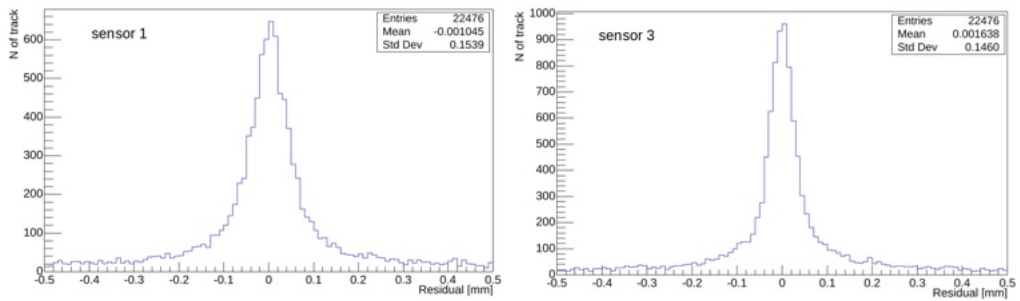


Figure (4.43) – Distribution of the unbiased residuals for a $300\text{ }\mu\text{m}$ (sensor 01, left) and a $150\text{ }\mu\text{m}$ (sensor 03, right) detector, after the alignment procedure.

and with a lower S/N as more signal is shared on more strips and charge is partially lost on backplane.

Alignment & Spatial resolution

As in the L0 analyses, see Sec. 4.1.1, the spatial resolution of the detectors under test is evaluated by the distribution of unbiased residuals, namely the difference between the reconstructed position and the prediction from independent tracking with other sensors. As a first step, the eight detector layers have been aligned and in Fig. 4.42 and 4.43 the unbiased residual plots for a $300\text{ }\mu\text{m}$ and a $150\text{ }\mu\text{m}$ (sensor 03) detectors before and after alignment are reported as an example.

As discussed earlier, see Eq. 4.1, the accuracy of the tracking telescope is needed to measure the intrinsic resolution from the unbiased results. Since, in the case under study, all the detectors are similar and with an unknown spatial resolution, the first estimate can be done only with an a-priori estimate of the intrinsic resolution of the single module. Given an implant pitch of $\sim 50\text{ }\mu\text{m}$, we expect a resolution of $50\text{ }\mu\text{m} / \sqrt{12} \sim 15\text{ }\mu\text{m}$.

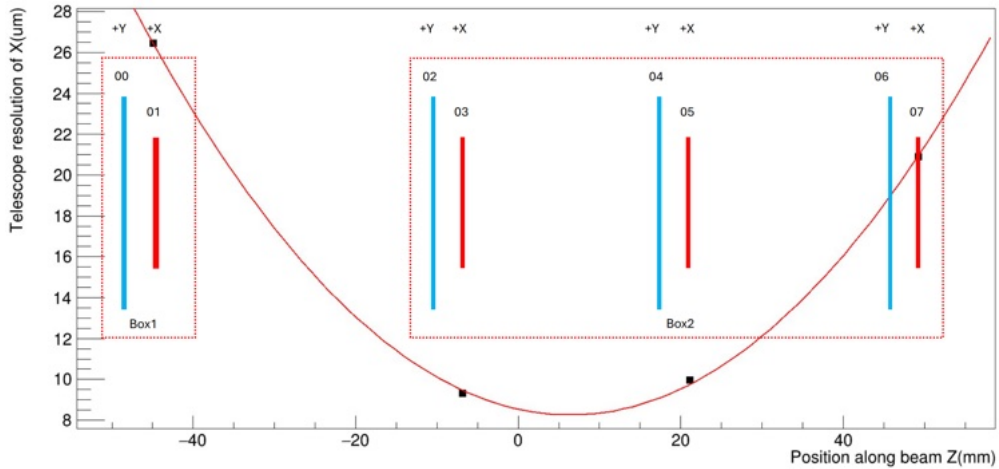


Figure (4.44) – Accuracy of the trajectory reconstructed by the tracking telescope (x coordinate) along the z coordinate of the telescope itself.

Figure 4.2.1 is a schematic diagram of the accuracy of the trajectory reconstructed by the tracking telescope (x coordinate) along the z coordinate of the telescope itself. The two chosen, as examples, sensors are in a z position where the effect of the tracking itself is expected to be $\sim 26 \mu\text{m}$ (sensor 01) and $\sim 9 \mu\text{m}$ (sensor 03).

By combining the accuracy of the reconstructed trajectory with the unbiased residuals of the detector, the intrinsic spatial resolution of the detector can be obtained using Equation 4.2.

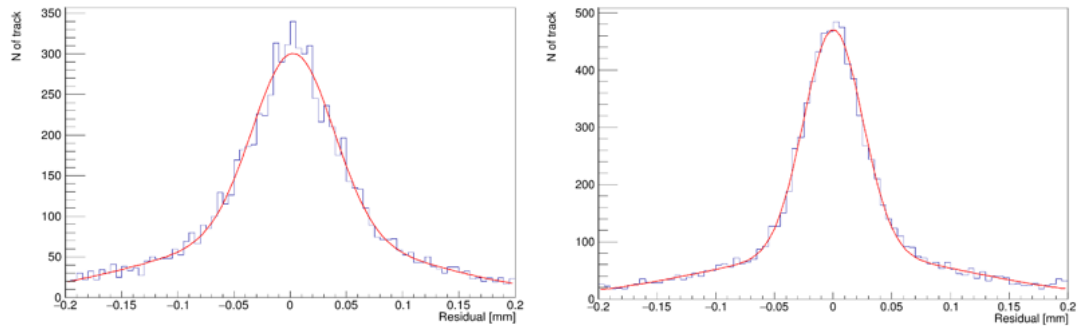


Figure (4.45) – Fit with two gaussians to the unbiased residual distribution of sensor 01 (left) and sensor 03 (right). The fit to sensor 01 yields to the contribution of two gaussian with, respectively, $\sim 36 \mu\text{m}$ and $\sim 120 \mu\text{m}$. The fit to sensor 03 yields to the contribution of two gaussian with, respectively, $\sim 25 \mu\text{m}$ and $\sim 113 \mu\text{m}$.

Figure 4.45 shows the result of a two-gaussian fit to the unbiased residual distributions for sensor 01 and sensor 03. The fit to sensor 01 yields to the contribution of two gaussian with, respectively, $\sim 36 \mu\text{m}$ and $\sim 120 \mu\text{m}$. The fit to sensor 03 yields to the contribution of two gaussian with, respectively, $\sim 25 \mu\text{m}$ and $\sim 113 \mu\text{m}$.

The standard procedure to extract the spatial resolution, as discussed in Sec. 4.1.1 would be to quote a single standard deviation, as weighted average of the standard deviations of two gaussians, where the weight is the relative contribution, to the residual distribution statistics, of the two populations. The relative contribution of the wider gaussian, for both the types of sensors, is quite large and this yields to a quite large combined standard deviation (for the two chosen sensors: $\sim 66 \mu\text{m}$ for sensor 01 and $\sim 51 \mu\text{m}$ for sensor 03). When subtracting the effect of the tracking telescope resolution by using Eq. 4.2, this yields to an estimated resolution that is much larger than the assumed $15 \mu\text{m}$ one, and that is significantly different between $300 \mu\text{m}$ and $150 \mu\text{m}$ thick sensors. The estimation using Eq. 4.2 must be repeated, iteratively, rescaling the extrapolation error shown in Fig. by the ratio between the estimated intrinsic resolution and the assumed a-priori one. This yields to $\sim 35 \mu\text{m}$ for the thicker sensors and $\sim 45 \mu\text{m}$ for the thinner ones.

If we, instead, assume that the wider gaussian is due to a poor track selection (the telescope in each coordinate is done with only 4 layers, using one as detector under study we end up with tracks with only 3 points, that mean χ^2 evaluations with a degree of freedom of only one). Repeating the iterative estimated discussed above with only the narrower gaussian yields to an intrinsic resolution of $\sim 18 \mu\text{m}$ for the thicker sensors and $\sim 21 \mu\text{m}$ for the thinner ones. This is much more compatible with the $\sim 15 \mu\text{m}$ from first principles and more coherent between the two kind sensors. Typically, when a particle passes through a thicker sensor, the higher deposited energy leads to a higher signal-to-noise ratio and thus better spatial resolution. The effect, anyhow, is expected to be quite limited.

Compared to the AMS02-L0 prototypes, can be observed that even if the SCD-IT detectors have a similar size of the AMS02-L0 single sensors detectors, its spatial resolution is significantly worse. This difference is mainly due to two factors. First, they have different electronic readout systems, with the SCD-IT having noticeably higher noise. Second, their silicon microstrip detectors are remarkably different: the SCD-IT has two intermediate strips, with a wider readout pitch ($150 \mu\text{m}$) and, more important, implant pitch ($50 \mu\text{m}$).

For the SCD-IT a wider readout pitch, which allows for fewer readout strips in the same area, was chosen, since its spatial resolution requirements are lower. Unlike AMS

tracker, which is required to measure particle rigidity through a magnetic field, the final version of the SCD, when operating in orbit, only needs to provide a rough estimate of the incident tracks into the CALO (the segmentation of the HERD CALO is $3 \times 3 \times 3 \text{ cm}^3$). Moreover, having fewer readout strips significantly reduces its energy consumption.

4.2.2 Test with heavy ions

As described in Sec. 4.1.2, also the for HERD ion beam test, a Lead primary beam, fragmented on a 4 cm beryllium target has been used. The resulting beam contains all the ions with atomic numbers (Z) from 1 to 82.

Before proceeding to the evaluation of the charge measurement performance, the VA equalisation procedure described in Sec. 3.4.4 is required.

Figures 4.46 and 4.47 show the signal of the seed strip as a function of the VA number corresponding to the particle impact point. There 80 VAs are grouped per sensor (10 VAs per sensor) and the different vertical distribution for each sensor is due to the limited width of the beam. It can be observed as after the equalisation, the MIP peaks corresponding to the same charged particles, as measured by all VAs are aligned at the same level.

As for the AMS-L0, the reference distribution for the charge measurement is the distribution of total cluster signal as a function of η , see the Figure 4.48. As before, a $300\mu\text{m}$ (sensor 01) and a $150\mu\text{m}$ (sensor 03) sensors are taken as example. Only the clusters with the largest signal detected by each sensor for each event are included in

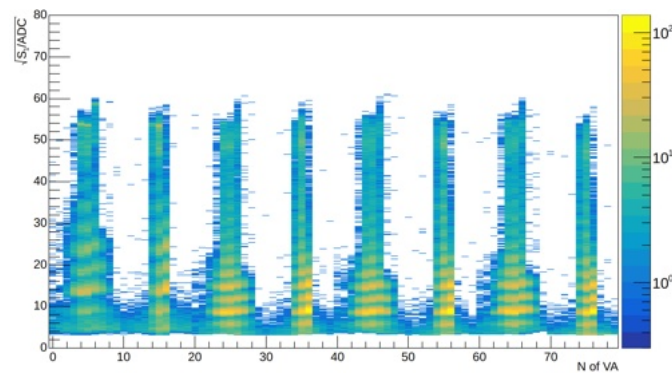


Figure (4.46) – Signal of the seed strip as a function of the VA number corresponding to the particle impact point, before VA equalisation. There 80 VAs are grouped per sensor (10 VAs per sensor).

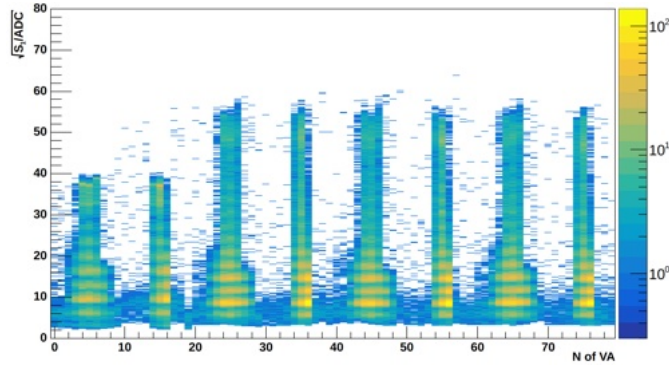


Figure (4.47) – Signal of the seed strip as a function of the VA number corresponding to the particle impact point, after VA equalisation. There 80 VAs are grouped per sensor (10 VAs per sensor).

the statistics.

From Figure 4.48, also if compared with AMS-L0 similar plot Fig. 4.21 we can easily see four things: a) the distribution of the different ions is quite different with respect to the AMS beam test, b) the peaks of the different charge ions are clearly visible, c) after around charge 7-8 the peaks start to be not anymore separated, d) the effect of the signal loss to the back plane is more pronounced on the thinner detector.

The first point, a), is simply due to a different tuning of the beam transport line: even with the same primary beam, fragmented on the very same target, one can tune the beam transport line (namely selection a certain A/Z value to be preferred) to enhance or suppress the high Z 's. In the HERD beam test the beam was better tuned, with respect to the AMS-L0 one, to enhance the high Z part of the beam.

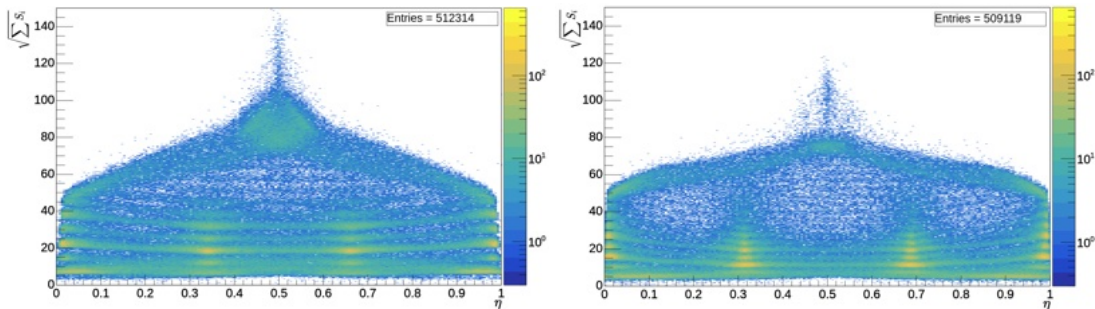


Figure (4.48) – Distribution of the total cluster signal as a function of η , for a $300\mu\text{m}$ (sensor 01, left) and a $150\mu\text{m}$ (sensor 03, right) taken as example.

As discussed for AMS-L0, see Sec. 4.1.2, for charges around 10, the saturation of the single VA channels start to heavily deformate the η distribution. Nevertheless, below the saturation, the peaks are well separated and a good charge resolution is observed. Figure 4.49 shows the distribution of the total cluster signal plots for the very two sensors discussed above. The plots, as in the AMS-L0 case, has been divided into *readout strip position* and *floating strip one*. While the former can be selected with the very same η request (i.e. around 0 or 1), the latter, in the SCD case of two intermediate strips, reflects to a selection on the corresponding η regions (i.e. around 0.32 or 0.68). From the comparison of the different distributions is clear how the $150\mu\text{m}$ thick sensors can identify peaks at slightly higher charges with respect to the $300\mu\text{m}$, and how this higher dynamic range is present for η values corresponding to intermediate strips, as shown in the AMS-L0 case. On the contrary, the more pronounced signal loss toward the backplane, for the $150\mu\text{m}$ thick sensor, is so important that the $Z=1$ peak is not clearly visible when dealing with intermediate strips.

As said, differently from AMS-L0, for the HERD SCD prototypes is clear how the saturation become crucial after $Z \sim 10$, at the single level strip. Even if this is also the case

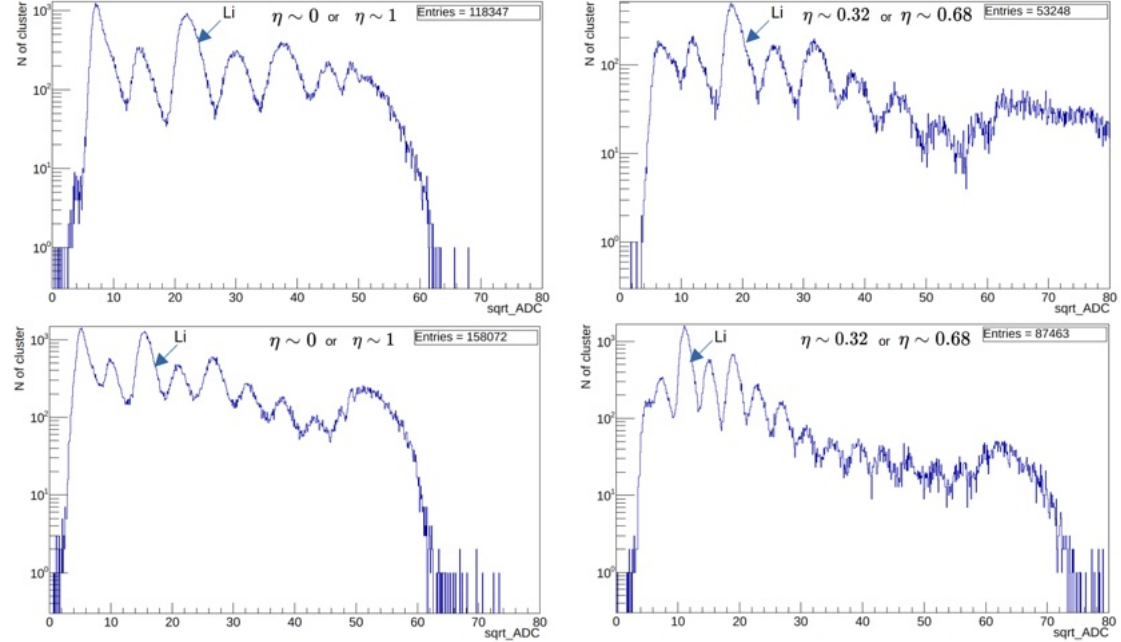


Figure (4.49) – Distribution of the total cluster signal for a $300\mu\text{m}$ (sensor 01, top) and a $150\mu\text{m}$ (sensor 03, bottom). The distribution has been divided into readout strip position (left) and floating strip one (right). The Lithium peak has been underlined for reference.

for the AMS-02 modules currently operated on the International Space Station [102], and the results of AMS-02 demonstrated how analysis strategies involving all the channels of the cluster can recover the charge information lost by the saturation of the central ones, the possibility to have an estimate of charge only by looking at the total cluster signal is a very key and interesting feature. The origin of this improved performance, for the AMS-L0 sensors, is clearly on the 14-bit ADC. For the flight modules of the SCD is clear how the choice will be to adopt the very same kind of improvement or maybe to even explore the possibility of a 16-bit ADC.

Since, differently from AMS-L0, no special treatment has been studied to recover the high Z part of the distribution, the next step is to apply the η correction discussed in Sec. 3.4.3, to flatten the measured total signal in the cluster and make independent from η itself. Figure 4.50 shows the cluster integral as a function of η , after η correction, for the two sensors chosen as example. To better guide the eye the y-axis has been scaled to be directly in charge units (i.e. Z).

Given the beam test setup of the SCD-IT prototype, we have eight independent measurements of the same particle Z . The combination of the different measurements is a relevant exercise toward the design of the final SCD detector and to estimate its performances. By discarding the maximum and minimum values and averaging the remaining six measurements, the particle charge is obtained as truncated mean. Figure 4.51 shows the obtained distribution.

By fitting each peak in Figure 4.51 with a Landau function, we can obtain the peak value and peak width for each one. Figure 4.52 illustrates the charge resolution of the SCD-IT as a function of the particle's charge when VA is not saturated.

From Figure 4.52, it can be seen that as the charge increases, the charge resolution

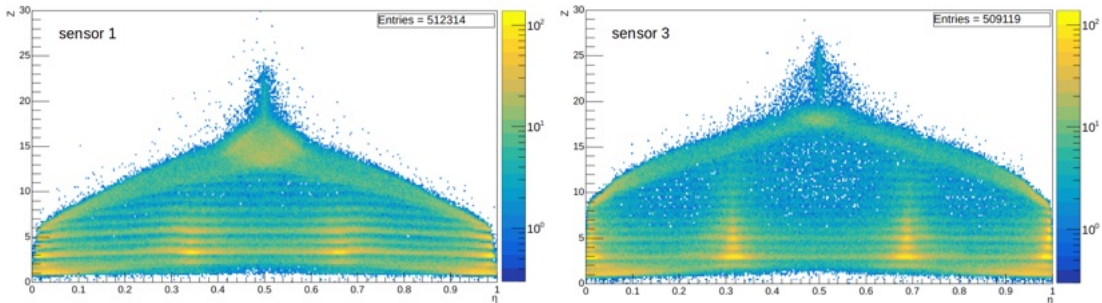


Figure (4.50) – Distribution of the total cluster signal, scaled to charge units, as a function of η , for a $300\mu\text{m}$ (sensor 01, left) and a $150\mu\text{m}$ (sensor 03, right), after η correction.

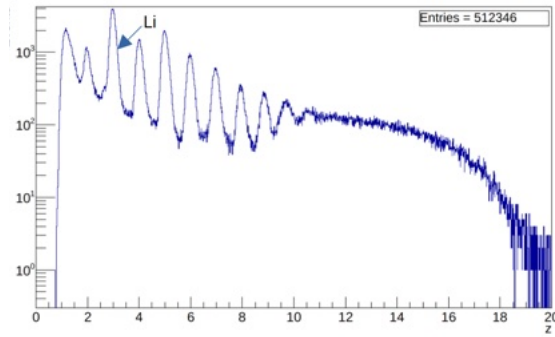


Figure (4.51) – Distribution of the truncated mean of the charges measured by the 8 sensors in the SCD beam test setup.

gradually improves due to the increase in the signal-to-noise ratio. However, due to the decrease in the statistics of the high Z 's, the error on the charge resolution estimate also gradually increases.

It is important to note that the current SCD-IT prototype is still in the preliminary design stage. The prototype used in this beam test consists of only eight layers of single silicon microstrip detectors ($96 \times 96 \text{ mm}^2$).

Conversely, the flight version of the SCD, similarly to the AMS02-L0 flight modules, will be composed of long silicon microstrip detectors, *ladders*, made up by several (~ 10) sensors connected between themselves and to the Front End electronics via a daisy chain approach. All the experience and the performances measurements gathered both with the SCD single sensor prototypes and with the AMS-L0 ones, during this thesis

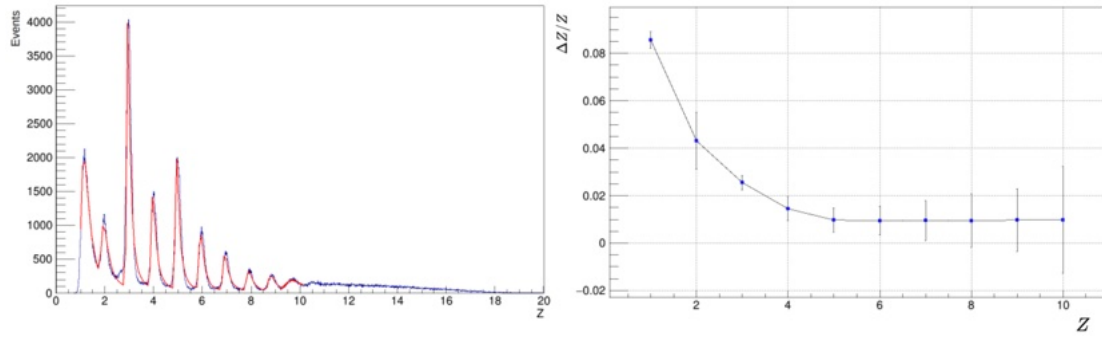


Figure (4.52) – Distribution of the truncated mean of the charges measured by the 8 sensors in the SCD beam test setup, fitted with Landau functions (left). Charge resolution (width of the Landau divided by the corresponding Z , i.e. the MVP value) as a function of the Z (right).

work, will be crucial to the design of the flight detector. Just to give a couple of examples: the SCD will be surely made by $300\text{ }\mu\text{m}$ thick (rather than $150\text{ }\mu\text{m}$) sensors and will have the ADC directly on the Hybrid Board.

Conclusions

Direct measurement of cosmic rays is essential for studying their origin, acceleration and propagation in the Milky Way, and to search signals of new physics as in DM indirect searches or the quest for nuclear anti-matter. To enhance our understanding of cosmic rays, the last decades have seen different space-based instruments operating in orbit and new ones are being developed, aimed to improve observational precision and expand the accessible energy range.

The upgrade of the AMS-02 detector, operating since 2011 on board the International Space Station, and the HERD experiment planned to operate on the Chinese Space Station are the two on going projects in which the present thesis work was developed. For both experiments, a key point is the choice to instrument large areas with silicon microstrip detectors. To contain the number of readout channels both experiments foresee to operate daisy chained sensors in long detection units, $\geq 1\text{m}$. However, such unit lengths have been never operated before and a careful study of the detectors performances is mandatory prior to the final design.

Even if silicon microstrip detectors represent a well-established technology, on ground and in space, different design details can lead to different performances, as an example possible elements are sensor thickness, the readout pitch and number of floating strips between two readout strips, the biasing scheme, the charge amplifier and the readout approach.

In this thesis, we studied the performances at the single sensor level and sensor detection unit, i.e. a ten sensors ladder for the Layer 0 detector to be installed in the upgrade of AMS-02. This was achieved taking part and analyzing data from beam tests with muons, representative of unitary charge MIPs, and ions from a fragmenting beam of lead on beryllium target, representative of the different nuclear species in CRs. The

position resolution, efficiency and charge identification were studied, pointing out also subtle effects in the bias resistor region for readout strips or dependences from the impact point in the inter-strip region. Calibration and signal selection approaches were validated, and different possible strategies to charge identification were studied.

The same studies were carried on single sensors designed for the Silicon Charge Detector of the HERD experiment. Sensors with $150\mu\text{m}$ and $300\mu\text{m}$ thickness were studied with a beam test campaign using electron and ions. After taking part to the setup and operation of the SCD prototypes, data were analyzed in terms of signal over noise and spatial resolution, as well as charge identification.

Based on our studies, the use of $150\mu\text{m}$ thick sensors is strongly disfavoured due to a quite reduced efficiency and poor spatial resolution in measuring single charged particles, even if they allow for a wider charge identification range. An overall comparison of the SCD performances with the L0 detector, clearly point outs that the AMS-L0 choice to use 14-bit to digitize the analog signal allows a better granularity in ADC units which improves charge separation at high Z. The integration of the ADC directly on the front-end as in AMS-L0 is more effective in reducing the noise component from electronics with respect to the independent ADC board of HERD-SCD. Finally, the choice in AMS-L0 of having more floating strips between the readout ones is clearly an advantage in terms of position resolution.

Bibliography

- [1] H. Dembinski et al. Data-driven model of the cosmic-ray flux and mass composition from 10 GeV to 10^{11} GeV. 2017. arXiv: 1711.11432 [astro-ph.HE]. URL: <https://arxiv.org/abs/1711.11432>.
- [2] H Becquerel. “*Sur les radiations émises par phosphorescence*”. Comptes Rendus 122 (1896), pp. 420–421. URL: https://www.academie-sciences.fr/pdf/dossiers/Becquerel/Becquerel_pdf/CR1896_p420.pdf.
- [3] M. Malley. Radioactivity: A History of a Mysterious Science. EBSCO ebook academic collection. Oxford University Press, USA, 2011. ISBN: 9780199766413. URL: <https://books.google.it/books?id=UPnyfSr-wW8C>.
- [4] C. T. R. Wilson. “*On the Ionisation of Atmospheric Air*”. Proceedings of the Royal Society of London 68 (1901), pp. 151–161. ISSN: 03701662. URL: <http://www.jstor.org/stable/116539> (visited on 09/03/2024).
- [5] T. Wulf. “*Observations of radiation of high penetration power at the Eiffel tower*”. Physikalische Zeitschrift (in German) 11 (1910), pp. 811–813.
- [6] P. Carlson and A. De Angelis. “*Nationalism and internationalism in science: the case of the discovery of cosmic rays*”. The European Physical Journal H 35.4 (Mar. 2011), pp. 309–329. ISSN: 2102-6467. doi: [10.1140/epjh/e2011-10033-6](https://doi.org/10.1140/epjh/e2011-10033-6). URL: <http://dx.doi.org/10.1140/epjh/e2011-10033-6>.
- [7] D. Pacini. Penetrating Radiation at the Surface of and in Water. 2017. arXiv: 1002.1810 [physics.hist-ph]. URL: <https://arxiv.org/abs/1002.1810>.

- [8] V. Hess. On the Observations of the Penetrating Radiation during Seven Balloon Flights. 2018. arXiv: 1808.02927 [physics.hist-ph]. URL: <https://arxiv.org/abs/1808.02927>.
- [9] W. Kolhörster. “Measurements of the penetrating radiation in a free balloon at high altitudes”. Physikalische Zeitschrift (in German) 14 (1913), pp. 1153–1156.
- [10] D. Maurin et al. “A cosmic-ray database update: CRDB v4.1”. The European Physical Journal C 83.10 (Oct. 2023). ISSN: 1434-6052. doi: 10.1140/epjc/s10052-023-12092-8. URL: <http://dx.doi.org/10.1140/epjc/s10052-023-12092-8>.
- [11] M. T. Dova, L. N. Epele, and J. D. Swain. Massive relic neutrinos in the galactic halo and the knee in the cosmic ray spectrum. 2001. arXiv: astro-ph/0112191 [astro-ph]. URL: <https://arxiv.org/abs/astro-ph/0112191>.
- [12] J. Candia, L. N. Epele, and E. Roulet. “Cosmic ray photodisintegration and the knee of the spectrum”. Astroparticle Physics 17.1 (Apr. 2002), pp. 23–33. ISSN: 0927-6505. doi: 10.1016/S0927-6505(01)00131-1. URL: [http://dx.doi.org/10.1016/S0927-6505\(01\)00131-1](http://dx.doi.org/10.1016/S0927-6505(01)00131-1).
- [13] G. T. Zatsepin and V. A. Kuz'min. “UPPER LIMIT OF THE SPECTRUM OF COSMIC RAYS”. JETP Lett. (USSR) (Engl. Transl.) 4 (Aug. 1966). URL: <https://www.osti.gov/biblio/4515382>.
- [14] K.-H. Kampert. “Ultra-High Energy Cosmic Rays: Recent Results and Future Plans of Auger”. AIP Conf. Proc. 1852.1 (2017), p. 040001. doi: 10.1063/1.4984858. arXiv: 1612.08188 [astro-ph.HE].
- [15] R. V. Wagoner. “Explosive Nucleosynthesis”. Astrophysical Journal 151 (July 2002), p. L103. doi: 10.1086/180152. URL: <https://doi.org/10.1086/180152>.
- [16] E. M. Burbidge et al. “Synthesis of the Elements in Stars”. Rev. Mod. Phys. 29 (4 Oct. 1957), pp. 547–650. doi: 10.1103/RevModPhys.29.547. URL: <https://link.aps.org/doi/10.1103/RevModPhys.29.547>.
- [17] K. Lodders. “Solar System Abundances and Condensation Temperatures of the Elements”. The Astrophysical Journal 591.2 (July 2003), p. 1220. doi: 10.1086/375492. URL: <https://dx.doi.org/10.1086/375492>.
- [18] E. Fermi. “On the Origin of the Cosmic Radiation”. Phys. Rev. 75 (8 Apr. 1949), pp. 1169–1174. doi: 10.1103/PhysRev.75.1169. URL: <https://link.aps.org/doi/10.1103/PhysRev.75.1169>.

- [19] K. Olive. “*Review of Particle Physics*”. Chinese Physics C 38.9 (Aug. 2014), p. 090001. doi: 10.1088/1674-1137/38/9/090001. URL: <https://dx.doi.org/10.1088/1674-1137/38/9/090001>.
- [20] A. Bell. “*The acceleration of cosmic rays in shock fronts - I.*” 182 (Jan. 1978), pp. 147–156. doi: 10.1093/mnras/182.2.147. URL: <https://ui.adsabs.harvard.edu/abs/1978MNRAS.182..147B>.
- [21] M. Hoshino. “*Nonthermal Particle Acceleration in Shock Front Region: “Shock Surfing Accelerations”*”. Progress of Theoretical Physics Supplement - PROG THEOR PHYS SUPPL 143 (May 2001), pp. 149–181. doi: 10.1143/PTPS.143.149.
- [22] A. W. Strong, I. V. Moskalenko, and V. S. Ptuskin. “*Cosmic-Ray Propagation and Interactions in the Galaxy*”. Annual Review of Nuclear and Particle Science 57. Volume 57, 2007 (2007), pp. 285–327. issn: 1545-4134. doi: <https://doi.org/10.1146/annurev.nucl.57.090506.123011>. URL: <https://www.annualreviews.org/content/journals/10.1146/annurev.nucl.57.090506.123011>.
- [23] E. Orlando et al. “*GALPROP cosmic-ray propagation code: recent results and updates*”. Nuclear and Particle Physics Proceedings 297–299 (Apr. 2018), pp. 129–134. issn: 2405-6014. doi: 10.1016/j.nuclphysbps.2018.07.020. URL: <http://dx.doi.org/10.1016/j.nuclphysbps.2018.07.020>.
- [24] V. V. Uchaikin, R. T. Sibatov, and V. V. Saenko. “*Leaky-box approximation to the fractional diffusion model*”. Journal of Physics: Conference Series 409 (Feb. 2013), p. 012057. issn: 1742-6596. doi: 10.1088/1742-6596/409/1/012057. URL: <http://dx.doi.org/10.1088/1742-6596/409/1/012057>.
- [25] ESA and the Planck Collaboration. Harrington, J.D. and Whitney, C. Planck Mission Brings Universe into Sharp Focus. 2013. URL: https://d2pn8kiwq2w21t.cloudfront.net/original_images/jpegPIA16873.jpg.
- [26] E. Komatsu. “*New physics from the polarized light of the cosmic microwave background*”. Nature Reviews Physics 4.7 (May 2022), pp. 452–469. issn: 2522-5820. doi: 10.1038/s42254-022-00452-4. URL: <http://dx.doi.org/10.1038/s42254-022-00452-4>.
- [27] D. N. Basu. Big Bang: a theory or fact. 2024. arXiv: 2409.20299 [nucl-th]. URL: <https://arxiv.org/abs/2409.20299>.
- [28] D. Nath. “*The Darkness of Dark Matter and Dark Energy*”. International Journal of Engineering and Applied Sciences (IJEAS) 5 (June 2018). doi: 10.31873/IJEAS.5.6.05.

- [29] E. Komatsu et al. “*FIVE-YEAR WILKINSON MICROWAVE ANISOTROPY PROBE OBSERVATIONS: COSMOLOGICAL INTERPRETATION*”. *The Astrophysical Journal Supplement Series* 180.2 (Feb. 2009), pp. 330–376. issn: 1538-4365. doi: 10.1088/0067-0049/180/2/330. url: <http://dx.doi.org/10.1088/0067-0049/180/2/330>.
- [30] R. P. Gupta. “*JWST early Universe observations and Λ CDM cosmology*”. *Monthly Notices of the Royal Astronomical Society* 524.3 (July 2023), pp. 3385–3395. issn: 1365-2966. doi: 10.1093/mnras/stad2032. url: <http://dx.doi.org/10.1093/mnras/stad2032>.
- [31] P. A. R. Ade and Aghanim. “*Planck2013 results. XVI. Cosmological parameters*”. *Astronomy and Astrophysics* 571 (Oct. 2014), A16. issn: 1432-0746. doi: 10.1051/0004-6361/201321591. url: <http://dx.doi.org/10.1051/0004-6361/201321591>.
- [32] J. D. Simon. “*The Faintest Dwarf Galaxies*”. *Annual Review of Astronomy and Astrophysics* 57.1 (Aug. 2019), pp. 375–415. issn: 1545-4282. doi: 10.1146/annurev-astro-091918-104453. url: <http://dx.doi.org/10.1146/annurev-astro-091918-104453>.
- [33] P. Salucci. “*The distribution of dark matter in galaxies*”. *The Astronomy and Astrophysics Review* 27.1 (Feb. 2019). issn: 1432-0754. doi: 10.1007/s00159-018-0113-1. url: <http://dx.doi.org/10.1007/s00159-018-0113-1>.
- [34] S. W. Allen, A. E. Evrard, and A. B. Mantz. “*Cosmological Parameters from Observations of Galaxy Clusters*”. *Annual Review of Astronomy and Astrophysics* 49.1 (Sept. 2011), pp. 409–470. issn: 1545-4282. doi: 10.1146/annurev-astro-081710-102514. url: <http://dx.doi.org/10.1146/annurev-astro-081710-102514>.
- [35] P. Schneider, J. Ehlers, and E. E. Falco. Gravitational Lenses. Provided by the SAO/NASA Astrophysics Data System. 1992. doi: 10.1007/978-3-662-03758-4. url: <https://ui.adsabs.harvard.edu/abs/1992grle.book.....S>.
- [36] S. D. M. White, G. Efstathiou, and C. S. Frenk. “*The amplitude of mass fluctuations in the universe*”. 262.4 (June 1993), pp. 1023–1028. doi: 10.1093/mnras/262.4.1023.
- [37] J. Knolle. “*Prompt searches for feebly interacting particles at the LHC*”. *Proceedings of 12th Large Hadron Collider Physics Conference — PoS(LHCP2024)*. LHCP2024. Sissa Medialab, June 2025, p. 180. doi: 10.22323/1.478.0180. url: <http://dx.doi.org/10.22323/1.478.0180>.

- [38] I. Cagnoli, D. Kyratzis, and D. Serini. “*HERD space mission: Probing the Galactic Cosmic Ray frontier*”. Nuclear Instruments and Methods in Physics Research Section A: Accelerators, Spectrometers, Detectors and Associated Equipment 1068 (2024), p. 169788. ISSN: 0168-9002. DOI: <https://doi.org/10.1016/j.nima.2024.169788>. URL: <https://www.sciencedirect.com/science/article/pii/S0168900224007149>.
- [39] M. Aguilar et al. “*The Alpha Magnetic Spectrometer (AMS) on the international space station: Part II —Results from the first seven years*”. Physics Reports 894 (2021). The Alpha Magnetic Spectrometer (AMS) on the International Space Station: Part II - Results from the First Seven Years, pp. 1–116. ISSN: 0370-1573. DOI: <https://doi.org/10.1016/j.physrep.2020.09.003>. URL: <https://www.sciencedirect.com/science/article/pii/S0370157320303434>.
- [40] M. Aguilar. “*Antiproton Flux, Antiproton-to-Proton Flux Ratio, and Properties of Elementary Particle Fluxes in Primary Cosmic Rays Measured with the Alpha Magnetic Spectrometer on the International Space Station*”. Phys. Rev. Lett. 117 (9 Aug. 2016), p. 091103. DOI: [10.1103/PhysRevLett.117.091103](https://doi.org/10.1103/PhysRevLett.117.091103). URL: <https://link.aps.org/doi/10.1103/PhysRevLett.117.091103>.
- [41] P. A. M. Dirac. “*The quantum theory of the electron*”. Proceedings of The Royal Society A: Mathematical, Physical and Engineering Sciences 117 (1928), pp. 610–624. URL: <https://api.semanticscholar.org/CorpusID:54061357>.
- [42] C. D. Anderson. “*The Positive Electron*”. Phys. Rev. 43 (6 Mar. 1933), pp. 491–494. DOI: [10.1103/PhysRev.43.491](https://doi.org/10.1103/PhysRev.43.491). URL: <https://link.aps.org/doi/10.1103/PhysRev.43.491>.
- [43] E. Segrè. “*Nuclear Properties of Antinucleons*”. Science 132.3418 (1960), pp. 9–14. DOI: [10.1126/science.132.3418.9](https://doi.org/10.1126/science.132.3418.9). eprint: <https://www.science.org/doi/pdf/10.1126/science.132.3418.9>. URL: <https://www.science.org/doi/abs/10.1126/science.132.3418.9>.
- [44] D. E. Dorfan et al. “*Observation of Antideuterons*”. Phys. Rev. Lett. 14 (24 June 1965), pp. 1003–1006. DOI: [10.1103/PhysRevLett.14.1003](https://doi.org/10.1103/PhysRevLett.14.1003). URL: <https://link.aps.org/doi/10.1103/PhysRevLett.14.1003>.
- [45] Y. M. Antipov, N. K. Vishnevskii, and Y. P. Gorin. “*OBSERVATION OF sup3He.*” Yadern. Fiz. 12: 311-22(Aug 1970). (Jan. 1970). URL: <https://www.osti.gov/biblio/4086416>.

- [46] T.S. Collaboration. “*Observation of the antimatter helium-4 nucleus*”. Nature 473.7347 (Apr. 2011), pp. 353–356. issn: 1476-4687. doi: 10.1038/nature10079. url: <http://dx.doi.org/10.1038/nature10079>.
- [47] T. S. Collaboration. “*Observation of an Antimatter Hypernucleus*”. Science 328.5974 (Apr. 2010), pp. 58–62. issn: 1095-9203. doi: 10.1126/science.1183980. url: <http://dx.doi.org/10.1126/science.1183980>.
- [48] T. S. Collaboration. “*Observation of the antimatter hypernucleus*”. Nature 632.8027 (Aug. 2024), pp. 1026–1031. issn: 1476-4687. doi: 10.1038/s41586-024-07823-0. url: <http://dx.doi.org/10.1038/s41586-024-07823-0>.
- [49] S. Coutu et al. “*High-energy Antimatter Telescope (HEAT): basic design and performance*”. Gamma-Ray and Cosmic-Ray Detectors, Techniques, and Missions. Ed. by B. D. Ramsey and T. A. Parnell. Vol. 2806. Society of Photo-Optical Instrumentation Engineers (SPIE) Conference Series. Oct. 1996, pp. 113–120. doi: 10.1117/12.253971.
- [50] P. Picozza et al. “*PAMELA – A payload for antimatter matter exploration and light-nuclei astrophysics*”. Astroparticle Physics 27.4 (2007), pp. 296–315. issn: 0927-6505. doi: <https://doi.org/10.1016/j.astropartphys.2006.12.002>. url: <https://www.sciencedirect.com/science/article/pii/S0927650506001861>.
- [51] G. Anshakov and V. Skirmunt. “*The Russian project of “resurs-DK 1” space complex development. Status, prospects, new opportunities for the consumers of space snapshots*”. Acta Astronautica 47.2 (2000). Space an Integral Part of the Information Age, pp. 347–353. issn: 0094-5765. doi: [https://doi.org/10.1016/S0094-5765\(00\)00076-X](https://doi.org/10.1016/S0094-5765(00)00076-X). url: <https://www.sciencedirect.com/science/article/pii/S009457650000076X>.
- [52] B. Alpat. “*The Alpha Magnetic Spectrometer (AMS) experiment on the International Space Station*”. Nuclear Instruments and Methods in Physics Research Section A: Accelerators, Spectrometers, Detectors and Associated Equipment 461.1 (2001). 8th Pisa Meeting on Advanced Detectors, pp. 272–274. issn: 0168-9002. doi: [https://doi.org/10.1016/S0168-9002\(00\)01223-7](https://doi.org/10.1016/S0168-9002(00)01223-7). url: <https://www.sciencedirect.com/science/article/pii/S0168900200012237>.
- [53] M. Aguilar. “*Towards Understanding the Origin of Cosmic-Ray Positrons*”. Phys. Rev. Lett. 122 (4), p. 041102. doi: 10.1103/PhysRevLett.122.041102. url: <https://link.aps.org/doi/10.1103/PhysRevLett.122.041102>.

- [54] V. Poulin et al. “*Where do the AMS-02 antihelium events come from?*” Phys. Rev. D 99 (2 June 2019), p. 023016. doi: 10.1103/PhysRevD.99.023016. URL: <https://link.aps.org/doi/10.1103/PhysRevD.99.023016>.
- [55] E. S. Agency. AMS-02 on the International Space Station. 2019. URL: https://www.esa.int/ESA_Multimedia/Images/2019/11/AMS-02_on_the_International_Space_Station.
- [56] S. Ahlen et al. “*An antimatter spectrometer in space*”. Nuclear Instruments and Methods in Physics Research Section A: Accelerators, Spectrometers, Detectors and Associated Equipment 350.1 (1994), pp. 351–367. issn: 0168-9002. doi: [https://doi.org/10.1016/0168-9002\(94\)91184-3](https://doi.org/10.1016/0168-9002(94)91184-3). URL: <https://www.sciencedirect.com/science/article/pii/0168900294911843>.
- [57] M. A. et al. “*The Alpha Magnetic Spectrometer (AMS) on the International Space Station: Part I – results from the test flight on the space shuttle*”. Physics Reports 366.6 (2002), pp. 331–405. issn: 0370-1573. doi: [https://doi.org/10.1016/S0370-1573\(02\)00013-3](https://doi.org/10.1016/S0370-1573(02)00013-3). URL: <https://www.sciencedirect.com/science/article/pii/S0370157302000133>.
- [58] T. Kirn and T. Siedenburg. “*The AMS-02 transition radiation detector*”. Nuclear Instruments and Methods in Physics Research Section A: Accelerators, Spectrometers, Detectors and Associated Equipment 535.1 (2004). Proceedings of the 10th International Vienna Conference on Instrumentation, pp. 165–170. issn: 0168-9002. doi: <https://doi.org/10.1016/j.nima.2004.07.273>. URL: <https://www.sciencedirect.com/science/article/pii/S0168900204015955>.
- [59] V. Bindi et al. “*The time of flight detector of the AMS-02 experiment on the international space station*”. Nuclear Instruments and Methods in Physics Research Section A: Accelerators, Spectrometers, Detectors and Associated Equipment 718 (2013). Proceedings of the 12th Pisa Meeting on Advanced Detectors, pp. 478–480. issn: 0168-9002. doi: <https://doi.org/10.1016/j.nima.2012.11.061>. URL: <https://www.sciencedirect.com/science/article/pii/S0168900212013988>.
- [60] V. Bindi et al. “*Calibration and performance of the AMS-02 time of flight detector in space*”. Nuclear Instruments and Methods in Physics Research Section A: Accelerators, Spectrometers, Detectors and Associated Equipment 743 (2014), pp. 22–29. issn: 0168-9002. doi: <https://doi.org/10.1016/j.nima.2014.01.002>. URL: <https://www.sciencedirect.com/science/article/pii/S0168900214000102>.

- [61] F. Giovacchini. “*The RICH detector of the AMS-02 experiment aboard the International Space Station*”. Nuclear Instruments and Methods in Physics Research Section A: Accelerators, Spectrometers, Detectors and Associated Equipment 1055 (2023), p. 168434. issn: 0168-9002. doi: <https://doi.org/10.1016/j.nima.2023.168434>. URL: <https://www.sciencedirect.com/science/article/pii/S0168900223004242>.
- [62] AMS02. The Ring Imaging Cherenkov Detector. URL: <https://ams02.space/detector/ring-imaging-cherenkov-detector-rich>.
- [63] M. Aguilar-Benitez et al. “*In-beam aerogel light yield characterization for the AMS RICH detector*”. Nuclear Instruments and Methods in Physics Research Section A: Accelerators, Spectrometers, Detectors and Associated Equipment 614.2 (2010), pp. 237–249. issn: 0168-9002. doi: <https://doi.org/10.1016/j.nima.2009.12.027>. URL: <https://www.sciencedirect.com/science/article/pii/S0168900209023444>.
- [64] R. Kossakowski et al. “*Electromagnetic calorimeter for the AMS-02 experiment*” (Mar. 2002).
- [65] AMS02. The Electromagnetic Calorimeter. URL: <https://ams02.space/detector/electromagnetic-calorimeter-ecal>.
- [66] P. von Doetinchem et al. The Anticoincidence Counter System of AMS-02. 2009. arXiv: 0906.1068 [astro-ph.IM]. URL: <https://arxiv.org/abs/0906.1068>.
- [67] Dr.C.H.Chung. The Electromagnetic Calorimeter. URL: https://www1b.physik.rwthaachen.de/~schael/AMS_ACC.html.
- [68] F. Donnini. “*Flux measurement of light nuclei in Cosmic Rays with the AMS-02 experiment*”. PhD thesis. Università degli Studi di Perugia, Feb. 2023, p. 138.
- [69] B. Blau et al. “*The superconducting magnet of AMS-02*”. Nuclear Physics B - Proceedings Supplements 113.1 (2002), pp. 125–132. issn: 0920-5632. doi: [https://doi.org/10.1016/S0920-5632\(02\)01831-5](https://doi.org/10.1016/S0920-5632(02)01831-5). URL: <https://www.sciencedirect.com/science/article/pii/S0920563202018315>.
- [70] C. Cecchi. “*The Silicon Tracker of the AMS02 experiment*”. Nuclear Instruments and Methods in Physics Research Section A: Accelerators, Spectrometers, Detectors and Associated Equipment 518.1 (2004). Frontier Detectors for Frontier Physics: Proceedin, pp. 145–146. issn: 0168-9002. doi: <https://doi.org/10.1016/j.nima.2003.10.045>. URL: <https://www.sciencedirect.com/science/article/pii/S0168900203027566>.

- [71] J. Tian. “*Precision Measurement of Neon, Magnesium, and Silicon Fluxes in Cosmic Rays Measured by AMS on the International Space Station*”. PhD thesis. Università degli Studi di Perugia, Feb. 2020, p. 124.
- [72] G. Ambrosi et al. “*The spatial resolution of the silicon tracker of the Alpha Magnetic Spectrometer*”. Nuclear Instruments and Methods in Physics Research Section A: Accelerators, Spectrometers, Detectors and Associated Equipment 869 (Oct. 2017), pp. 29–37. doi: [10.1016/j.nima.2017.07.014](https://doi.org/10.1016/j.nima.2017.07.014). URL: <https://hal.science/hal-04132374>.
- [73] P. Saouter. “*Nuclei identification with the AMS-02 silicon tracker and measurement of cosmic ray nuclei fluxes*”. 2014. URL: <https://api.semanticscholar.org/CorpusID:209775843>.
- [74] G. A. M. Duranti P. Zuccon. AMS-L0 Technical Design Report - TDR. 2024.
- [75] H. collaboration. The High Energy cosmic-Radiation Detection (HERD) facility. URL: <https://herd.ihep.ac.cn/>.
- [76] J. Chang et al. “*The DArk Matter Particle Explorer mission*”. Astroparticle Physics 95 (2017), pp. 6–24. issn: 0927-6505. doi: <https://doi.org/10.1016/j.astropartphys.2017.08.005>. URL: <https://www.sciencedirect.com/science/article/pii/S0927650517300841>.
- [77] D. Kyratzi. “*Latest advancements of the HERD space mission*”. Nuclear Instruments and Methods in Physics Research Section A: Accelerators, Spectrometers, Detectors and Associated Equipment 1048 (2023), p. 167970. issn: 0168-9002. doi: <https://doi.org/10.1016/j.nima.2022.167970>. URL: <https://www.sciencedirect.com/science/article/pii/S0168900222012621>.
- [78] D. Kyratzi. “*Overview of the HERD space mission*”. Physica Scripta 97 (Apr. 2022). doi: [10.1088/1402-4896/ac63fc](https://doi.org/10.1088/1402-4896/ac63fc).
- [79] C. Perrina et al. “*FIT: the scintillating fiber tracker of the HERD space mission*”. Aug. 2021, p. 067. doi: [10.22323/1.395.0067](https://doi.org/10.22323/1.395.0067).
- [80] F. Gargano. “*The High Energy cosmic-Radiation Detection facility (HERD)*”. Oct. 2020, p. 035. doi: [10.22323/1.364.0035](https://doi.org/10.22323/1.364.0035).
- [81] F. Alemanno et al. “*Status of the plastic scintillator detector for the HERD experiment*”. Nuclear Instruments and Methods in Physics Research Section A: Accelerators, Spectrometers, Detectors and Associated Equipment 1051 (2023), p. 168237. issn: 0168-9002. doi: <https://doi.org/10.1016/j.nima.2023.168237>. URL: <https://www.sciencedirect.com/science/article/pii/S0168900223002279>.

- [82] G. Silvestre and on behalf of the HERD SCD collaboration. “*The Silicon Charge Detector of the High Energy Cosmic Radiation Detection experiment*”. Journal of Instrumentation 19.03 (Mar. 2024), p. C03042. doi: [10.1088/1748-0221/19/03/C03042](https://doi.org/10.1088/1748-0221/19/03/C03042). URL: <https://dx.doi.org/10.1088/1748-0221/19/03/C03042>.
- [83] C. Dai. “*Development of Transition Radiation Detector for HERD*”. PoS ICRC2023 (2023), p. 113. doi: [10.22323/1.444.0113](https://doi.org/10.22323/1.444.0113).
- [84] C. Hu. Modern Semiconductor Devices for Integrated Circuits. Pearson, 2009. URL: <https://www.chu.berkeley.edu/>.
- [85] H. Zhang. Loss Mechanisms In Non-Fullerene Organic Solar Cells. Oct. 2021. ISBN: 9789179290344. doi: [10.3384/diss.diva-178408](https://doi.org/10.3384/diss.diva-178408).
- [86] P. Atkins, J. Paula, and D. Smith. “*The Boltzmann distribution*”. Aug. 2023. ISBN: 9780198727873. doi: [10.1093/hesc/9780198727873.003.0070](https://doi.org/10.1093/hesc/9780198727873.003.0070).
- [87] D. Santostasi. “*Caratterizzazione elettrica di un sensore planare al silicio a bordo attivo irraggiato*”. PhD thesis. Sept. 2014. doi: [10.13140/RG.2.2.35850.98242](https://doi.org/10.13140/RG.2.2.35850.98242).
- [88] G. Lutz. Semiconductor Radiation Detectors: Device Physics. New York: Springer, 1999. ISBN: 978-3-540-64859-8.
- [89] C. Leroy and P. G. Rancoita. Principles of Radiation Interaction in Matter and Detection. Nov. 2004. ISBN: 978-981-238-909-1. doi: [10.1142/5578](https://doi.org/10.1142/5578).
- [90] W. Shockley. “*Currents to Conductors Induced by a Moving Point Charge*”. Journal of Applied Physics 9.10 (Oct. 1938), pp. 635–636. ISSN: 0021-8979. doi: [10.1063/1.1710367](https://doi.org/10.1063/1.1710367). eprint: https://pubs.aip.org/aip/jap/article-pdf/9/10/635/18304047/635_1_online.pdf. URL: <https://doi.org/10.1063/1.1710367>.
- [91] S. Ramo. “*Currents Induced by Electron Motion*”. Proceedings of the IRE 27.9 (1939), pp. 584–585. doi: [10.1109/JRPROC.1939.228757](https://doi.org/10.1109/JRPROC.1939.228757).
- [92] F. Hartmann. “*Basic Principles of a Silicon Detector*”. Evolution of Silicon Sensor Technology in Particle Physics. Cham: Springer International Publishing, 2017, pp. 1–133. ISBN: 978-3-319-64436-3. doi: [10.1007/978-3-319-64436-3_1](https://doi.org/10.1007/978-3-319-64436-3_1). URL: https://doi.org/10.1007/978-3-319-64436-3_1.
- [93] H. Spieler. “*Semiconductor Detector Systems*”. 2005. URL: <https://api.semanticscholar.org/CorpusID:107068623>.
- [94] S. Navas et al. “*Review of particle physics*”. Phys. Rev. D 110.3 (2024), p. 030001. doi: [10.1103/PhysRevD.110.030001](https://doi.org/10.1103/PhysRevD.110.030001).
- [95] J. Ankerhold. “*Springer Tracts in Modern Physics*”. Springer Tracts in Modern Physics 224 (Jan. 2007), pp. 1–5. doi: [10.1007/3-540-68076-4_1](https://doi.org/10.1007/3-540-68076-4_1).

- [96] IDEAS. Integrated Detector Electronics AS IDEAS. 2024. URL: <https://ideas.no/>.
- [97] M. Barbanera. “DESIGN, DEVELOPMENT, AND TEST OF DATA ACQUISITION SYSTEMS FOR PHYSICS IN SPACE”. PhD thesis. UNIVERSITÁ DI PISA, Jan. 2022, p. 80.
- [98] G. Silvestre. “Development of the external tracker of the FOOT experiment”. PhD thesis. Università degli Studi di Perugia, Feb. 2021, p. 112.
- [99] R. Pugliese, S. Regondi, and R. Marini. “Machine learning-based approach: global trends, research directions, and regulatory standpoints”. Data Science and Management 4 (2021), pp. 19–29. issn: 2666-7649. doi: <https://doi.org/10.1016/j.dsm.2021.12.002>. URL: <https://www.sciencedirect.com/science/article/pii/S2666764921000485>.
- [100] M. Mohri, A. Rostamizadeh, and A. Talwalkar. Foundations of machine learning. English (US). MIT Press, 2012.
- [101] T. Inc. DE10-Nano Development Board. 2024. URL: <https://www.terasic.com.tw/cgi-bin/page/archive.pl?No=1046>.
- [102] A. Oliva. “High Charge Cosmic Rays Measurement with the AMS-02 Silicon Tracker”. PhD thesis. Università degli Studi di Perugia, 2007.
- [103] A. K. Drukier, K. Freese, and D. N. Spergel. “Detecting cold dark-matter candidates”. Phys. Rev. D 33 (12 June 1986), pp. 3495–3508. doi: [10.1103/PhysRevD.33.3495](https://doi.org/10.1103/PhysRevD.33.3495). URL: <https://link.aps.org/doi/10.1103/PhysRevD.33.3495>.
- [104] L. Canetti, M. Drewes, and M. Shaposhnikov. “Matter and antimatter in the universe”. New Journal of Physics 14.9 (Sept. 2012), p. 095012. issn: 1367-2630. doi: [10.1088/1367-2630/14/9/095012](https://doi.org/10.1088/1367-2630/14/9/095012). URL: <http://dx.doi.org/10.1088/1367-2630/14/9/095012>.
- [105] A. Green. “Dark matter in astrophysics/cosmology”. SciPost Physics Lecture Notes (Jan. 2022). issn: 2590-1990. doi: [10.21468/scipostphyslectnotes.37](https://doi.org/10.21468/scipostphyslectnotes.37). URL: <http://dx.doi.org/10.21468/SciPostPhysLectNotes.37>.
- [106] M. Pohl. Cosmic Ray Space Experiments. 2025. arXiv: 2502.18025 [hep-ex]. URL: <https://arxiv.org/abs/2502.18025>.